

**Design and Implementation of Integrated GHz Frequency Capacitance  
Cytometer with aF Sensitivity for Single Cell Characterization**

by

**Kaveh Mohammad**

A Thesis submitted to the faculty of Graduate Studies of  
University of Manitoba  
in partial fulfillment of the requirement of the degree

**Doctor of Philosophy**

Department of Electrical and Computer Engineering  
University of Manitoba  
Winnipeg, Manitoba, Canada

Copyright © 2016 by Kaveh Mohammad

## **Abstract**

This thesis is focused on the design, implementation, and measurements of integrated electronic sensors developed for detection and analysis of single biological cells in microfluidic systems. This work introduces three separate designs.

The first is a microwave frequency reflectometer on a printed circuit board (PCB) which operates at  $\sim 1.8$  GHz, and achieves  $\sim 1.25$  aF capacitance sensitivity in less than 100 mV sensing voltage. It is used for detection of  $5.7 \mu\text{m}$  Poly-Styrene Spheres (PSS) and Chinese Hamster Ovary cells (CHO). This sensor was successfully used to detect DEP response of PSS with a sensitivity close to the connectorized resonator based microwave interferometer.

The second design is a differential ring oscillator based capacitance sensor on a PCB. The oscillation frequency of two oscillators (one connected to detection microelectrodes) are compared by an XOR gate, and is monitored using a frequency counter. It achieves  $\sim 180$  aF sensitivity in 100 ms averaging time and  $\sim 2.5$  V sensing voltages. It is used for detection of water with Isopropyl Alcohol contents up to 1%, and for detection of  $15 \mu\text{m}$  PSS.

The third design is an integrated DEP cytometer sensor. It is composed of an optimized capacitance sensor implemented using  $0.35 \mu\text{m}$  CMOS technology, on which a machined PMMA microfluidic is clamped to provide a path for cells to flow. The capacitance sensor operates at 500 MHz/1.4 GHz, and achieves  $\sim 14$  aF sensitivity in 100 ms averaging time and  $\sim 1.4$  V sensing voltage. The sensor is used for detection of  $10 \mu\text{m}$  PSS and CHO cells. It is used to observe shifts in PSS and CHO cells signatures normalized peak difference histograms when positive or negative DEP forces are applied. Finally, equations of the capacitance sensor noise and sensitivity are calculated. Calculated noise in frequency and time domains are compared with measurement results and suggestions are given to improve this sensor.

These integrated sensors are small in size, low cost, portable and easily reproducible compared with bulky electrical sensors. They are markerless compared with conventional single cell analysis assays. These designs introduce new approaches for detection of biomaterials in a wide range of microfluidic applications.

## **Acknowledgement**

Firstly, I would like to express my sincere gratitude to my advisor Prof. Douglas Thomson for the continuous support of my Ph.D study and related research, for his patience, motivation, and immense knowledge. His guidance helped me in all the time of research and writing of papers and thesis. He provided me with the opportunity of two internships in industry in the related fields of my Ph.D study. He made me involved in other industrial and academic projects such as in the field of structural health monitoring, which all helped me gather experience and develop my knowledge. I appreciate his flexible attitude toward my research which led me to love my work and enjoy it. I appreciate his considerations toward my welfare during my study. I could not imagine having a better advisor and mentor for my Ph.D study. I had some of the best years of my life having him as my advisor.

I would like to thank Prof. Gregory Bridges for giving strong feedbacks and support during designs and measurements, which incited me to widen my research from various perspectives. The “Experimental Methods in Microwave Engineering” course I had with him was very helpful in designing microwave frequency sensors as an important part of my Ph.D thesis. I should also thank my research committee member Prof. Francis Lin for his insightful comments and encouragement. I should thank Prof. Douglas Buchanan who was a great help all during my Ph.D program. He has been an immense source of knowledge for me during the “MEMS and Microfabrication” course I had with him. He helped me a lot in designing the integrated CMOS based DEP-cytometer sensor as the main part of my Ph.D thesis, whom without his helps I wouldn't be able to get the sensor working on the first try.

I should acknowledge helps from my friend Farhad Sheikhhossieni at University of Manitoba, and Jim Quinn from Canadian Microelectronics Corporation (CMC), who gave me invaluable helps

and instructions during designing integrated DEP-cytometer chip in Cadence. I should thank CMC microsystems for providing the opportunity of “Analog Mixed Signal Design Methodology in Cadence” training course and also access to Cadence IC design CAD tool. I should thank CMC for providing access to TSMC 0.35  $\mu\text{m}$  fabrication process and microfluidic chip fabrication.

Thanks to James Dietrich for his time and effort in providing this work with valuable RF measurement tools and facilities. Thanks from “Advanced RF Systems Laboratory” at University of Manitoba for providing high impedance probes, high frequency scope, frequency counter, phase noise personality analyzer, spectrum analyzer and impedance analyzer which made measurement and characterization of PCBs and the chips possible. I should also thank Cory Smit at University of Manitoba machine shop for making the PMMA microfluidic part for on chip PSS and CHO cell measurements.

I should acknowledge Natural Sciences and Engineering Research Council of Canada (NSERC), Canadian Foundation for Innovation (CFI), Western Economic Diversification Canada (WD), and the Province of Manitoba for providing financial support of this work. I should also thank Mitacs Canada for providing research grants for the involved internships.

*Dedicated to my Family*

## **Contributions of Authors**

This thesis is comprised of one published journal paper, one journal paper in press, one submitted journal paper, and a conference paper. K. Mohammad is the first author in all of them. All papers have multiple authors. Contributions of the authors in each paper is as follows.

**Chapter 2: K. Mohammad, K. Braasch, E. Salimi, A. Bhide, B. S. Rizzi, M. Butler, G. Bridges, D. Thomson, “A compact microwave frequency reflectometer with atto-Farad sensitivity: A path towards an integrated dielectrophoresis cytometer”, *Sensors and Actuators A: Physical*, vol.232, pp.132-140, 2015.**

In this chapter of the thesis, D. Thomson developed the idea. K. Mohammad developed the printed circuit board design for the article, carried out all measurements and data analysis. He also wrote the manuscript which was edited by D. Thomson. This work was done in collaboration with Department of Microbiology where K. Braasch and M. Butler provided the work with CHO cell samples for measurements. E. Salimi developed the microfluidic chip design, A. Bhide, B. S. Rizzi developed the semi-automated data analysis code in Matlab and G. Bridges provided helpful instructions and RF measurement tools during design and testing of the microwave frequency sensor.

**Chapter 3: K. Mohammad, D. J. Thomson, “Differential Ring Oscillator Based Capacitance Sensor for Microfluidic Applications”, in Press, *IEEE Transactions on Biomedical Circuits and Systems*, 2016.**

In this chapter of the thesis, D. Thomson developed the idea, K. Mohammad designed, implemented and tested the printed circuit board sensor. K. Mohammad carried out all the simulations, measurements and data analysis in the work. He wrote the article manuscript and D. Thomson edited it.

**Chapter 4: Integrated 0.35  $\mu\text{m}$  CMOS Capacitance Sensor with atto-Farad Sensitivity for Single Cell Analysis, K. Mohammad, D. A. Buchanan, and D. J. Thomson, IEEE Biomedical Circuits and Systems Conference, 2016.**

In this chapter of the thesis, D. J. Thomson and K. Mohammad developed the idea. K. Mohammad designed the chip in Cadence. He carried out all simulations, design testing, measurements with the sensor and data analysis. He wrote the paper and D. J. Thomson and D. A. Buchanan edited it. D. A. Buchanan also helped with simulations of the chip in Cadence.

**Chapter 5: GHz Frequency CMOS DEP Cytometer for Characterization of Single Biological Cells, K. Mohammad, D. A. Buchanan, K. Braasch, M. Butler, and D. J. Thomson, Submitted to Lab on Chip Journal, 2016.**

This chapter of thesis is completion of the work in chapter 4. K. Mohammad accomplished all the simulations, measurements and data analysis in this work. He wrote the paper and D. J. Thomson and D. A. Buchanan edited it. This work was done in collaboration with Department of Microbiology where K. Braasch and M. Butler provided biological CHO cell samples for measurements.

# Table of Contents

Abstract.....	i
Acknowledgement.....	iii
Contributions of Authors .....	vi
List of Tables .....	xi
List of Figures.....	xii
List of Copyrighted Materials for which Permission was Obtained.....	xiii
Nomenclature .....	xiv
<b>Chapter 1: Introduction .....</b>	<b>1</b>
<b>1.1 Motivation .....</b>	<b>1</b>
<b>1.2 Detection Methods.....</b>	<b>1</b>
<b>1.2.1 Dielectrophoresis (DEP).....</b>	<b>2</b>
<b>1.2.2 Electro-Rotation (EROT).....</b>	<b>4</b>
<b>1.2.3 Impedance Spectroscopy.....</b>	<b>4</b>
<b>1.2.4 Electro-physiometry .....</b>	<b>6</b>
<b>1.3 Comparison of Electrical Methods .....</b>	<b>7</b>
<b>1.4 Resonator Based Capacitance DEP-Cytometer .....</b>	<b>8</b>
<b>1.5 Thesis Structure and Contributions .....</b>	<b>9</b>
<b>Chapter 2: A Compact Microwave Frequency Reflectometer with atto-Farad Sensitivity: a Path towards an Integrated Dielectrophoresis Cytometer.....</b>	<b>14</b>
<b>2.1 Abstract .....</b>	<b>14</b>
<b>2.2 Introduction .....</b>	<b>14</b>
<b>2.3 Methods and Experiments.....</b>	<b>17</b>
<b>2.3.1 Reflectometer Design Details.....</b>	<b>17</b>
<b>2.3.2 Power Levels on Board.....</b>	<b>19</b>
<b>2.3.3 Sensor Tuning .....</b>	<b>21</b>
<b>2.3.4 Sensitivity Measurement Method.....</b>	<b>22</b>
<b>2.4 Results and Discussion .....</b>	<b>22</b>
<b>2.4.1 Sensitivity Detection .....</b>	<b>22</b>
<b>2.4.2 Detection of Mammalian Cells .....</b>	<b>23</b>
<b>2.4.3 Verification of Detection Without Perturbation.....</b>	<b>24</b>

2.4.4 Sensitivity to Changes in Media Conductivity .....	26
2.4.5 Reflectometer Design in Comparison with Resonator Based Sensors.....	29
2.5 Conclusion.....	31
<b>Chapter 3: Differential Ring Oscillator Based Capacitance Sensor for Microfluidic Applications .....</b>	<b>33</b>
3.1 Abstract .....	33
3.3 Design Description.....	35
3.4 Simulation and Characterization.....	39
3.5 Description of System Noise .....	41
3.6 Results and Discussion .....	44
<b>Chapter 4: GHz Frequency CMOS DEP Cytometer for Characterization of Single Biological Cells .....</b>	<b>53</b>
4.1 Abstract .....	53
4.2 Introduction .....	53
4.3 Design .....	54
4.4 Design Optimization for Single Cell Application .....	55
4.5 Sensitivity Measurement .....	61
4.6 Sensor Bandwidth .....	62
4.7 Conclusion.....	64
<b>Chapter 5: GHz Frequency CMOS DEP Cytometer for Characterization of Single Biological Cells .....</b>	<b>66</b>
5.1 Abstract .....	66
5.2 Introduction .....	66
5.3 System Design .....	72
5.3.1 Detection Microelectrodes .....	73
5.3.2 Ring Oscillator Design.....	73
5.4 Materials and Methods .....	77
5.5 Results and Discussion .....	80
5.5.1 CMOS Sensor Characterization.....	80
5.5.2 Detection of PSS.....	84
5.5.3 PSS Signatures with DEP.....	86
5.5.4 Statistical Analysis of PSS Signatures .....	88

<b>5.5.5 Statistical Analysis of CHO cells Signatures</b> .....	89
<b>5.6 Conclusion</b> .....	94
<b>Chapter 6: GHz Frequency CMOS DEP Cytometer Noise and Sensitivity Analysis</b> .....	96
<b>6.1 Abstract</b> .....	96
<b>6.2 Introduction</b> .....	96
<b>6.3 Dominant source of noise</b> .....	97
<b>6.4 Calculation of phase noise due to 1/f noise</b> .....	100
<b>6.5 Phase noise measurement results</b> .....	103
<b>6.6 Jitter calculation from measured phase noise spectrum</b> .....	103
<b>6.7 Suggestions on how to improve the design SNR</b> .....	106
<b>6.8 Conclusion</b> .....	107
<b>Chapter 7: Conclusions and Future Work</b> .....	109
<b>7.1 Overview of the Accomplished Works</b> .....	109
<b>7.2 Comparison with Capacitance Sensors in Other Works</b> .....	111
<b>7.3 Suggestions and Future Works</b> .....	113
<b>References</b> .....	116

## List of Tables

<b>Table 2.1:</b> Measured power levels at different nodes of the board. ....	20
<b>Table 2.2:</b> Sensitivity of High-Q, Low-Q resonator based sensors and microwave reflectometer sensor when DI water, and 0.1 S/m, 0.3 S/m, 1 S/m and 3 S/m saline solution are used. ....	29
<b>Table 3.1:</b> RMS frequency noise in time domain vs. averaging time .....	44
<b>Table 3.2:</b> Capacitance and frequency change for different IPA content. ....	46
<b>Table 3.3:</b> Number of 15 $\mu\text{m}$ beads signatures collected with the average and standard deviation of their peak values. ....	49
<b>Table 4.1:</b> Oscillation frequency and sensitivity changes by connecting microelectrodes to different stages. ....	58
<b>Table 4.2:</b> Chip Layout Pin and Components Description of Fig. 4.3. ....	60
<b>Table 4.3:</b> System noise for different averaging time frames. ....	64
<b>Table 5.1:</b> Oscillation frequency of the application specific tapered ring oscillators designed in CMOS 0.35 $\mu\text{m}$ technology. ....	76
<b>Table 5.2:</b> Capacitance sensitivity, oscillation frequency and voltage swing of microelectrodes located at different stages of the tapered oscillator. ....	77
<b>Table 5.3:</b> Description of components and pins shown in Fig. 5.1 (b). ....	79
<b>Table 5.4:</b> Particle/cell signatures peak amplitude shown in Fig. 5.3. ....	85
<b>Table 6.1:</b> 3-stage sensor measured noise with different supplies. ....	98
<b>Table 6.2:</b> 3-stage sensor frequency noise for different averaging time lengths. ....	99
<b>Table 6.3:</b> Parameters values used in noise equations. ....	102
<b>Table 6.4:</b> Parasitic capacitances at different nodes of 3-stage and 5-stage oscillator. ....	102
<b>Table 6.5:</b> Calculated vs. measured noise parameters. ....	106
<b>Table 7.1:</b> Comparison of the sensors developed by different groups for high sensitivity capacitance detection. ....	112

## List of Figures

<b>Figure 2.1:</b> The schematic of the reflectometer microwave frequency sensor is shown. ....	19
<b>Figure 2.2:</b> Single cell interferometer integrated on a PCB.....	21
<b>Figure 2.3:</b> A sample detected signal in the output of lock-in amplifier from a 5.7 $\mu\text{m}$ PSS.....	23
<b>Figure 2.4:</b> A sample signal of a CHO cell using the microwave reflectometer sensor obtained from the differential microelectrodes.....	24
<b>Figure 2.5:</b> Statistical analysis of the normalized peaks difference for 5.7 $\mu\text{m}$ beads signature with no DEP signal. ....	26
<b>Figure 2.6:</b> Statistical analysis of normalized peak differences for CHO cells signatures from the microwave reflectometer and resonator based design with no DEP signal. ....	27
<b>Figure 2.7:</b> Statistical analysis of the normalized peak differences for 580 PSS signatures obtained from the microwave reflectometer.....	28
<b>Figure 2.8:</b> Sensitivity changes for different sensors versus changes in media conductivity for the reflectometer. ....	30
<b>Figure 3.1:</b> Design schematic composed of two ring oscillators used for detection of capacitance change in a microfluidic channel. ....	36
<b>Figure 3.2:</b> Differential ring oscillator based capacitive sensor in contact with microelectrodes of a microfluidic channel.....	38
<b>Figure 3.3:</b> Capacitance sensitivity simulation vs. experimental measurements.....	40
<b>Figure 3.4:</b> Phase noise spectrum of ring oscillator2 operating at 260 MHz, and the output IF at 20 MHz.. ....	43
<b>Figure 3.5:</b> 4-port microfluidic chip used for detection of water-alcohol content and 15 $\mu\text{m}$ PSS. ....	46
<b>Figure 3.6:</b> Detection of DI water with IPA content with sensor (scales are different on figures). ....	47
<b>Figure 3.7:</b> Shift in the sensor output IF frequency when DI water in the microfluidic channel is replaced by DI water with 1%, 5%, 10%, 25%, 50% and 100% IPA content.....	48
<b>Figure 3.8:</b> Sample signatures of single and multiple 15 $\mu\text{m}$ PSS detected by the sensor.. ....	51
<b>Figure 4.1:</b> Ring oscillator based capacitance sensor design architecture.....	55
<b>Figure 4.2:</b> (a) 3-stage ring oscillator. (b) 5-stage ring oscillator. ....	57

<b>Figure 4.3:</b> Chip layout in Cadence. It is designed to be 2 mm×2 mm in dimension. ....	59
<b>Figure 4.4:</b> Sample signatures of PSS and CHO cell detected by the CMOS chip. ....	63
<b>Figure 5.1:</b> Design of an integrated DEP cytometer. ....	78
<b>Figure 5.2:</b> Characterization tests results for 5-stage and 3-stage sensors. ....	83
<b>Figure 5.3:</b> Sample signatures of polystyrene spheres and CHO cells detected with the chip for VDD=3 V. ....	85
<b>Figure 5.4:</b> Sample signatures of PSS detected by the chip for VDD=2 V, without applying DEP signal (VDEP=0) and with DEP signal applied at 1 MHz, 1 Vp-p. ....	87
<b>Figure 5.5:</b> Normalized peak difference distribution for 100 signatures of 10 μm PSS in DI water detected by 3-stage sensor. ....	90
<b>Figure 5.6:</b> Normalized peak difference distribution for 100 signatures of CHO cell in low conductivity medium detected by 3-stage sensor. ....	92
<b>Figure 6.1:</b> Sensor noise diagram. ....	97
<b>Figure 6.2:</b> A general n stage ring oscillator with $N_i$ unit inverter cells in its $i^{\text{th}}$ stage. ....	100
<b>Figure 6.3:</b> 3-stage sensor output and 3-stage ring oscillator measured phase noise spectrums. ....	104
<b>Figure 6.4:</b> 5-stage sensor output and 5-stage ring oscillator measured phase noise spectrums. ....	104

## **List of Copyrighted Materials for which Permission was Obtained**

- K. Mohammad, K. Braasch, E. Salimi, A. Bhide, B. S. Rizi, M. Butler, G. Bridges, D. Thomson, “A compact microwave frequency reflectometer with atto-Farad sensitivity: A path towards an integrated dielectrophoresis cytometer”, *Sensors and Actuators A: Physical*, vol.232, pp.132-140, 2015.

## **Nomenclature**

CHO: Chinese Hamster Ovary

PCB: Printed Circuit Board

RF: Radio Frequency

CMOS: Complementary Metal Oxide Semiconductor

PSS: polystyrene spheres

DEP: Dielectrophoresis

CMF: Clausius–Mossotti factor

aF: atto-Farad

SNR: Signal to Noise Ratio

LC: Inductive Capacitive

DI: de-Ionized

VNA: Vector Network Analyzer

LO: Local Oscillator

TTL: Transistor-Transistor Logic

LNA: Low Noise Amplifier

Q: Resonator Quality Factor

$\epsilon$ : Permittivity

GUI: General User Interface

LOC: Lab on Chip

PDEP: Positive DEP Force

NDEP: Negative DEP Force

IPA: Isopropyl Alcohol

XOR: Exclusive OR

IF: Intermediate Frequency

IBIS: Input/output Buffer Information and Specifications

MDC: Minimum Detectable Capacitance

DAC: Digital to Analog Converter

# **Chapter 1: Introduction**

## **1.1 Motivation**

The focus of this work is the electrical analysis of single cells using a dielectrophoretic (DEP) cytometer. In a DEP cytometer cells are analyzed one at a time. Electrical detection can be done as a bulk measurement or single cell measurement. Bulk measurements are based on the assumption that all the particles are the same, which is often not true. On the other hand, single cell analysis reveals properties of subpopulations of cells that are hidden in the average or bulk response [1]. Cytometers were developed to provide single cell analysis. However, most commercial cytometers rely on the use of optical analysis. This work uses an electrical approach to single cell analysis that offers the possibility of highly integrated analysis systems.

Single cell analysis systems seek to characterize many aspects of cells. This work focuses on apoptosis (programmed cell death), which causes the cell to condense and disassemble [1]. Apoptosis is a process important to many technological and health fields. For example, determining the viability of cells is important to monitoring cell cultures used in the production of biopharmaceuticals and in tracking the effectiveness of chemotherapy treatments. This work is focused on exploring new approaches to integrating the electronic detection and analysis of cells in DEP cytometers.

## **1.2 Detection Methods**

The methods developed for cellular analysis can be broadly categorized in two groups. The first is dye based methods in which cell samples are analyzed using absorption or attachment of dyes or fluorescent tags. Attachment or absorption of tags is almost exclusively detected using optical (laser) apparatus. This can be done using a microscope with image processing algorithms or with optical detectors in a flow cytometer. Several conventional cytometers exist in the market offered

by companies such as Guava [2], and Invitrogen [3] that can be used for cell counting, sorting (fluorescent activated cell sorting) and analysis. As an example in Cedex Assay the cell culture is exposed to Trypan blue and then monitored under microscope with image acquisition using a computer to count the viable cells [4,5].

The second broad method is electrical detection. As the composition or status of a cell changes, its electrical properties change, and this can be used to analyze a cell. This method is sometimes done through impedance flow cytometry, which probes the dielectric properties of cells [6]. There are commercial impedance base flow cytometers available, such as AmphaZ30 offered by Amphasys [7]. This integrated flow cytometer is part of a bulky single cell analysis tool, that measures the impedance magnitude and phase of a sample in 0.5-30 MHz range [8]. Another example is the fully electrical capacitance flow cytometer introduced by Thomson et al. that is used to determine single cells viability [9].

Electronic systems have advantages over chemical-optical techniques. Chemical-optical assays require dyes that can contaminate cell samples and can affect basic biological process within the cell. These assays can be time consuming as the dyes must be incubated with the cells. Also the dyes can be expensive. Optical detectors have spatial microscale resolution problems as cells are near resolution limits. They suffer from video acquisition rates limits, and huge files sizes storing problems [10]. These detectors are also very expensive to integrate. On the other hand, electronic assays are markerless, inexpensive and integratable [11].

Electrical methods can be categorized to four main approaches:

### **1.2.1 Dielectrophoresis (DEP)**

DEP is the force applied to a particle in a non-uniform electric field due to its dielectric contrast with its surrounding medium. Biological changes in the cell lead to changes in its dielectric

properties. Dielectric changes are often characterized using the Clausius–Mossotti factor<sup>1</sup>. Depending if a cell is polarizable more or less than the surrounding medium, they will be attracted or repelled from regions of higher electric field. The Clausius–Mossotti factor is positive for attractive DEP and negative for repulsive DEP. This can be used as a tool for detecting different cell dielectric properties.

For example, Fatimah et al. used DEP to monitor the leukaemic (K562) cell membrane and cytoplasm changes during apoptosis induced by staurosporine. They showed that the cytoplasm conductivity increases during the first 12 hours due to ions influx/efflux, as well as its capacitance due to cell shrinkage [12].

Some groups use DEP to separate cell samples known as Dielectrophoretic Field Fractionation (DEPFFF). This is done by using different DEP forces applied on cells with different Clausius–Mossotti factor and different sizes. Gascoyne et al used DEPFFF to isolate circulating tumor cells from normal blood cells [13].

Ahmet et al. used Dielectrophoresis to differentiate mouse melanoma clones based on their melanin content [14]. They scanned the real part of Clausius–Mossotti factor at different frequencies for two separate samples with different melanin contents, and showed that the frequency where forces changes from attractive to repulsive changed with melanin content.

Dielectrophoresis has also been used to detect drug resistant cells [15]. Hoettges et al used DEP to detect the effect of antibiotics on E. Coli bacteria by monitoring the apoptosis process to see which antibiotics are capable of suppressing bacteria growth. This method just took an hour compared to the conventional methods –based on sample culturing and testing it with different antibiotics- that take 24 hours. They have also been able to extract cell electrical properties like

---

<sup>1</sup>  $CMF = \frac{\epsilon_p^* - \epsilon_m^*}{\epsilon_p^* + 2\epsilon_m^*}$ , in which  $\epsilon_p^*$  and  $\epsilon_m^*$  are the particle and medium complex permittivity respectively.

cytoplasm conductivity and permittivity and membrane thickness by curve fitting the CMF versus frequency.

In summary DEP forces can be used to track changes in a number of different cell systems.

### **1.2.2 Electro-Rotation (EROT)**

Electrorotation is similar to DEP in nature. It is caused due to a cell dielectric contrast with its surrounding medium in a non-uniform electric field. Except that the cell is centered and the forces caused by AC signals that are at  $90^\circ$  phase shift induce a torque on the cell. The direction of the rotation and the magnitude of torque is defined by the cell CMF, and physical properties. This method has been used to measure dielectric spectrum of the cell versus frequency.

As an example, Becker et al used this method to differentiate breast cancer cells from normal blood cells. They used ROT to find the difference in cells dielectric properties. Then they exploited these differences to separate the cells by DEP and hydrodynamic forces [16].

### **1.2.3 Impedance Spectroscopy**

Detects cell electrical properties, like conductivity and permittivity by applying an AC electric fields to electrodes in close proximity to the cells. The impedance between the electrodes then becomes a function of the cells in proximity to the electrodes. Then the frequency of the applied fields is swept and the dielectric spectra can be monitored over a wide frequency range. Based on the stimulation frequency, the measurements highlight different dispersion modes,  $\alpha$ ,  $\beta$  or  $\gamma$ .  $\alpha$ -dispersion is detection at lower kHz frequency range which is associated with electrodes polarization effects [6]. At this frequency range also the media in which cells are suspended or in total the biological media might be damaged due to electro-thermal effects or ionization [17].  $\beta$ -dispersion is associated with a kHz to a few MHz detections which is related to the membrane capacitance surrounding the cytoplasm [6]. This capacitance defines Maxwell-Wagner relaxation

frequency [18].  $\gamma$ -dispersion is related to monitoring the inside of a cell at GHz frequency range, when all the discussed surface related capacitance effects are bypassed. This dispersion is due to the water molecules and other dissolved molecule reorientation at GHz frequencies [6].

Impedance spectroscopy techniques is generally used in two modes to characterize cells:

**1- Electric Cell Substrate Impedance Sensor (ECIS):** in this technique gold or platinum microelectrodes impedance is measured against a counter electrode, when cells are placed on microelectrodes. Measuring cells attachment to the microelectrodes by impedance is an indication of cells health. Impedance measurement is mainly done through off-chip signal generators or impedance analyzers. Commercial ECIS are available such as the ones through Applied Biophysics [19]. Esphahani et al used ECIS to monitor Human Glioblastoma cancer cells responses to ion channel inhibitor drug treatments [11]. In their experiments, they used a multi electrode chip with cells sitting on the electrodes. Drugs caused the cell to electrodes interaction to change, which was detected as changes in the impedance between electrodes at low frequencies. This method helped them to find out the effective chemotherapy dose [11].

**2- Impedance Flow Cytometry:** Impedance spectroscopy is used sometimes in conjunction with flow cytometry. This is monitoring the electrical properties when the cells pass through a channel. It makes the design capable of characterizing a large number of cells at a time. In this method cells are suspended in a stream of fluid, and passes through the probe electrodes in a microfluidic channel. Two pairs of electrodes are commonly used, one as reference, to increase SNR. There are two general ways to implement electrodes inside the microfluidic channel, parallel plate electrodes and coplanar electrodes. In parallel plate electrodes the impedance is not dependent on the position of a cell as long as the effect of

fringing field could be neglected. This can be reduced by increasing the electrodes size vs. cell diameter. Coplanar electrodes are simpler in fabrication but the measured impedance with them is dependent on the particle's position in the channel. In this essay the second approach is selected. Holmes et al used single cell impedance cytometry to identify CD4 (antigens on) T-lymphocyte cells versus normal blood cells for the diagnosis of AIDS [20]. The antibody beads attached to the CD4 cells resulted in a change that was detected using the impedance. This method is called impedance labeling.

#### **1.2.4 Electro-physiometry**

There are many other electrical and electrochemical techniques for designing biosensors to analyze cells in stationary mode [21]. These techniques are aimed to monitor cell physiology (physiometers) useful in monitoring activities of neural cells and in drug monitoring.

They include:

- 1- Patch Clamp:** is based on probing the cell membrane using a sealed pipette for measurement of ion channel currents and transmembrane voltages. To place probes in right position, single cells are monitored under optical microscopes in a vibration isolated table.
- 2- Microelectrodes Array (MEA):** in this technique gold or platinum metal layers on the substrate are used to measure electrical responses from cells (such as neurons) or to monitor a cell sample pH level. Microelectrodes in contact with cells are connected to external signal generators or data acquisition instruments for readout. Commercial MEAs are available such as Ayanda MEA60 [22].
- 3- Ion Selective Field Effect Transistors (ISFET):** is based on implementing arrays of FETs without a metal on their gate, in which cell ion activities and voltages are measured by the charge they induce in the channel through capacitive coupling. These sensors do not need

external amplifiers compared with MEA because of using FETs. Local measurements of cell sample pH can be made possible if  $\text{Si}_3\text{N}_4$  is used instead of  $\text{SiO}_2$  on the gates.

**4- Light Addressable Potentiometric Sensor (LAPS):** in this technique cell samples are placed on a  $\text{SiO}_2/\text{Si}$  interface, on which a light source induces photo currents to the substrate that depends on surface voltages. Because the light source can be located anywhere on the sample, this technique archives higher resolution than ISFETs, but there is only one measurement channel through the substrate.

**5- Quartz Crystal Microbalance (QCM):** is mainly used to monitor cell samples mass and growth rate. A piece of mm sized quartz crystal is used with sample on it, which the change in the sample mass shift the oscillation frequency of the crystal. These sensors have very stable response with temperature and achieve ng sensitivities, but can only be used to measure average behavior of the sample.

There are other techniques such as ENFET, IMFET, CHEMFET, etc. which discussing them is out of the scope of this thesis, but interested readers are referred to [21] for more information.

### **1.3 Comparison of Electrical Methods**

Electro-physiometer biosensors mainly use optical microscopes to place the cells in the right position on microelectrodes, or use bulky off-chip instruments for electrodes stimulation or impedance measurement. These techniques mainly report the average response of a sample and less likely are useful for single cell analysis. Also, they analyze cells in stationary mode which make them slow, compared with impedance spectroscopy or DEP when used with flow cytometry. Impedance flow cytometry is typically faster than DEP and electro-rotation analysis because it is a fully electrical method compared to the other two which make use of a mechanical force as well. Also DEP and EROT give only the real and imaginary part of the CMF respectively, at a few single

frequencies, after time-consuming measurements [18]. In impedance flow cytometry, the impedance of the particle can be scanned in a wide frequency range in a short time. Then the best frequency (i.e. where the highest sensitivity occurs) for measuring the changes in the amplitude or phase can be selected [18]. This method has been used to detect dielectric properties of cells, like their sizes, membrane resistance and cytoplasm conductivity [17]. Changes in each of these parameters are induced by physical changes in the cells. As an example, when a cell becomes cancerous, typically it swells and its size increases. Changes in each of these parameters affect impedance differently. For instance, when the membrane conductivity increases, the impedance magnitude decreases at low frequencies, while increase in cytoplasm conductivity causes impedance magnitude to decrease at higher frequencies [23].

#### **1.4 Resonator Based Capacitance DEP-Cytometer**

The work done by Thomson and Bridges research group at the University of Manitoba [9, 10] engaged both DEP and microwave frequency capacitance detection in microfluidic channel to monitor internal cell properties. In their work DEP forces were detected using a differential microwave frequency capacitance sensor [9]. This method has been used to monitor cells apoptosis process [24]. As discussed in chapter 2, this sensor is bulky (hardly portable) because it is designed with discrete connectorized components. It makes use of a resonator based microwave frequency sensor which is hard to tune. Besides, the sensor resonance frequency and sensitivity changes dramatically with small perturbations such as changes in media conductivity.

This work is mostly focused on design, implementation and integration of an electronics system for single cell detection and analysis. Separate systems have been designed and integrated on a printed circuit board, and also on a chip. The explanations of the works done in this thesis is as follows.

## 1.5 Thesis Structure and Contributions

The thesis is comprised of three journal papers and a conference paper and in total has seven chapters as follows:

### **Chapter 1: Introduction**

In the first chapter a background of the work done in this thesis is given. The main objectives for designing integrated electronic sensors for characterization of single biological cells are introduced. Then a literature review of different electrical techniques for characterization of cells is given following their comparison. At the end, disadvantages of the resonator based microwave frequency sensor developed in [10] is explained.

**Chapter 2: A Compact Microwave Frequency Reflectometer with atto-Farad Sensitivity: a Path towards an Integrated Dielectrophoresis Cytometer** © [2015] Elsevier. Reprinted with Permission, from [K. Mohammad, K. Braasch, E. Salimi, A. Bhide, B. S. Rizi, M. Butler, G. Bridges, D. Thomson, “A compact microwave frequency reflectometer with attoFarad sensitivity: A path towards an integrated dielectrophoresis cytometer”, Sensors and Actuators A: Physical, vol.232, pp.132-140, 2015] [25]

Disadvantages of the previously designed resonator based microwave frequency sensor [9, 10, 24] is explained in section 1.4. In this chapter a new microwave frequency sensor called reflectometer is introduced. The contributions of this paper are:

- Designing a microwave frequency capacitance sensor that makes use of SMD components rather than connectorized components in [9, 10]. This design is implemented on a PCB with a dimension of 9 cm×10 cm, and is shown to have enough sensitivity to be used as a DEP cytometer for analysis of single CHO cells.

- Compared with the resonator based sensor in [9, 10], which has to be tuned in two steps by adjusting the input RF frequency and by tuning a phase shifter, the new design is tunable only by adjusting the input RF frequency.
- Sensor sensitivity is shown to reduce less than the resonator based design [9, 10], when samples medium conductivity is increased.

**Chapter 3: Differential Ring Oscillator Based Capacitance Sensor for Microfluidic Applications** [K. Mohammad, D. J. Thomson, “Differential Ring Oscillator Based Capacitance Sensor for Microfluidic Applications”, in Press, IEEE Transactions on Biomedical Circuits and Systems, 2016] [26]

Microwave frequency sensor introduced in chapter 2, as the resonator based designs still makes use of a bulky lock-in amplifier and RF signal generator. The use of lock-in amplifier is very important in chopping the sensor signal to the frequency range where white noise is dominant, and in adjusting the sensor bandwidth to boost sensitivity.

Integration of all parts of the system was not possible, unless the detection system (capacitance sensor) could be completely integrated. In this chapter a ring oscillator based capacitance sensor is introduced which makes use of an external frequency counter and microfluidic chip but all of its components are easily integratable on chip.

The contributions of this paper are:

- Introducing a capacitance sensor design idea, which can be completely integrated on a chip. It is shown that compared with the previous capacitance sensors designs, which is reviewed in [25], this design idea can meet most of the required specifications of a capacitance sensor for use in single cell analysis and biomedical applications.

- The design idea is used to implement the new capacitance sensor on a PCB using SMD components, and the design operation is confirmed through detection of Isopropyl alcohol (IPA) in DI water contents from 100%-1% and 15  $\mu\text{m}$  PSS by the sensor.

**Chapter 4: Integrated 0.35  $\mu\text{m}$  CMOS Capacitance Sensor with atto-Farad Sensitivity for Single Cell Analysis** [K. Mohammad, D. A. Buchanan, D. J. Thomson, “Integrated 0.35  $\mu\text{m}$  CMOS Capacitance Sensor with atto-Farad Sensitivity for Single Cell Analysis”, Biomedical Circuits and Systems Conference, 2016] [27]

The proposed differential ring oscillator based capacitance sensor in chapter 3, proves the concept of using this architecture for detection of capacitance changes. The problem is still the sensor does not have enough sensitivity in detection of single cells, it has an equivalent voltage on sensing microelectrodes as the supply voltage, and makes use of an external microfluidic chip for detection. In this chapter an application specific differential ring oscillator based capacitance sensor is designed which includes a microfluidic part for driving cells over top of the chip for detection. The sensor is proved to have enough sensitivity in detection of single cells.

The contributions of this paper are:

- Optimizing the capacitance sensor introduced in chapter 3 for single cell applications, by using tapered ring oscillators in the design architecture.
- Implementing the new design on chip using 0.35  $\mu\text{m}$  CMOS technology, and confirming that sensor has enough sensitivity through detection of 15  $\mu\text{m}$ -10  $\mu\text{m}$  PSS and CHO cells.

**Chapter 5: GHz Frequency CMOS DEP Cytometer for Characterization of Single Biological Cells** [K. Mohammad, D. A. Buchanan, K. Braasch, M. Butler, D. J. Thomson, “GHz Frequency CMOS DEP Cytometer for Characterization of Single Biological Cells”, Submitted to Lab on Chip Journal, 2016] [28]

This chapter completes chapter 4 by adding more details of the design implementation and measurement results.

The contributions of this paper are:

- A fully electrical and integrated DEP cytometer is introduced. Compared with conventional DEP cytometers such as in [12, 13, 14] which make use of bulky optical microscopes, the detection system in this sensor is fully integrated using TSMC 0.35  $\mu\text{m}$  CMOS technology. Compared with the previously designed fully electrical DEP cytometers in [24, 25], this design integrates all the required components of a DEP cytometer including the detection sensor and the microfluidic part in an area of 2 cm $\times$ 2 cm. This is equivalent to more than 10 times reduction in system volume when compared with past works [24, 25, 27].
- The new DEP cytometer operation is confirmed by monitoring PSS and CHO cells signatures normalized peak difference histograms shifts in case of applying positive or negative DEP forces.

## **Chapter 6: GHz Frequency CMOS DEP Cytometer Noise Analysis**

In this chapter the noise sources in the designed DEP cytometer chip are identified, and the noise from these sources are compared with calculations. It includes noise measurement results both in time domain (jitter) and frequency domain (phase noise).

The contributions of this chapter are:

- Identifying the dominant sources of noise in the sensor.
- Developing equations to estimate sensor noise and sensitivity, and comparing noise measurement results with calculated numbers.
- Giving design insight on how to reduce sensor minimum detectable capacitance.

## **Chapter 7: Conclusions and Future Works**

The last chapter begins with a summary of the discussed works. Then the design specifications of the capacitance sensors introduced in chapter 2-5 are compared with the state of the art capacitance sensors from other research groups. This chapter ends with some propositions on how to improve the designed integrated sensor, and some of the potential applications of this design for one who wants to follow this pathway in future.

# **Chapter 2: A Compact Microwave Frequency Reflectometer with atto-Farad Sensitivity: a Path towards an Integrated Dielectrophoresis Cytometer**

## **2.1 Abstract**

A microwave frequency reflectometer with atto-Farad capacitance sensitivity has been designed and tested for detection of particles and cells in a microfluidic channel. The design is implemented on a printed circuit board. Capacitance sensitivity up to 1.25 aF is achieved in a 50 Hz bandwidth. The sensor was used for detection of 5.7  $\mu\text{m}$  polystyrene spheres and Chinese Hamster Ovary (CHO) cells flowing over co-planar electrodes in a microfluidic chip. The reflectometer was used in a dielectrophoresis cytometer. A statistical analysis of particle deflection demonstrated that the microwave sensing voltages are below the limit required to prevent actuating beads and cells by dielectrophoresis. The use of a reflected signal rather than one transmitted through a resonator has eliminated the bulky resonator and allowed for a much more integrated design. The sensor nulling is accomplished by changing the RF generator frequency and the need for stable and bulky mechanical phase shifters required for resonator designs is eliminated. The open line design is less sensitive to media conductivity compared to resonator based cytometer and the sensitivity changes by less than 34% for media conductivities from 0.1 to 3 S/m.

## **2.2 Introduction**

Simple low cost electronic detectors with single cell and particle sensitivity are important for highly integrated lab-on-chip systems. Optical analysis methods have single cell sensitivity, but are expensive and difficult to integrate into on-chip systems [29]. In addition, optical analyzers have spatial microscale resolution problems, suffer from video acquisition rate limits, and large data flow and analysis problems [29]. Electrical detection systems are typically markerless, much

easier to integrate into highly compact systems and have lower data processing requirements. Many groups have used impedance spectroscopy as a means for single cell detection and analysis [11, 17, 18, 20]. In this method, the impedance of cells can be detected in a wide frequency range in a short time. Then the best frequency (i.e. where the highest sensitivity occurs) for measuring the changes in the amplitude or phase can be selected [18]. This method has been used to detect dielectric properties of cells, characterizing their size, membrane resistance and cytoplasm conductivity [17]. Impedance measurements are typically done in the  $\beta$  and  $\gamma$  dispersion regions. One reason for this choice is that in  $\alpha$ -dispersion, the impedance changes are concealed by double layer capacitance effects [6]. Media electro-thermal effects and its ionization may also have an impact [30]. To characterize a large number of cells in a short time, impedance spectroscopy is typically used in combination with flow cytometry [18]. In this method, cells are suspended in a stream of fluid, and pass over the detection electrodes in a microfluidic device. With appropriate dilution of the cells flow cytometry makes it possible to do single cell detection and analysis. Single cell analysis is typically more sensitive than bulk measurements, and is capable of measuring those properties of cells that are hidden in the average response of the cell culture [11]. Capacitive sensing is a subcategory of impedance spectroscopy. Several methods have been developed for high sensitivity capacitance detection for different applications. Differential charge based capacitance measurement was used by York et al for particle detection with 16 aF resolution [31]. Balanced bridge was used by Wei et al. with lock-in detection technique for Pico liter liquid monitoring. They achieved 1 aF resolution in 100 Hz resolution [32]. AC based method was used by Marioli et al. in a CMOS lab on a chip for single cell detection. They reported 420 aF changes in capacitance in presence of a cell with 39 dB SNR [33]. Prakash et al. used charge sharing method at 1 kHz with fF resolution for measuring cell to substrate interaction [34]. Frank et al. used

oscillator based capacitance sensor at 10 kHz and achieved 50 aF resolution [35]. Carminati et al. developed a CMOS current front end circuit that operates up to 1 MHz. They achieved 5 zF in 1.6 Hz bandwidth [36]. Resonance based method has been considered for capacitive detection both at low and higher frequencies [9, 10, 37-39]. Ghidini et al. used an LC resonance lock-in technique at 2 MHz and achieved 100 aF resolution [37]. Thomson and Bridges developed a resonance based microwave frequency sensor for microfluidic measurements and single cell detection. It operates around 1-2 GHz frequency and resolution up to 125 zF in 50 Hz bandwidth is achieved [9, 10, 39]. At GHz frequencies the membrane capacitance is bypassed and polarization is dominated by the dielectric properties of the cytoplasm [23]. They used the resonator based microwave detection apparatus in a dielectrophoresis cytometer to monitor Chinese Hamster Ovary (CHO) cells during the onset of apoptosis [24].

The details of the resonator based capacitive cytometer circuitry were presented in [9, 24, 39]. The design is based on an interferometric architecture with a signal path and a reference path. A signal proportional to the phase difference between the paths is produced using a mixer. In the signal path a quarter wavelength microwave coupled transmission line resonator is used which is coupled to the microfluidic channel electrodes using brass wires. Presence of a cell above the electrodes perturbs the field on the resonator leading to a phase shift detected in the output of the mixer. The rate of change in phase vs. capacitance is estimated using [34]:

$$\frac{\partial \phi}{\partial C} = -2Qf_0Z_0 \quad (2.1)$$

In which  $Q$  and  $f_0$  are the quality factor and resonance frequency of the resonator respectively. However, when these sensors are coupled to electrodes in microfluidic channels losses due to coupling of fields into the media filling the microfluidic channel can be significant [24, 39]. For one resonator sensor addition of DI water lowers the quality factor of the resonator from 50 to 10

in this case [9]. The reduction in  $Q$  causes sensitivity degradation by more than a factor of 6. Changes in medium conductivity also influence losses and degrade the measurement sensitivity. This can be an issue with mammalian cells as they are suspended in highly conductive buffer solutions, with 0.1 to 3 S/m being the most common conductivity range. To overcome this problem Low- $Q$  resonators ( $Q \sim 9$ ) have been used, which are less sensitive to losses. These resonators are less prone to reductions in quality factor. But on the other hand as its quality factor is less, it is less sensitive (see Eq. 2.1). A disadvantage of resonator based interferometers is the need for very stable and bulky phase tuning to null out the sensor.

In this work a non-resonant microwave frequency reflectometer with sensitivity suitable for single cell capacitive cytometry is demonstrated. Compared to the other microwave IDC (Interdigitated Coplanar Waveguides) based sensors the current reflectometer demonstrates single cell sensitivity without the need for a bulky Vector Network Analyzer (VNA) [40-42]. The sensor functions by detecting electrical length changes induced in interdigitated coplanar transmission lines by presence of a cell. The reflectometer does not require phase tuning and can be nulled through frequency tuning alone. The application of the microwave reflectometer for the detection of 5.7  $\mu\text{m}$  (in diameter) polystyrene spheres (PSS) and CHO cells are demonstrated. The sensitivity of the reflectometer for particle detection and also its sensitivity to media conductivity are compared with resonator based sensors.

## **2.3 Methods and Experiments**

### **2.3.1 Reflectometer Design Details**

The reflectometer sensor operates using the electrical path length differences in an interferometer at  $\sim 2$  GHz. The signal from a RF generator (E8663B, Agilent Technologies) is applied at 13 dBm level to a bandpass filter (SYBP-2250, Mini-Circuits) to remove low frequency and high frequency

noise and harmonics. It is then split into a signal and reference path using an 18 dB directional coupler (D18P, Mini-Circuits). The -18 dB coupling reduces the power on the signal path below the level that causes dielectrophoretic actuation of the particles being detected. Using a directional coupler for power splitting reduces circuit complexity and enhances signal to noise ratio as no attenuation is required for controlling the power level in the sensing path of the interferometer. The signal from reference path is applied to LO (Local Oscillator) input of a mixer (MCA1-24MH, Mini-Circuits). The power in the signal path is coupled to the electrode in the microfluidic channel via a circulator (C2AB16, Sonoma Scientific). As in the resonance based sensors, the RF signal is modulated and detected using a lock-in amplifier (SR830, Stanford Research Systems) with a 50 Hz bandwidth. The modulation is done with an absorptive TTL switch (M3SWA-2-50DR, Mini-Circuits) on the sensing path before the channel. The signal reflected from channel is applied to a LNA (TAMP-242GLN, Mini-Circuits) through the circulator to enhance signal to noise ratio. The circulator helps isolate the signal and prevents reflected signals from flowing back and forth in the sensing path. The channel microelectrodes are connected to circuitry using a separate 50  $\Omega$  on PCB transmission line and a pair of brass wire probes. As particles suspended in media, flow through the microfluidic channel and pass over the electrodes, the phase of the sensing path shifts. By applying the signal from the sensing path to the RF input of the mixer, an output signal proportional to phase shift of sensing signal compared to reference signal is produced. A schematic of the design is shown in Fig. 2.1. The section enclosed in the dash lines (except for the microfluidics and 50  $\Omega$  interface board) is implemented on an FR4 printed circuit board (PCB) with 0.0602" thickness. A photograph of the PCB with the related components is shown in Fig. 2.2. On the board two sets of test transmission lines labeled H and I, with widths of 2.5 mm and 3 mm are implemented. The output from PCB coupled through 50  $\Omega$  line to two brass wires used to

interface to electrodes on a microfluidic channel. This interface is mounted on an x,y,z positioner to align the brass wires with the contact pads of the microfluidic electrodes. The entire interferometer and microfluidic system is set up inside a metallic cabinet suspended on a vibration isolation table.

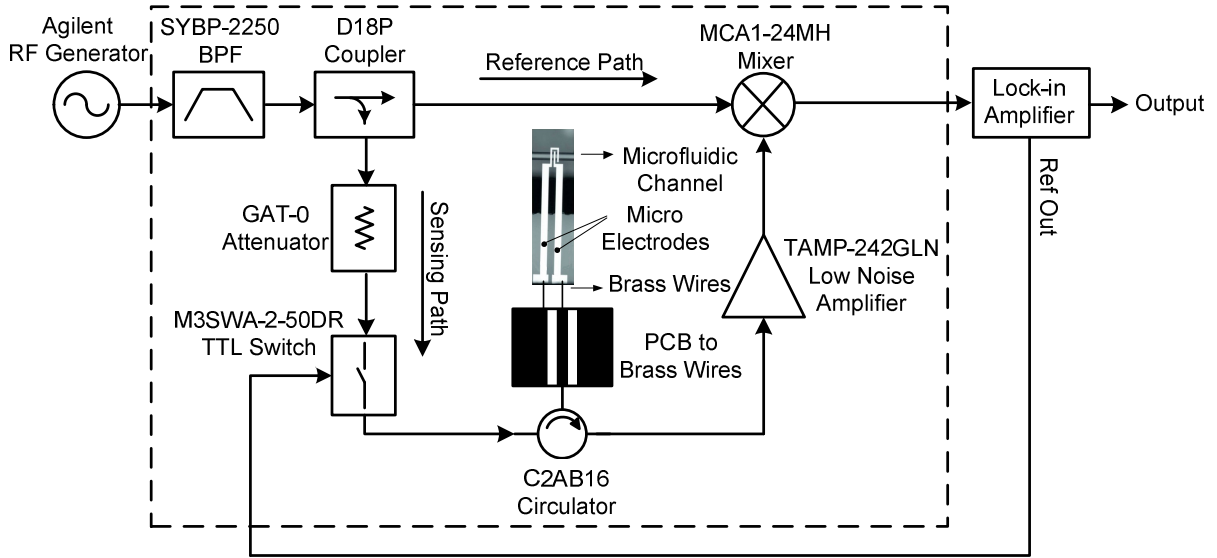


**Figure 2.1:** The schematic of the reflectometer microwave frequency sensor is shown. The section enclosed by dash lines is implemented on a PCB (except for the microfluidics and 50 $\Omega$  interface board).

### 2.3.2 Power Levels on Board

The power level adjustment on the board is important to prevent particles and cells from being actuated by dielectrophoretic forces generated by the GHz frequency sensing signals, as this will interfere with the low frequency DEP actuation used for cell diagnostics [24]. The maximum RF power that can be applied to the sensing electrodes in the channel is calculated in [39] to be -4 dBm. Power levels greater than this will significantly actuate the particles.

In this design the input power level is set 13 dBm. Assuming 1 dB loss of the connecting cable to PCB, 12 dBm reaches the board theoretically. The signal on reference path and sensing path was

calculated to be 9.5 dBm and -8.2 dBm respectively assuming filter and directional coupler's loss [43,44]. On striking the channel the sensing signal is mostly reflected due to the high impedance of the electrodes [9], and is directed to low noise amplifier by the circulator. The switch also attenuated the signal by 3 dB due lock-in amplifier modulation, hence about -12.6 dBm reaches the circulator. Circulator loss from one port to the other is measured to be 1 dB. So the signal applied to the channel was calculated to be -13.6 dBm. This is roughly 10 times less than -4 dBm which means the actuation at microwave frequencies will be insignificant. In the output of the circulator about 23 dB margin for signal amplification was left if the signal is kept below the 1 dB compression point of the mixer at 9 dBm. A 13 dBm input power and a 28 dB gain for the amplifier might overload the RF input of the mixer. Therefore, the power on board was optimized using attenuators.

To sample the signal power levels on board at different nodes, 20 dB directional couplers (SYD-20-33, Mini-Circuits) is used. Power is measured using a power meter (HP438A, Agilent Technologies). The list of measured power levels on board at 1.8 GHz for a 0 dB attenuator is shown in Table 2.1 in detail. As shown, the voltage applied to the channel is about -16 dBm. LNA output power is about 8.4 dBm, which is still less than 1 dB compression of the RF input of the mixer.

**Table 2.1:** Measured power levels at different nodes of the board.

<b>Node Power</b>	<b>Measured (dBm)</b>
Input to the Board	11.62
Output of the Bandpass Filter/Input of the Coupler	9.45
Output of the Switch/Input of the Circulator	-14.33
Output of the Circulator/Input of the Channel	-16.14
Output of the LNA/Input of the Mixer	8.40

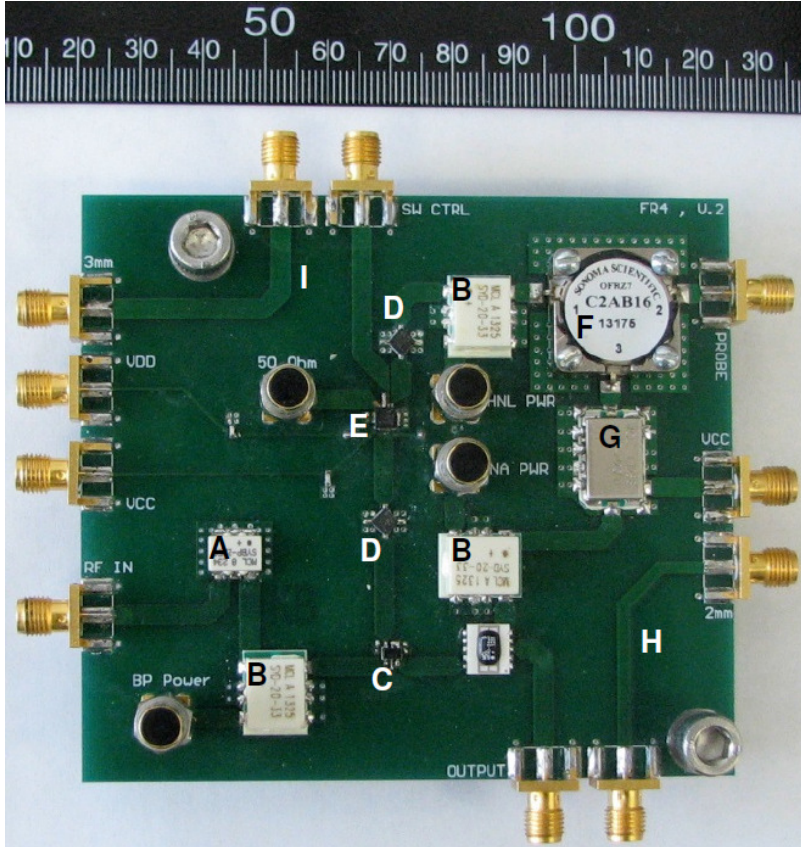


**Figure 2.2:** Single cell interferometer integrated on a PCB. A: bandpass filter, B: 20 dB coupler, C: 18 dB coupler, D: attenuator, E: switch, F: circulator, G: LNA, H: 2.5 cm wide 50 $\Omega$ , I: 3 cm wide 50  $\Omega$ .

### 2.3.3 Sensor Tuning

The interferometer is nulled by adjusting the frequency of the RF generator, eliminating the need for a physical phase shifter (which is essential in the resonator based designs). The operating frequency is chosen by designing the reference and sensing initial path lengths differences to be integer multiple half wavelengths at the operating frequency. The electrical length depends on the permittivity of the transmission lines which is about 4 for the FR4 board. The physical length difference for two paths including the length of the connecting cable (to brass wires) is about 35cm, so:

$$\frac{\Delta L}{\sqrt{\epsilon}} = \text{Electrical Length} = \frac{C}{f} \times \frac{n}{2} \quad (2.2)$$

In which  $\Delta L$  is the difference in electrical length,  $\epsilon$  is the permittivity of the board,  $C$  is the speed of light,  $f$  is the nulling frequency. The first 2 nulls would occur when  $n$  is 1 or 2, depending whether nulling happens at  $\pi$  or  $2\pi$  phase differences between the paths. Therefore:

$$\frac{35\text{cm}}{\sqrt{\epsilon}} = \frac{3 \times 10^8}{f} \times \frac{n}{2} \Rightarrow f = 0.9 \times 10^9 n \quad (2.3)$$

The closest nulling frequency based on the operation frequency of the board components would happen for  $n=2$ , which is  $\sim 1.8$  GHz. The nulling in this design was at 1.86 GHz, which is close to the calculated value.

### 2.3.4 Sensitivity Measurement Method

As for the resonator based cytometer [9, 10, 39], an intended application of this sensor is the detection of particles in microfluidic channels. The sensor is tested by using particles flowing over the electrodes in a microfluidic chip. The details of the microfluidic chip fabrication are discussed in [45]. The capacitance profile for  $5.7 \mu\text{m}$  PSS passing over the coplanar 2-gap microelectrodes is simulated using a finite element simulation package (COMSOL Multiphysics) [39]. For a PSS altitude (center to bottom) of  $7 \pm 1 \mu\text{m}$  the estimated capacitance change is  $48 \pm 4$  aF. So if the sensor signal level is 1 V for example, in this case the sensitivity is 48 aF/V. Hence the minimum detectable capacitance is calculated by:

$$\text{Minimum Detectable Capacitance} = \frac{48 \text{ aF}}{(\text{Signal} / \text{Noise})} \quad (2.4)$$

## 2.4 Results and Discussion

### 2.4.1 Sensitivity Detection

A sample output signal from the sensor for a  $5.7 \mu\text{m}$  bead is shown in Fig. 2.3. The distance of the particle above the electrodes for the signature is matched using the ratio of the signals at point A

and point B. In this case the estimated altitude is  $5\ \mu\text{m}$  [39]. The estimated capacitance change is about  $56\ \text{aF}$  as mentioned. The observed signal magnitude is  $1\ \text{V}$ . The RMS noise was estimated to be  $0.025\ \text{V}$ , measured over a  $1\ \text{s}$  window, using a response time of  $3\ \text{ms}$ . With  $56\ \text{aF/V}$  sensitivity, this corresponds to a minimum detectable capacitance change of approximately  $1.40\ \text{aF}$ , which is an acceptable limit for detecting the  $10\text{--}100\ \text{aF}$  capacitance changes induced by cells and PSS.

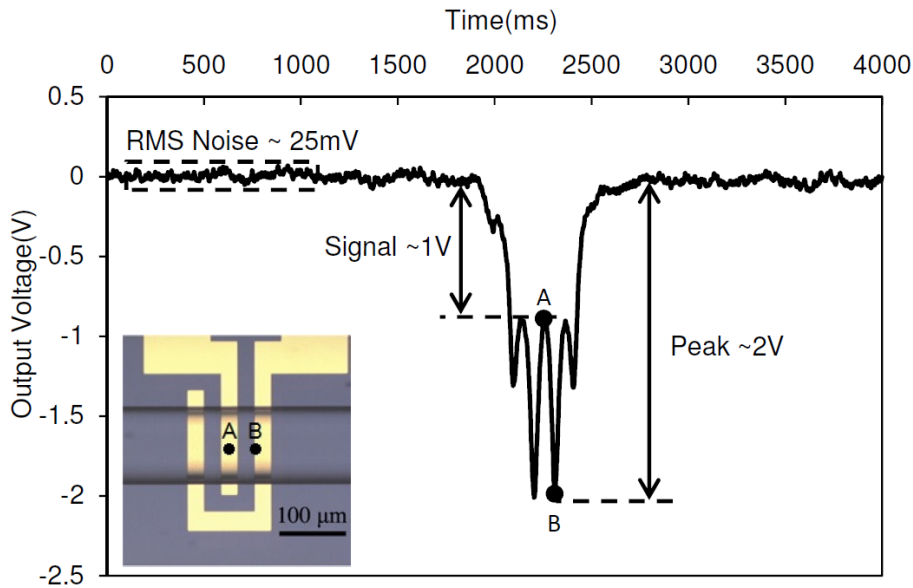


**Figure 2.3:** A sample detected signal in the output of lock-in amplifier from a  $5.7\ \mu\text{m}$  PSS.

#### 2.4.2 Detection of Mammalian Cells

Chinese Hamster Ovary (CHO) cells expressing a human llama chimeric antibody (EG2) are used for this work to compare the results with other sensor designs. Details of cell culture preparation are explained in [24]. In this case two pairs of interdigitated microelectrodes are used that produce a pair of peaks for each particle or cell [24]. A sample signature for a CHO cell is shown in Fig. 2.4. A peak to peak signal of  $2\ \text{V}\text{--}5\ \text{V}$  is detected depending on the cell size. Peaks are at same level ( $P1\approx P2\approx 1.8\ \text{V}$ ), which confirms that the cell is not actuated as it flows from the first to the second pair of electrodes.

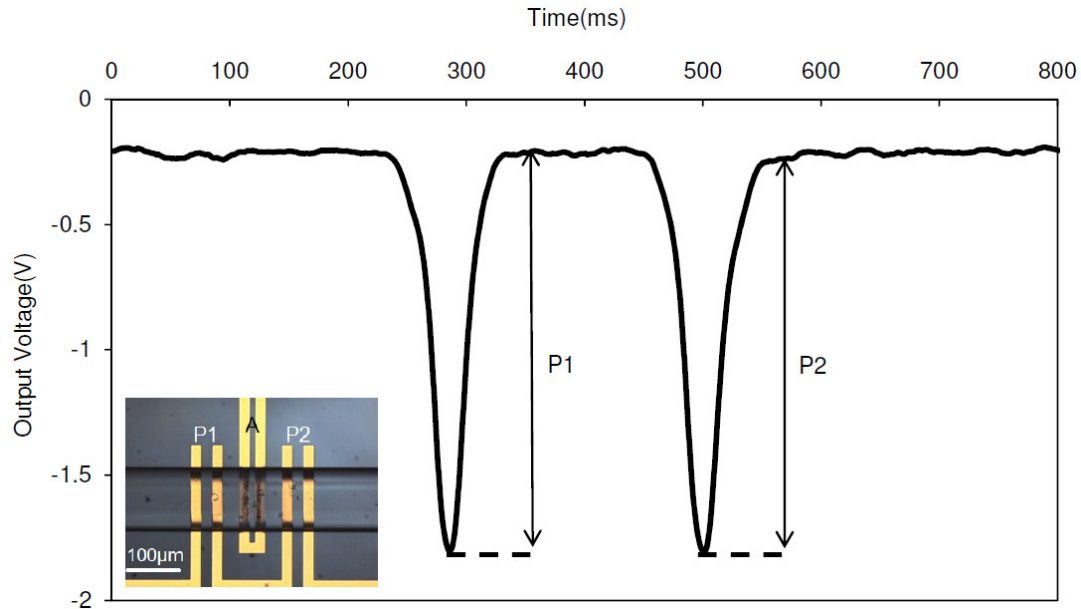


**Figure 2.4:** A sample signal of a CHO cell using the microwave reflectometer sensor obtained from the differential microelectrodes. “A” is the actuation electrode.

### 2.4.3 Verification of Detection Without Perturbation

Before using the sensor for DEP cytometry, it was verified that there was no actuation of the cells by the microwave detection signal. Using the interdigitated electrodes, with the center DEP electrode grounded, the peaks should theoretically be at same levels, neglecting effects of particle rotation [46]. This confirms that the only possible source of actuation is the low frequency center electrode voltage and not the microwave frequency signal, when the sensor is used for DEP cytometry.

To confirm detection without actuation, a normalized peak difference quantity called force index is used to quantify any DEP induced motion. The force index is the difference in the magnitude of the detected peaks divided by the sum of the magnitude of the peaks. A positive or negative force index is associated with positive or negative DEP actuation respectively [24]. The smaller the actuation of the particles the closer the value of normalized peak difference will be to zero. Two

sets of measurements were done, one using 5.7  $\mu\text{m}$  beads and another using CHO cells to detect their actuation utilizing the microwave reflectometer.

For data analysis a semi-automated Matlab GUI was utilized [47]. The normalized peak difference histograms obtained from the detection of 5.7 $\mu\text{m}$  beads are shown in Fig. 2.5. Polystyrene spheres are suspended in DI water. In this case about 300 signatures are collected and the normalized peak differences mean value and standard deviation were -0.008 and 0.056 respectively. The mean is nearly within the experimental uncertainty, estimated at 0.006, indicating that there is negligible actuation of the particles.

This test was also carried out with CHO cells suspended in low conductivity medium with  $\sigma=0.1590$  S/m. A population of 1450 of CHO cells signatures was collected. The histograms are shown in Fig. 2.6 (A). In this case the total normalized peak differences mean value and standard deviation is found to be -0.015 and 0.050 respectively. The histograms have means that are near zero. The same experiment with the resonator based design and CHO cells with population of about 1520 suspended in low conductivity medium with  $\sigma=0.1736$  S/m resulted in mean value and standard deviation of -0.015 and 0.068 respectively. The related histograms are shown in Fig. 2.6 (B). This demonstrates that reflectometry didn't have a negative impact on the discrimination capability of the sensor compared with the resonator based design.

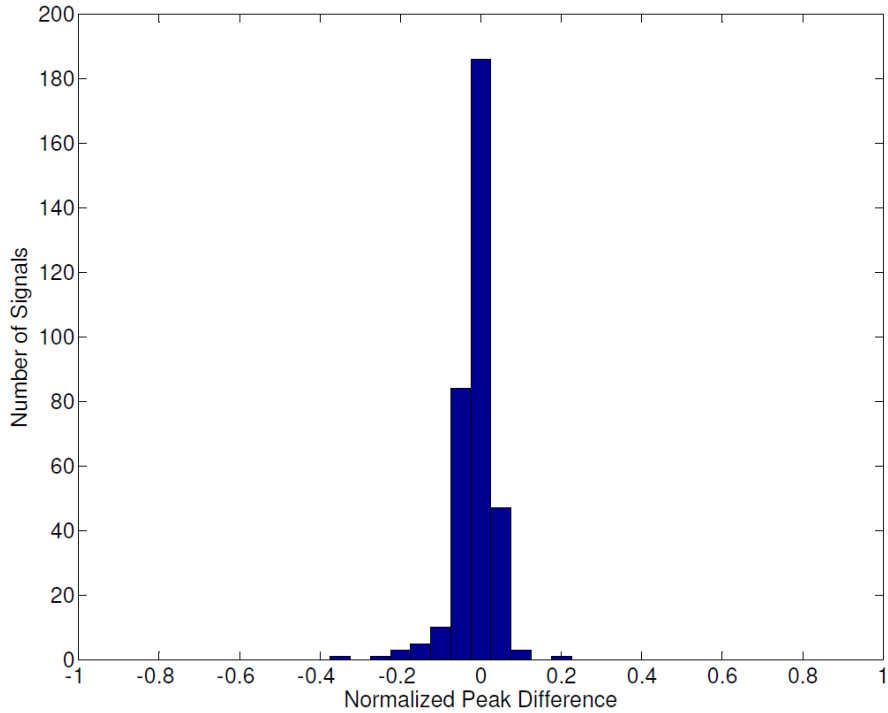


**Figure 2.5:** Statistical analysis of the normalized peaks difference for 5.7  $\mu\text{m}$  beads signature with no DEP signal.

After confirming that the sensor is not actuating the cells at microwave frequency, it was used for DEP cytometry. 5.7  $\mu\text{m}$  PSS beads suspended in DI water were actuated with DEP potentials (3 MHz, 4 Vp-p). The resulting histograms from 580 beads signatures are shown in Fig. 2.7. It shows that the particle actuation by DEP is clearly resolved with normalized peak differences mean value and standard deviation of about -0.21 and 0.97 respectively. This is evident by comparing the shift in the histograms between Fig. 2.7 versus Fig. 2.6.

#### 2.4.4 Sensitivity to Changes in Media Conductivity

Resonator based sensors are sensitive to factors that change the resonator resonance frequency and quality factor, such as the media conductivity.

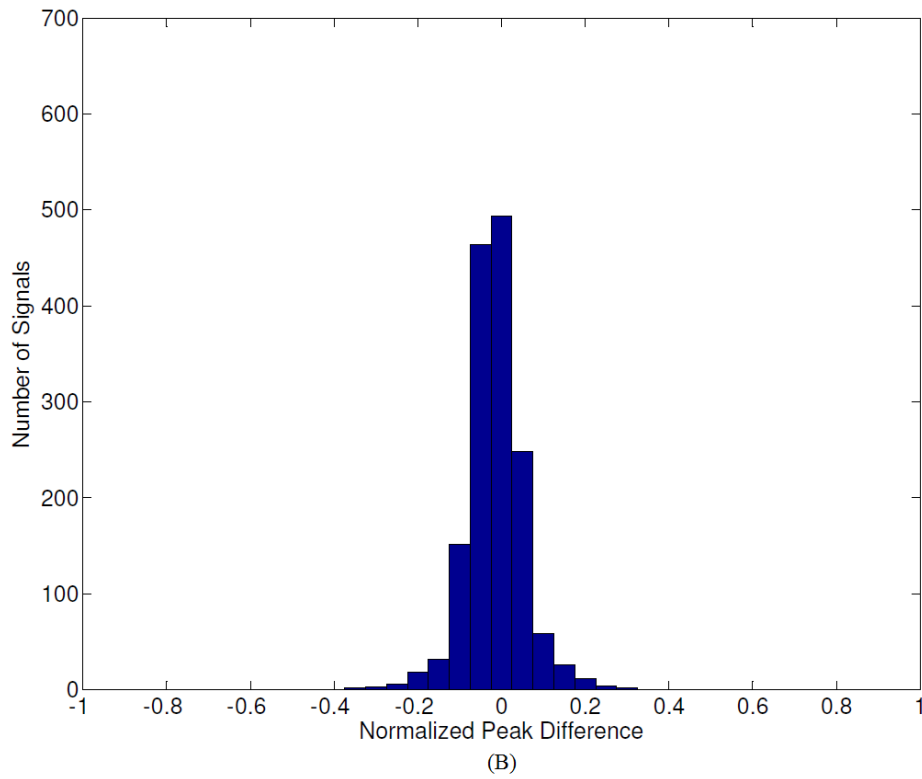
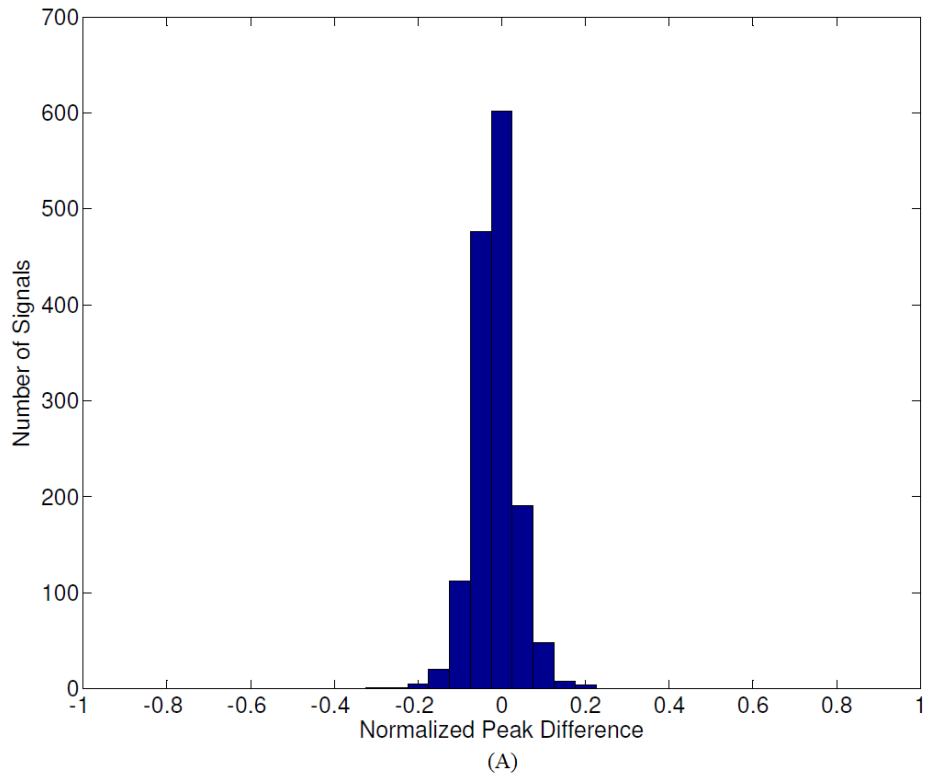


**Figure 2.6:** Statistical analysis of normalized peak differences for CHO cells signatures from the microwave reflectometer and resonator based design with no DEP signal. (A) reflectometer. (B) resonator based sensor.

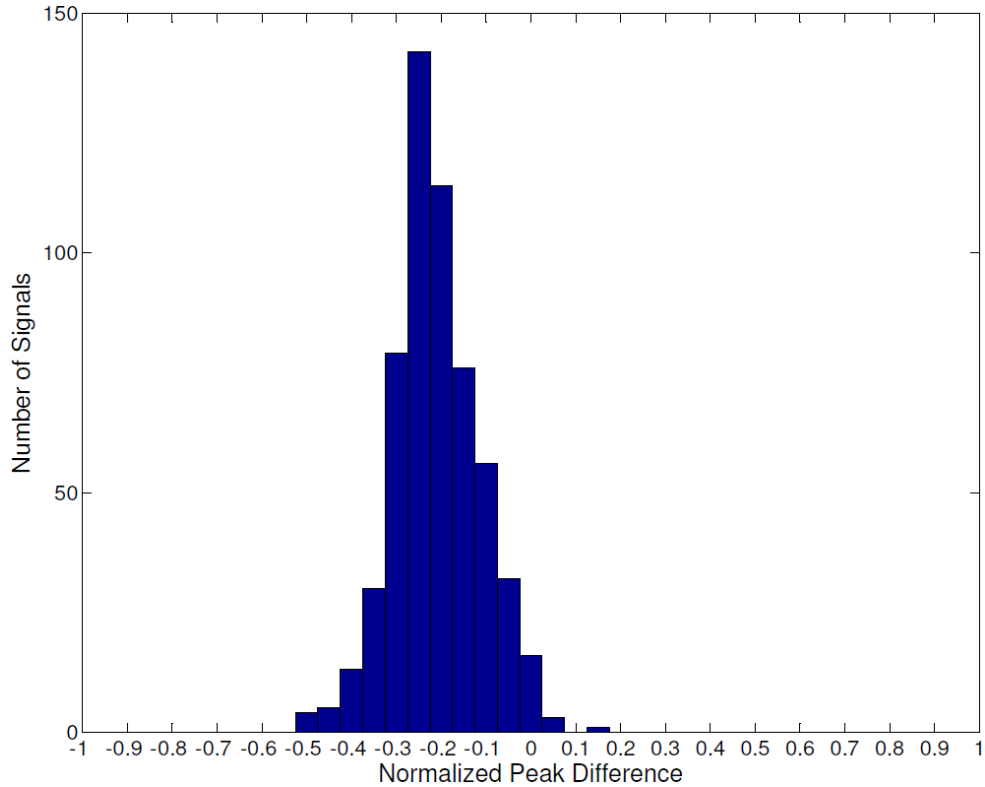


**Figure 2.7:** Statistical analysis of the normalized peak differences for 580 PSS signatures obtained from the microwave reflectometer. DEP signal is applied at 3 MHz and 4 Vp-p.

The higher the media conductivity, the lower resonator quality factor and the lower the resonance frequency. A lower quality factor leads to degradation of sensor sensitivity. The open ended design is less sensitive to electrical loss and is therefore expected to be less sensitive to media conductivity. It is important to minimize this sensitivity, as mammalian cells flow in solutions with high salt concentrations that are required to maintain viability.

Media was simulated using sodium chloride solutions with conductivities of 0.1 S/m, 0.3 S/m, 1 S/m and 3 S/m. This range of conductivities cover those found in most biological and dielectrophoresis applications. 5.7  $\mu\text{m}$  beads are used with 2-gap microelectrodes in all measurements. Measurements are done using electrodes described in Fig. 2.3, with system inputs power of 13 dBm and lock-in amplifier 50 Hz filter bandwidth. The variation of the sensitivity

with media conductivity is shown in Fig. 2.8. The results for each type of sensor are tabulated in Table 2.2. The last column shows the normalized changes in sensitivity.

As shown the sensitivity changes for reflectometer sensor is lowest (1:1.34), while for the High-Q resonator based system is highest (1:1.95). The reflectometer design is more than two times less sensitive than the next best, which is the low Q resonator. Decreasing the resonator quality factor reduces the rate of change of phase with frequency with increasing media conductivity and hence degrades the sensitivity when media conductivity changes from about 0 to 3 S/m. However, in the reflectometer the electrical path length difference is much less sensitive to the media conductivity as the results demonstrate. Based on these results, this detection system is more usable over the full range of media conductivities used for mammalian cells.

**Table 2.2:** Sensitivity of High-Q, Low-Q resonator based sensors and microwave reflectometer sensor when DI water, and 0.1 S/m, 0.3 S/m, 1 S/m and 3 S/m saline solution are used.

<b>Systems Sensitivity(aF)</b>	<b>DI Water</b>	<b>0.1S/m</b>	<b>0.3S/m</b>	<b>1S/m</b>	<b>3S/m</b>	<b>Sensitivity Changes</b>
High Q Resonator	0.162	0.179	0.225	0.300	0.365	0.190 aF-0.374 aF (1:1.95)
Low Q Resonator	0.208	0.161	0.190	0.230	0.311	0.181 aF-0.310 aF (1:1.71)
Reflectometer	1.42	1.16	1.24	1.33	1.69	1.24 aF-1.66 aF (1:1.34)

#### **2.4.5 Reflectometer Design in Comparison with Resonator Based Sensors**

Microwave reflectometer design has several advantages over the resonator based sensors. The resonator designs use a quarter wavelength resonator and a bulky phase shifter is required for stability and low noise. The microwave reflectometer is portable and more compact. The reflectometer components are such that they can be easily integrated into lab-on-chip systems.

The other major difference is the adjustment needed to null the interferometer used in sensors. The resonator based sensor is tuned using a two stage process. First, the resonance frequency of the

quarter wave resonator is found by sweeping the frequency, and finding the maximum point in the power transmission. The microwave source is then set to that frequency. Parasitic resonances can

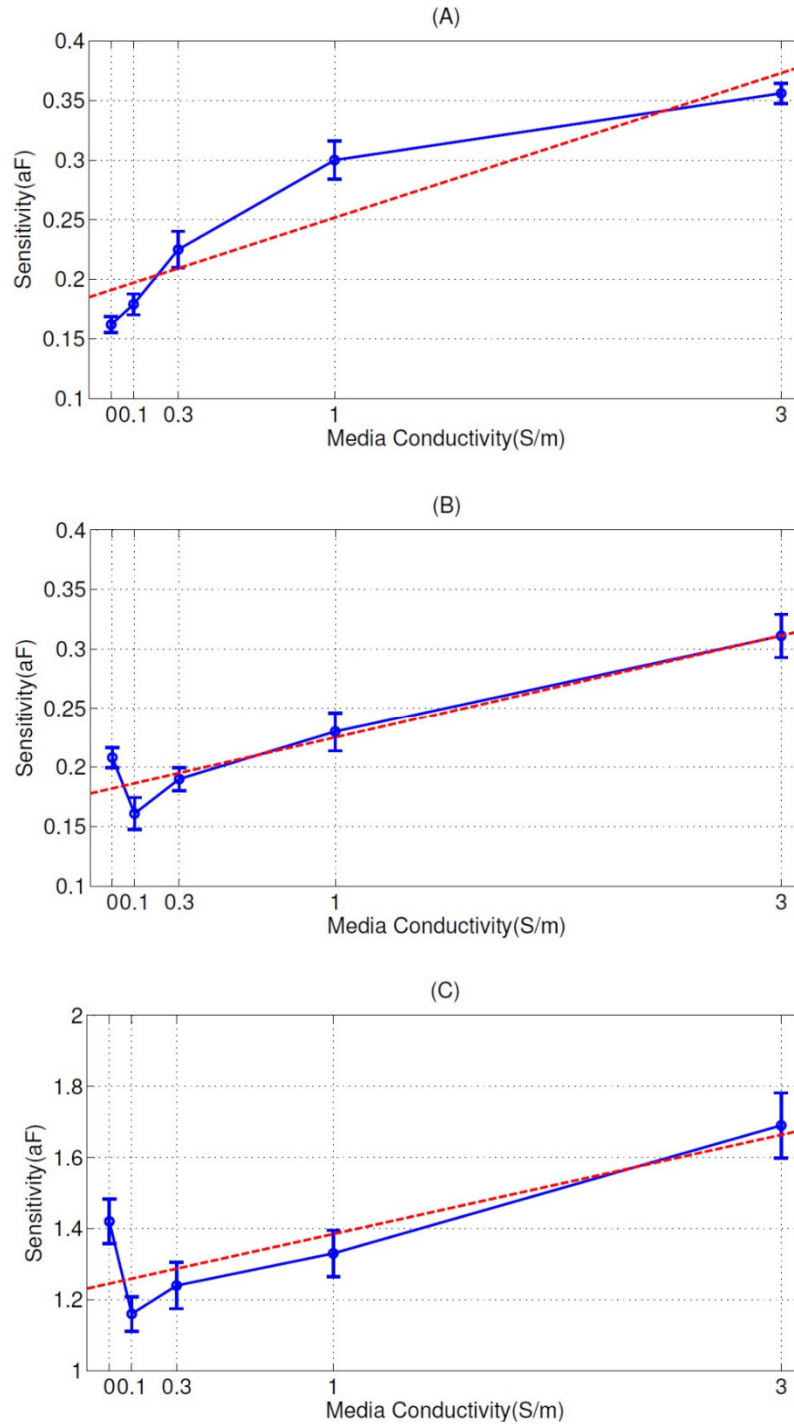


**Figure 2.8:** Sensitivity changes for different sensors versus changes in media conductivity for the reflectometer. (A) High-Q resonator. (B) Low-Q resonator. (C) Reflectometer.

make it difficult to find the correct resonance frequency. In the second step, the nulling is accomplished using the mechanical adjustment of the phase shifter. Mechanical phase shifters avoid the additional noise introduced due to voltage modulation of phase. This double stage tuning makes the adjustment a cumbersome process and requires using bulky mechanical components. The reflectometer sensor can be nulled using frequency adjustment alone, as its operation is only based on nulling the electrical path length difference between sensing path and reference path. With the use of frequency based nulling it can also be easily automated. Simple RF sources are available with part per million stabilities, and part per million tunability that would be suitable for this task.

## **2.5 Conclusion**

A simple microwave frequency reflectometer suitable for use with microfluidic detection system with single cell sensitivity is demonstrated. The sensor operation is based on an interferometric structure that compares changes in electrical path length between a sensing path and a reference path. The use of a reflectometer allows very simple nulling of the interferometer. In addition, the components can be fabricated in a highly integrated PCB. The reflectometer is much more compact than its resonator based counterparts. The reflectometer has been used for detection of 5.7  $\mu\text{m}$  beads and CHO cells. A key attribute of this sensor is that the sensing voltages are low (less than 300 mVp-p) and hence it does not cause parasitic dielectrophoretic actuation of the cells. Sensitivity up to 1.25 aF is obtained for particles flowing in DI water. This sensitivity is sufficient for applications such as use in DEP cytometer and does not significantly increase the uncertainty of DEP cytometer measurements. The sensor operation as a DEP cytometer was confirmed using 5.7  $\mu\text{m}$  beads. The change in sensitivity of the sensor over the media conductivity range of 0-3

S/m is less than that of resonator based sensors. This sensor will enable highly integrated and compact single cell sensors, including DEP cytometers.

In the next chapter the idea of a completely integratable capacitance sensor will be introduced. This is important because the developed microwave reflectometer makes use of a bulky lock-in amplifier and an RF generator. The new idea can be used for making a completely integratable DEP cytometer.

## **Chapter 3: Differential Ring Oscillator Based Capacitance Sensor for Microfluidic Applications**

### **3.1 Abstract**

A simple high frequency capacitance sensor with 180 aF sensitivity is designed for a wide range of microfluidic applications. The sensor is implemented utilizing differential ring oscillators operating at ~240 MHz with a differential signal at ~20 MHz. The sensor occupies ~2 cm×2 cm on a printed circuit board. The sensor is tuned using two precision variable capacitors and has a full scale range of ~1.5 pF. The sensor was able to detect less than 1% Isopropyl Alcohol in DI water and to detect 15  $\mu\text{m}$  polystyrene spheres flowing over 25  $\mu\text{m}$  lines and spaces coplanar electrodes in a microfluidic channel. The compact differential ring oscillator based architecture of the design makes it suitable to be integrated into microprocessor based systems for detection in Lab on Chip or Lab on Board applications.

### **3.2 Introduction**

Capacitive sensors are very useful in sensing applications. This type of sensors has been used for many years in different applications, and several techniques have been developed for high-resolution capacitance measurement. Applications range from integrated accelerometers for use in automotive applications and for structural health monitoring [48], to integrated implantable sensors for biomedical applications [49]. Capacitive sensors are known for signal stability, high sensitivity, lower power, and temperature immunity compared with resistive sensors [50], and they are well suited for remote sensing and biomedical applications. These sensors are aimed to detect permittivity rather than the conductivity of the materials between detection electrodes. Complexity of the methods and the architecture of capacitance detection systems varies depending on the design requirements and application, and has been reviewed in a previous work [25]. The

capacitance sensitivity of some designs has reached  $\sim 12$  zF [51].

In microfluidic sensors, these methods find use in Lab on Chip (LOC) applications [52-57], fluid and volatiles characterization [56], single biological cell detection and analysis [9], detection and characterization of microdroplets [58], etc. In these cases, sensors are preferred to operate above a few 10's kHz to avoid electrothermal, electrochemical and electrodes polarization effects [6, 30]. In addition, high detection voltages can damage biochemical samples and interfere with biological processes [30]. Therefore, capacitance sensors with MHz operating frequencies with relatively low operating voltages are advantageous. Capacitance sensors have also application in the detection of particles flowing in microfluidic channels [10]. In the case of mammalian cells in saline solutions MHz detection frequencies minimize the possibilities of electrothermal, electrochemical and electrode polarization effects. In addition, the use of frequencies in the 1-10 MHz frequency range can result in highly variable dielectrophoresis (DEP) force on cells and particles due to interfacial polarization [6]. Hence sensors with detection frequencies in the 100 MHz to GHz frequency have advantages [24] for use in capacitance sensors used in microfluidic applications to detect particles and cells. In addition, sensors in this frequency range are useful to detect particles and cells height changes induced by the applied MHz DEP signals. Clausius-Mossotti factor cross over frequencies for cell suspensions in low conductivity (less than 10 S/m) medium makes detection frequencies in the  $\sim 10$  kHz to 100 MHz range optimal to use for positive DEP (PDEP) cell characterization [59], and hence frequencies above 100 MHz are advantageous for detection [24]. For use in microfluidics applications sensors require sensitivity that is sub femto Farad, due to the small volume occupied by the samples in microfluidic channels. For example, a 25  $\mu\text{m}$  lines and spaces coplanar electrode in a 125  $\mu\text{m}$  channel filled with DI water has 52 fF capacitance between the electrodes [9]. For many applications there is also an interest in integration of these capacitance

sensors in highly compact systems [52, 60, 61].

LCR type meters are used for capacitance change detection in biochemical sensors [62], [63]. The operation frequency of these instruments is limited to a few tens of megahertz. To achieve higher operation frequencies, Network Analyzers can be used such as in [64] to extract complex permittivity information, and in [42] to de-embed capacitance changes from this information. In [9] lock-in amplifiers are used to limit the bandwidth, and to achieve high signal to noise ratios (SNR). All these instruments are expensive and bulky, and do not meet the need for compact capacitance sensors. There are capacitance detection sensors, integrated on chip, and commercially available to be used for detection such as AD7746 used in [65] and MS3110 used in [66]. These chips make use of a few 10's kHz detection signals, which makes their application limited in biomedical sensors. The same problem exists in [36] where using analog amplifiers limits the operation frequency to a few MHz, causing instability in detection at high frequencies.

In this work a simple differential ring oscillator based capacitance sensor is presented. The sensor detection frequency is about 240 MHz, which is useful for a wide range of biomedical and microfluidic applications. The design makes use of two separate ring oscillators with XOR gate and a low pass filter to detect the frequency difference. It is tuned using two precision variable capacitors. The design is implemented on a printed circuit board (PCB). The sensor architecture makes it small in size, low cost, and easily integratable. This design has been used for detection of isopropyl alcohol (IPA) content in a DI water solution, and the detection of 15  $\mu\text{m}$  Polystyrene spheres (PSS) flowing in a microfluidic channel.

### **3.3 Design Description**

The design schematic is shown in Fig. 3.1. A 3-stage ring oscillator is made by connecting the input to the output of an integrated 3-stage inverter (74AUP2G3404 NXP Semiconductors). The

propagation delay between these pins for a 5 pF load, ranges between 1.1 ns to 3.3 ns, resulting in a predicted oscillation frequency between 156 MHz to 454 MHz [67]. This oscillator oscillation frequency is above 100 MHz, which makes it suitable for sensing in microfluidic applications.

In this design, two of these oscillators are used in a differential architecture. One of the ring oscillators (ring oscillator1) is connected to the detection microelectrodes in a microfluidic channel. The coplanar microelectrodes in the channel are 25  $\mu\text{m}$  wide and have a distance of 50  $\mu\text{m}$  center to center. Details of the microfluidic chip fabrication are given in [45]. To remove any DC component from the output of ring oscillator1, a 47 pF decoupling capacitor is used before applying the signal to the microelectrodes. This is mainly to prevent channel microelectrodes deterioration over time due to electrolysis.

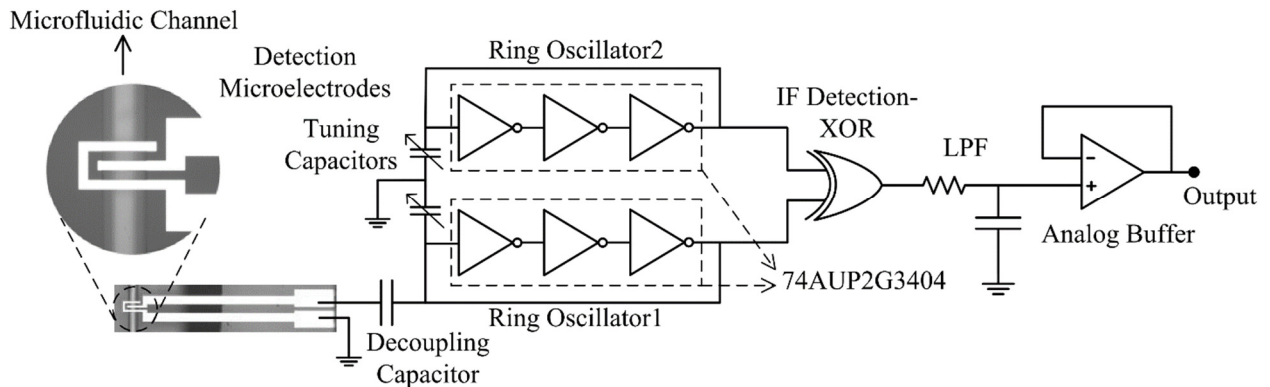


**Figure 3.1:** Design schematic composed of two ring oscillators used for detection of capacitance change in a microfluidic channel.

Oscillation frequency of the ring oscillators in this work primarily depends on the capacitance of the input/output node of the oscillator and the supply voltages. The use of a low noise power supply (Keithley 2400 SourceMeter) results in the oscillation frequency changes being primarily due to changes in the capacitance of microelectrodes. The wavelength of the applied signal from oscillator1 to microelectrodes is more than 1 order of magnitude greater than the electrical distance between oscillator and the detection microelectrodes. Hence, neglecting the parasitic resistance of

electrical connections, a lumped element approximation can be used. Changes in oscillation frequency due to noise are explained in section 3.5.

The oscillation frequency of ring oscillator1 is compared with the other oscillator (ring oscillator2) using an XOR gate (NC7SV86, Fairchild) for detection. The XOR gate produces a signal that has a fundamental frequency given by the ring oscillators that is pulse width modulated at the difference frequency. This signal is then passed through a low pass filter (10 k $\Omega$ , 4 pF) to remove the high frequency components. The output IF signal from the filter is buffered using an amplifier (LT1220), and then coupled into to a 12-digit Frequency Counter (53132A, Agilent) in order to determine the difference frequency.

To tune the sensor output IF (intermediate frequency) frequency two variable capacitors (ER-530-006, Sprague-Goodman) are used, each connected to one of the ring oscillators. These capacitors have about 24 full turns of tuning, and their capacitance is specified to range between 0.25 pF to 1.5 pF over the full range [68]. This results in an estimated  $\sim$ 53 fF of capacitance tuning per turn. In practice the variable capacitor connected to ring oscillator1 is adjusted to maximum (except when it is connected to the microelectrodes), and the variable capacitor of ring oscillator2 is set such that it oscillates 20 MHz above ring oscillator1. The output IF was typically adjusted to be about 20 MHz during the tests described in this work. This frequency offset between oscillators allows them to operate out of injection locking and injection pulling modes. To create a mechanically stable system with stable parasitic impedances the system was implemented on a printed circuit board (PCB). Two 0.15 mm diameter brass wires coupled the sensor to the microfluidic channel. The electrodes on the microfluidic device had a total capacitance of approximately 0.3 pF, and hence could be compensated for using the adjustable capacitor. A photograph of the sensor implemented on a 0.0602" FR4 printed circuit board (PCB), with other

system components are shown in Fig. 3.2.

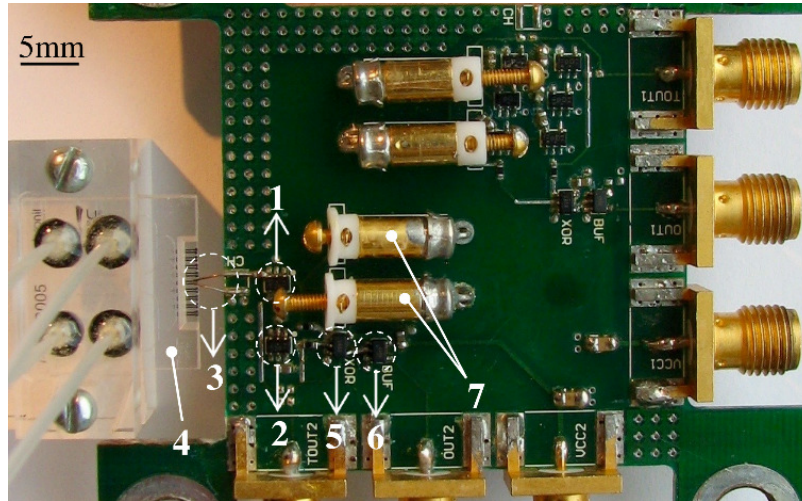


**Figure 3.2:** Differential ring oscillator based capacitive sensor in contact with microelectrodes of a microfluidic channel. Sensor components are: 1- ring oscillator1, 2- ring oscillator2, 3- brass wires, 4- microfluidic chip 5- XOR gate, 6- unity gain buffer, 7- variable capacitors. Dimension of the designed sensor on PCB is  $\sim 2\text{ cm} \times 2\text{ cm}$ .

According to Fig. 3.1, the capacitance of ring oscillator1 is changed when the capacitance of the connected microelectrode or variable capacitance changes. The capacitance of ring oscillator2 changes when the connected variable capacitance to that oscillator changes.

To couple the sensor to the channel microelectrodes the sensor is mounted on a xyz positioner. The xyz positioner is then used to position the sensor such that the brass wires contact the channel electrodes. The detection signal is then applied to the microelectrodes using the brass wires soldered to the output of ring oscillator1. The printed circuit board in contact with microfluidic chip are both kept at room temperature inside a vibration isolation chamber, to reduce the effect of mechanical noise and temperature variations from air currents. This is important as the water dielectric constant variation with temperature is  $4.5 \times 10^3 \text{ ppm}/^\circ\text{C}$ . This variation is about  $0.14 \text{ fF}/^\circ\text{C}$  when the variable capacitors are tuned for an output IF frequency of  $\sim 20 \text{ MHz}$ . When the sensor

is connected to the microelectrodes, the added capacitance causes the frequency difference to increase. This is compensated by using the adjustable capacitor coupled to ring oscillator1 until the difference frequency is approximately 20 MHz. The sensor is supplied with 3 V DC connected to the inverters, and XOR gate. The output IF signal is then sampled by the frequency counter at a rate of 10 Hz, and the frequency readings are transferred through serial port to Matlab each 200 ms for analysis.

### **3.4 Simulation and Characterization**

In this section the sensitivity of the capacitance sensor was estimated using simulation. These simulations were compared to results obtained using the tunable capacitors as precision test capacitors. The variable capacitors were calibrated at 1 MHz using a precision impedance analyzer (4294A, Agilent). Starting with the screw completely in, the screw was turned out in half turn steps (180° rotation). At each step 4 capacitance value readings from the impedance analyzer were collected from an average of 8 readings. This resulted in an uncertainty for each reading of less than 0.01 pF. The variable capacitor values are changed (and measured) by turning the capacitor screw each time half turn (1 step), equivalent to approximately 36 fF. This per turn difference is smaller towards the end of the range due to the non-linearity in capacitance changes as the tuning screw begins to exit the tunable capacitor.

The measured variable capacitor values in 45 half turn steps were then used as input to simulate the circuit, using MicroCap simulator. For the inverters an IBIS model (typical) was used with ring oscillator1 connected to a fixed 1.68 pF capacitor, while ring oscillator2 is connected to a variable capacitor equal to the 45 capacitance values measured using the impedance analyzer. To model the XOR gate input capacitance, a 2 pF capacitor was connected in the output of each oscillator [69] with a 150 fF coupling capacitor between the pins, which is measured by connecting input

“a” and “b” of the XOR to the impedance analyzer.

Simulation results are shown in Fig. 3.3. The oscillation frequency difference is expected to be 21.88 MHz when ring oscillator2 capacitance is 0.28 pF, and reduces to 0 MHz when both capacitors are maximized. For this type of capacitance sensor, an important figure of merit is rate of frequency change with respect to the capacitance. In the region used for this work, the slope is 17.5 kHz/fF, found from a linear fit to the first 25 data points on the left hand side.

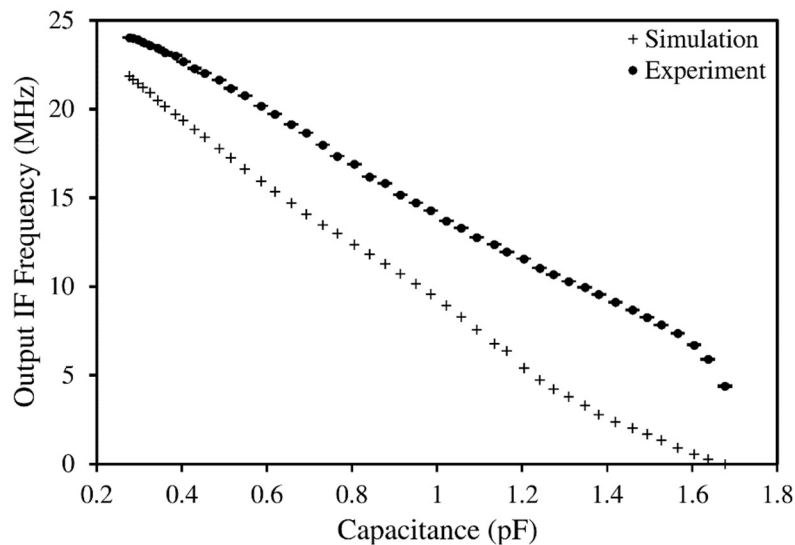


**Figure 3.3:** Capacitance sensitivity simulation vs. experimental measurements.  $\Delta f/\Delta C$  from simulation is 17.54 kHz/fF compared with 14.13 kHz/fF in experimental. Error bars are included for experimental results data points.

The sensor was characterized using the tuning capacitors. In the experiments, ring oscillator1 tuning capacitor is maximized, and ring oscillator2 variable capacitor was varied from 1.68 pF to 0.28 pF using one half turns until the adjusting screw was completely out. The frequency sensitivity to capacitance change, found from a linear fit to the first 25 data points. The slope was 14.1 kHz/fF. This is slightly smaller than the calculated slope from simulation results. However, it is well within the expected range given the expected variation in propagation delay. The oscillators output signals were measured using a high impedance probe (Model 35, GGB Industries

$C_P=0.04$  pF). The oscillation frequency range of ring oscillator1 was found to range between 240.9 MHz-264.8 MHz and ring oscillator2 found to range between 244.5 MHz-271.7 MHz. The initial oscillation frequency difference between oscillators causes the results from the experiment to have an offset when compared with the simulation results. Also the difference between simulation and experimental results at the end points maybe due to the overly simplified modeling of the XOR gate inputs with linear capacitive elements in the simulation. This results in greater error as the capacitance difference between oscillators become smaller. In addition, when the oscillator frequencies become close, the oscillators will pull each other due to the coupling of the oscillators through parasitic circuit elements. When the capacitive differences are small enough  $\sim 0.1$ - $0.2$  pF, the oscillators will lock to one another and capacitance shifts will result in phase shifts rather than frequency shifts [70].

To conclude, calibration of the sensor includes two steps. First step is measurement of the sensor frequency to capacitance sensitivity using variable capacitors. Based on 74AUP2G3404 datasheet [67], minimum propagation delay will increase from 1.1 ns to 1.6 ns when inverter output capacitance is increased from 5 pF to 10 pF, equivalent to a sensitivity of 28.4 kHz/fF. This number increases from 2.1 ns to 2.7 ns when typical values are used, equivalent to a sensitivity of 10.6 kHz/fF. Using max values for propagation delay, results in a sensitivity of 4.9 kHz/fF. So the frequency to capacitance sensitivity can vary by a factor of more than two about its typical value, and sensitivity measurement is necessary for each circuit. The second step is tuning output IF frequency out of the injection pulling/locking range around  $\sim 20$  MHz.

### 3.5 Description of System Noise

Minimum detectable capacitance (MDC) of the designed sensor can be defined by:

$$\text{MDC} = \frac{N}{S} \quad (3.1)$$

In which “N” is the frequency RMS noise, and “S” is the sensor frequency sensitivity to capacitance changes (Hz/F). So it is important to identify the dominant sources of noise. Frequency RMS noise in time domain from a single ring oscillator in this design can be calculated by [71]:

$$N = \frac{1}{T_W} \sqrt{N_{OSC}^2 + G_S^2 N_{VDD}^2} \quad (3.2)$$

In which  $T_W$  is the averaging window length,  $N_{OSC}$  is RMS frequency noise originated from oscillators,  $N_{VDD}$  is RMS supply voltage noise and  $G_S$  is the oscillator output frequency sensitivity to supply voltage (in Hz/V). Both  $N_{OSC}^2$  and  $N_{VDD}^2$  are directly proportional to the area under the phase noise spectrum of oscillators and supply voltage respectively [71]. In this equation the other sources of noise such as temperature changes and averaging window length variation is neglected. Temperature changes induces signal drifts due to air movements around large metallic body of the variable capacitors. Window length variation can be neglected as the noise from frequency counter is less than 1 ppm.

In Eq. (3.2), the noise from high precision supply is negligible compared with oscillators noise. This assumption was tested by substituting the power supply with a heavily filtered battery source. This substitution did not change the noise level.

Due to the differential sensor architecture, the common correlated sources of noise is suppressed in the output IF, but the uncorrelated sources of noise and the noise from non-stationary processes ( $1/f$  noise) directly add in the output. To characterize the noise behavior, phase noise measurements were done using a phase noise measurement tool (E4448A PSA, Agilent). The high impedance probe is used to probe the output of ring oscillator2 operating at ~260 MHz, and the 20 MHz output IF from the buffer. The results are shown in Fig 3.4.

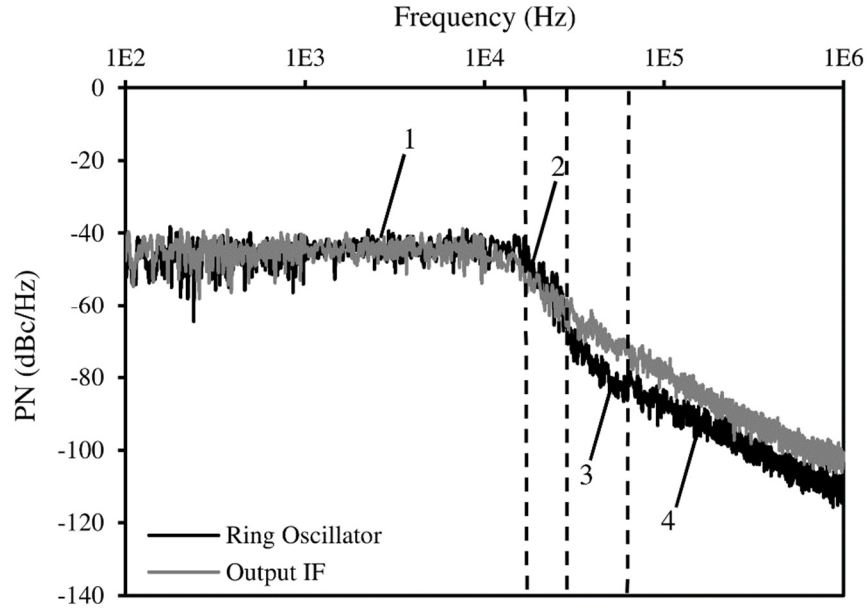


**Figure 3.4:** Phase noise spectrum of ring oscillator2 operating at 260 MHz, and the output IF at 20 MHz. Frequency regions are separated based on their dominant source of noise. 1- White noise injected around carrier, 2- random walk noise, 3- flicker noise, 4- thermal noise.

In this figure, phase noise spectrum of the ring oscillator is separated to different regions based on the dominant source of noise in that region. In region 1 close to the carrier, the noise is dominated by the injection of the white sources of noise at carrier frequency. Region 2 (16 kHz-27 kHz) is where the spectrum has  $1/f^4$  behavior, and the noise is dominated by the random walk noise up conversion [71]. Region 3 (27 kHz-62 kHz) is the  $1/f^3$  region created by the up conversion of the  $1/f$  noise from supply voltage and oscillators transistors at carrier frequency [72, 73].  $1/f^2$  region resides from 62 kHz to 1 MHz in the measurement frequency span, which is the created by the up conversion of white noises sources of noise at multiplicands of oscillation frequency [72]. Based on this  $f_{1/f^4} \approx 27$  kHz,  $f_{1/f^3} \approx 62$  kHz.

Increasing  $T_w$  to infinity does not necessarily reduce noise down to zero. It is shown that [73, 74] flicker noise dominates at large averaging time frames as jitter accumulates by a factor of  $\zeta T_w$ , in which “ $\zeta$ ” is the oscillator flicker noise multiplicand. Reducing the averaging time  $T_w$  below  $(\kappa/\zeta)^2$

causes white noise dominates and jitter increases linearly with a reduction in bandwidth ( $\kappa$  is the oscillator white noise multiplicand) [74]. Minimum noise floor is hence limited by  $\sqrt{2}\times\zeta$  from two identical oscillators with uncorrelated  $1/f$  source [71]. This can be achieved by selecting  $T_w$  between  $1/f_{1/f}^3$  and  $1/f_{1/f}^4$  where the noise is dominated by  $1/f$  sources [71]. In our case this translates to  $T_w$  between  $16\ \mu\text{s}$ - $37\ \mu\text{s}$ .

In this work, the averaging time frame of the frequency counter is limited to 1 ms. So RMS noise is measured in 3 different cases of 1 ms, 10 ms and 100 ms. The results are shown in Table 3.1. Based on this 100 ms averaging time is selected for the measurements done in this work. It should be noted that the noise does not increase by the same rate of reduction in  $T_w$ . The reason is because in this averaging periods, the noise is not dominated by white noise sources. A direct implication if this is that sensor bandwidth can be increases by a factor of 100 (for faster measurements) with a MDC reduction of less than two.

**Table 3.1:** RMS frequency noise in time domain vs. averaging time

Averaging time	100 ms	10 ms	1 ms
RMS frequency noise	3.5 kHz	4.8 kHz	6 kHz

### 3.6 Results and Discussion

#### 3.6.1 Detection of DI Water Alcohol Content

This sensor has several potential uses. One use would be to detect bulk changes to the dielectric material filling the channel, for applications such as chromatography. This application of the sensor is demonstrated through the detection of DI water with varying Isopropyl alcohol (IPA) content. The reason is because water and IPA dielectric constants are known in a wide range of frequencies. IPA has a lower polarizability than DI water. Therefore, as IPA content is increased the bulk relative dielectric response decreases. For this purpose, 6 separate 20ml samples of DI water with 1%, 5%, 10%, 25%, 50% IPA contents and one with 100% IPA content is prepared.

Pressure driven flow is used to rapidly alternate the flow over the electrodes between DI water and the DI/IPA mixture. Two 2 ml vials are used, one filled with DI water connected to port1 of the microfluidic chip as in Fig. 3.5, and the other filled with DI/IPA mixture connected to port4 of it. The headspace of the vials is pressurized with 7 PSI filtered air. Tubes extending into the liquid in the vials is coupled to the ports on the microfluidic chip (See Fig. 3.5). To control the flow of each fluid within the channel, valves are connected to tubes coupled to port2 and port3 of the microfluidic chip. By closing the valve on port2 and leaving the valve on port 3 open the fluid from port 1 is forced across the electrodes. By closing the valve on port3 and leaving the valve on port 2 open the fluid from port 4 is forced across the electrodes. This system allows the rapid and repetitive replacement of the DI water with “x” percent IPA content. The permittivity of the mixture can be estimated based on water [75] and IPA permittivity [76] at room temperature using:

$$\epsilon_{\text{mixture}} = \left(\frac{x}{100}\right) \times 18.6 + \left(\frac{100-x}{100}\right) \times 80.1 = -0.615x + 80.1 \quad (3.3)$$

The change in ring oscillator1 frequency is due to the DI water being replaced with DI water-IPA modifying the capacitance of microelectrodes within the channel. The channel electrodes capacitance is about 104 fF for the present microelectrode geometry when the channel is filled with water [9]. The change in the channel microelectrodes capacitance when DI water is replaced by DI water with “x” percent IPA content can be found approximately by:

$$\Delta C = \frac{\Delta\epsilon}{\epsilon} C_{\text{Microelectrodes}} = \frac{0.615x}{80.1} \times 104 \text{ fF} = 0.798x \text{ fF} \quad (3.4)$$

The expected change in capacitance based on Eq. (3.4), and the expected change in frequency based on the experimentally detected 14.1 kHz/fF sensor sensitivity is listed in Table 3.2.

$$\Delta f = 11.26x \text{ kHz} \quad (3.5)$$

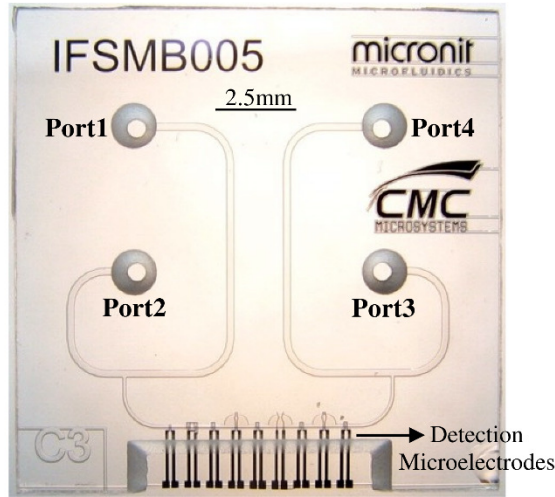


**Figure 3.5:** 4-port microfluidic chip used for detection of water-alcohol content and 15 $\mu$ m PSS.

**Table 3.2:** Capacitance and frequency change for different IPA content.

	$\Delta C$ (Calculation) (fF)	$\Delta f$ (Calculation) (kHz)	$\Delta f$ (Experiment) (kHz)
100%	79.8	1128.3	904.9 $\pm$ 6.10
50%	39.9	564.1	456.1 $\pm$ 2.63
25%	19.9	282.1	215.9 $\pm$ 3.62
10%	7.9	112.8	91.4 $\pm$ 2.88
5%	4.0	56.4	48.9 $\pm$ 3.65
1%	0.8	11.3	11.3 $\pm$ 2.08

In experimental measurements, DI water from the vial connected to port1 is replaced by mixture in the other vial connected to port4 repetitively 10 times, and the related frequency steps are recorded in Matlab. The average values and standard deviation of the frequency steps are shown in Table 3.2. Fig. 3.6 shows these steps when DI water is replaced with the DI water-IPA contents of 5% and 1%. The detected RMS noise in this case is found 2.4 kHz proportional to 178 aF based on sensor detection sensitivity. The experimental results of IF frequency shifts for different IPA contents are shown in Fig. 3.7 with the related error bars.

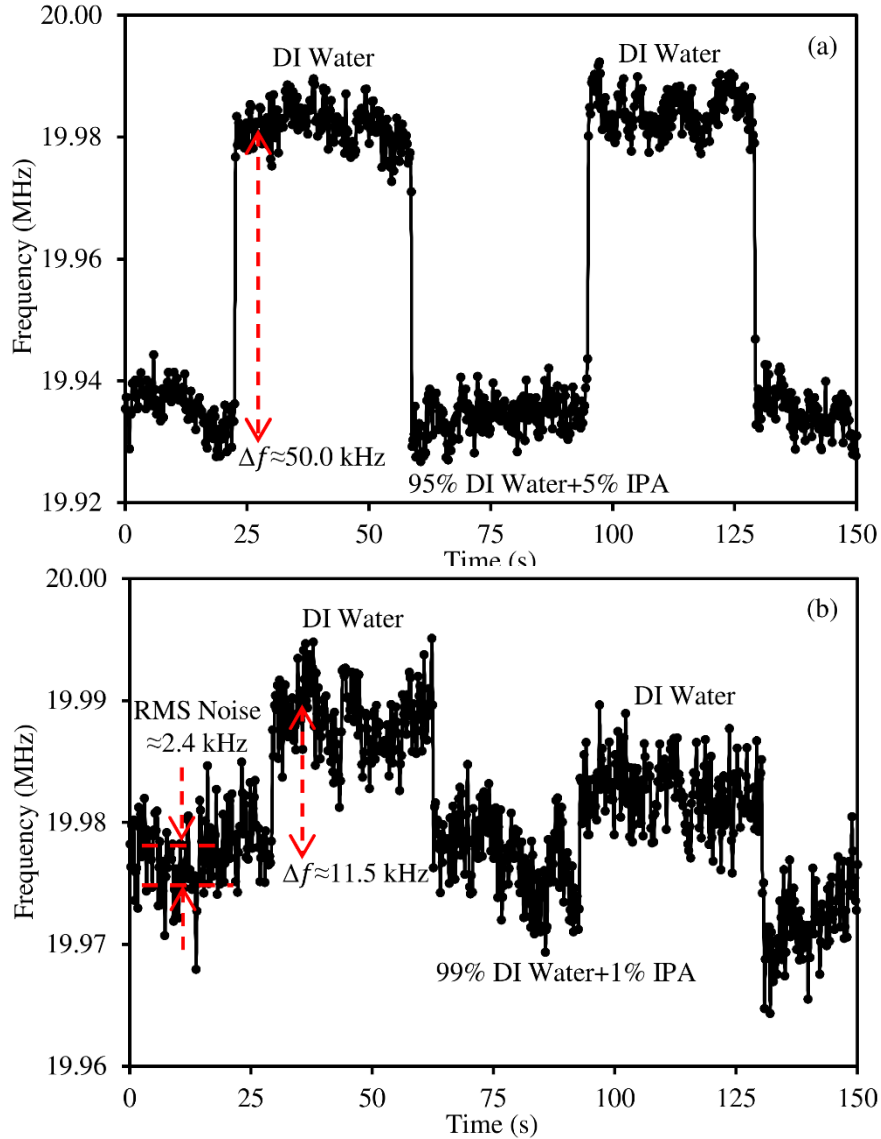


**Figure 3.6:** Detection of DI water with IPA content with sensor (scales are different on figures). (a) Shift in the output IF frequency, when DI water in channel is replaced by 5% IPA in DI water, is about 50 kHz. (b) Shift in the output IF frequency, when DI water in channel is replaced by 1% IPA in DI water, is about 11.5 kHz. RMS noise is about 2.4 kHz.

According to Fig. 3.7, the sensor shows an almost linear behavior between the frequency shifts and IPA content percentage from 1% to 100%. The difference between calculated frequency shifts and experimental results can be attributed to IPA contents percentage errors, temperature variations of permittivity, non-linearity of  $\Delta f$ - $\Delta C$  curves, and inaccuracy in microelectrodes

capacitance value in Eq. (3.4).

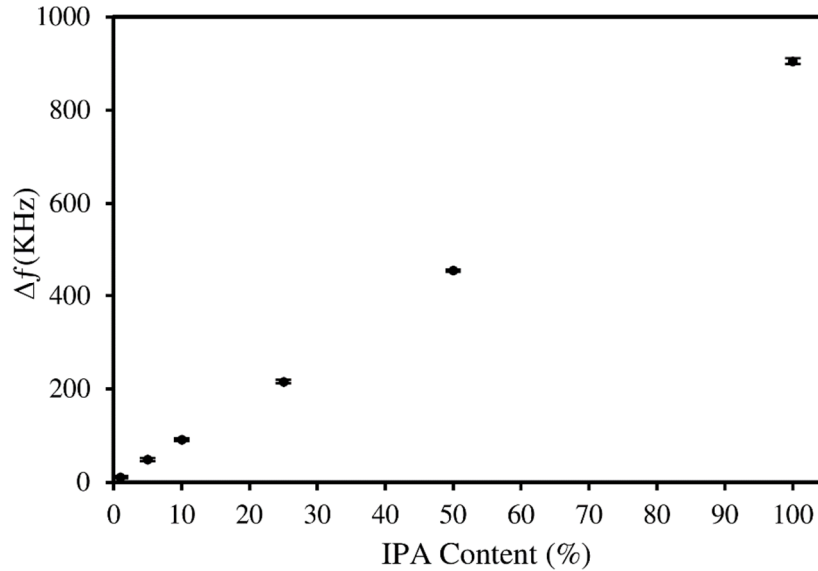


**Figure 3.7:** Shift in the sensor output IF frequency when DI water in the microfluidic channel is replaced by DI water with 1%, 5%, 10%, 25%, 50% and 100% IPA content. Error bars are included on figure. Measured frequency shifts trend line is  $\Delta f = 9.04 \times \text{IPA Content (\%)} + 0.25 \text{ kHz}$

### 3.6.2 Detection of flowing Poly-Styrene Spheres (PSS)

A second possible application of this sensor is for the detection of flowing particles. When a particle displaces water in the vicinity of the electrodes, it causes change in the capacitance of the electrodes. This capacitance change is known for microbeads and depends on their size, height in the channel, permittivity and detection microelectrodes size [10]. Microbeads can be used for calibration of the sensor. Also in electrical analysis of spherical biomaterials such as single cells, output signal can be compared with the signal from a microbead to find the biomaterial permittivity. In this demonstration, the sensor is used to detect 15  $\mu\text{m}$  diameter PSS signatures. Occasionally, PSS beads will bind to one another forming clusters of 2, 3 or 4 beads. In this example clusters were used to verify the linearity of the sensor response to cluster volume. In this case DI water is used as the fluid carrying beads inside the microfluidic channel over the microelectrodes in contact with sensor brass wires. For this measurement, the vials connected to

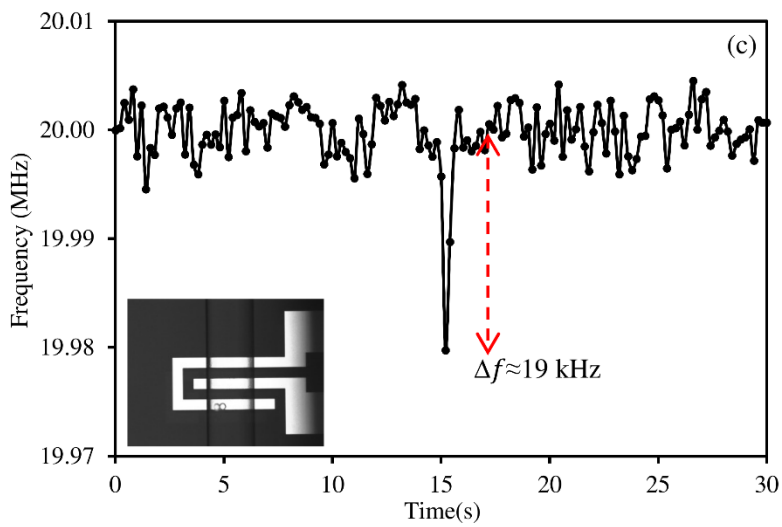
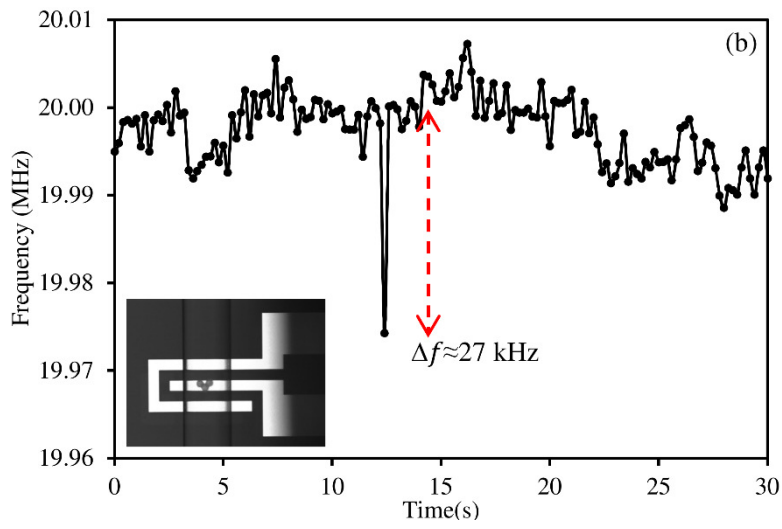
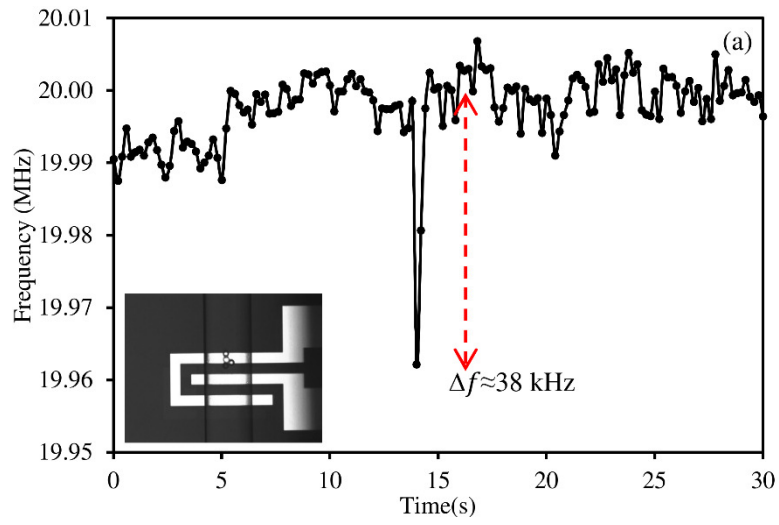
port1 and port2 are filled with DI water/PSS mixture, and DI water respectively. The valves connected to port2 and port3 are then left open to let the DI/PSS mixture flow to the channel by the pressure from vials height difference. Using a height difference of 1-5 cm this pressure is set between 1-5 mbar to drive PSS at a velocity of less than 100  $\mu\text{m/s}$ . In this case particles will be flowing almost at the bottom of the channel close to the detection microelectrodes.

Sample signatures of the recorded data for one bead as well as two, three and four 15  $\mu\text{m}$  beads cluster are shown in Fig. 3.8. Simulations of particles flowing over electrodes of the geometry used predict the expected capacitance changes, for a 6  $\mu\text{m}$  diameter PSS to be  $48 \pm 4$  aF when driven at height of  $7 \pm 1$   $\mu\text{m}$  (center to bottom) [39]. The capacitance scales with particle volume, and the expected capacitance change of a single 15  $\mu\text{m}$  bead is approximately  $750 \pm 60$  aF yielding an expected frequency shift of  $10.6 \pm 0.9$  kHz.

This change should scale with the number of beads in the cluster and shows that the theoretical values are closed to experimental results in this case. Details of the number of signatures collected and the average and standard deviation of signatures peak values are shown in Table 3.3.

**Table 3.3:** Number of 15  $\mu\text{m}$  beads signatures collected with the average and standard deviation of their peak values.

	1 Bead	2 Beads cluster	3 Beads cluster	4 Beads cluster
Number of signatures collected	6	5	3	5
Signatures average peak value	11.8 kHz	18.8 kHz	26.5 kHz	38.2 kHz
Peak values standard deviation	1.3 kHz	1.1 kHz	0.8 kHz	4.2 kHz



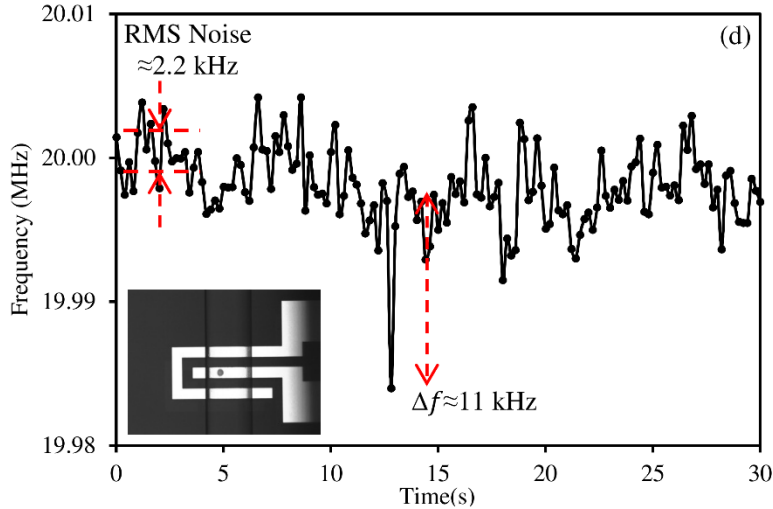


**Figure 3.8:** Sample signatures of single and multiple 15  $\mu\text{m}$  PSS detected by the sensor. (a) Four 15  $\mu\text{m}$  beads cluster passing over the microelectrodes causes a frequency shift of about 38 kHz. (b) Three 15  $\mu\text{m}$  beads cluster passing over the microelectrodes causes a frequency shift of about 27 kHz. (c) Two 15  $\mu\text{m}$  beads cluster passing over the microelectrodes causes a frequency shift of about 19 kHz. (d) A single 15  $\mu\text{m}$  bead passing over the microelectrodes causes a frequency shift of about 11 kHz. RMS noise is about 2.2 kHz.

### 3.7 Conclusion

A simple low cost high frequency capacitance sensor is designed and implemented on a PCB to be used for microfluidic applications. The sensor is composed of two ring oscillators connected to sensing microelectrodes where their frequency difference is detected with an XOR gate and monitored in a frequency counter. The use of multiturn trimmer capacitors connected to oscillators makes sensor tuning to within 10 fF relatively easy. Sensor frequency sensitivity to changes in capacitance simulation results are shown to be close to experimental measurements. The sensor has been used for detection of DI water alcohol content and 15  $\mu\text{m}$  diameter PSS. The sensor sensitivity is shown to be sufficient for detection of DI water IPA contents up to 1% and single 15  $\mu\text{m}$  PSS. The components are very low cost and the design components including the sensor and

counter can be easily integrated on a chip for capacitance detection, to be used in Lab-on-Chip applications.

The implemented sensor on PCB proves the idea of being able to use the ring oscillator based architecture for detection of the capacitance changes that suit biomedical applications. The use of available SMD components in this design limits the sensitivity to 180 aF, which is not enough for single cell applications. So in the next chapter the design of an application specific ring oscillator based capacitance sensor is introduced which is optimized to meet most of the requirements of a single cell DEP cytometer.

## **Chapter 4: GHz Frequency CMOS DEP Cytometer for Characterization of Single Biological Cells**

### **4.1 Abstract**

Differential 3-stage and 5-stage, ring oscillator based capacitance sensors were designed and integrated using 0.35  $\mu\text{m}$  CMOS technology. The sensor operates at 0.7 GHz and 1.4 GHz and achieves  $\sim 14$  aF capacitive sensitivity. The use of CMOS technology makes the integration of the sensing circuit, and the detection microelectrodes on chip possible. A hybrid system was developed where a Plexiglas microfluidic system was mounted on top of the CMOS chip. This created a complete Lab-on-Chip cytometer sensor that was used to detect individual polystyrene spheres (10-15  $\mu\text{m}$ ) and Chinese hamster ovary (CHO) cells. The integration of sensing circuitry with the microfluidic parts reduces the sensor size and weight significantly when compared with previous designs.

### **4.2 Introduction**

Integrated electronic sensors can replace bulky single cell analysis tools with small, low cost lab-on chip systems. Satisfying all of the design requirements in a single chip to be useful for single cell analysis can be challenging. These constraints are reviewed in [28] and include  $\sim$ GHz operation frequency,  $\sim 100$ 's mV detection voltage on microelectrodes,  $\sim$ cell size microelectrode dimensions, biocompatibility of the microelectrode material, and  $\sim$ aF capacitive sensitivity. In this work the implementation of a capacitance cytometer using a 0.35  $\mu\text{m}$  CMOS technology is demonstrated. These capacitance sensors have a potential application in DEP cytometers for monitoring biological single cells apoptosis process [24]. Monitoring apoptosis is important in determining the viability of cells cultures in the production of biopharmaceuticals and in tracking the effectiveness of chemotherapy treatments.

In the past work, a microwave frequency resonator based interferometer was designed and used as a DEP cytometer for monitoring Chinese Hamster Ovary (CHO) cells apoptosis [9, 10]. The resonator based sensor achieved  $\sim 0.65$  aF sensitivity at 1.4 GHz with less than 300 mVp-p detection voltage. However, this sensor was bulky because it used a lock-in detection technique and discrete connectorized components. Recently, a microwave frequency reflectometer was designed and implemented on a printed circuit board (PCB) which achieves  $\sim 1.25$  aF sensitivity at 1.8 GHz with less than 150 mV p-p detection voltage [25]. The reflectometer demonstrated a DEP cytometer, however still required the use of a bulky lock-in amplifier and an RF generator. Also, both of the previous designs have made use of a separate microfluidic chip in contact with the sensors which was used for driving cells over detection microelectrodes in the microfluidic channels.

In this work an integrated capacitance sensor was designed that implemented a standard CMOS technology. This reduced the sensor size and weight by more than three orders of magnitude. Calibrated 10  $\mu\text{m}$  and 15  $\mu\text{m}$  polystyrene sphere particles were flowed over coplanar microelectrodes on top of the chip for sensitivity measurement. These particles were driven at a very low velocity to maintain their position in the channel to remain close to the detection microelectrodes. This capacitance cytometer sensor was found to have enough sensitivity to be used to detect single biological CHO cells.

### **4.3 Design**

The sensor design is based on detection of capacitance changes induced by a cell during apoptosis in a differential architecture as shown in Fig. 4.1. Two identical ring oscillator generate  $\sim$ GHz frequency signals to be applied to the coplanar detection microelectrodes. The oscillation frequency of the oscillators changes linearly with capacitance for small capacitive perturbations. In presence of a cell, the frequency of one oscillator changes relative to the other which is then detected with

an XOR gate. The output from XOR is then low pass filtered to remove the high frequency components of the signal. To detect the frequency difference between oscillators, this signal is then applied to an off chip frequency counter and monitored using MATLAB.

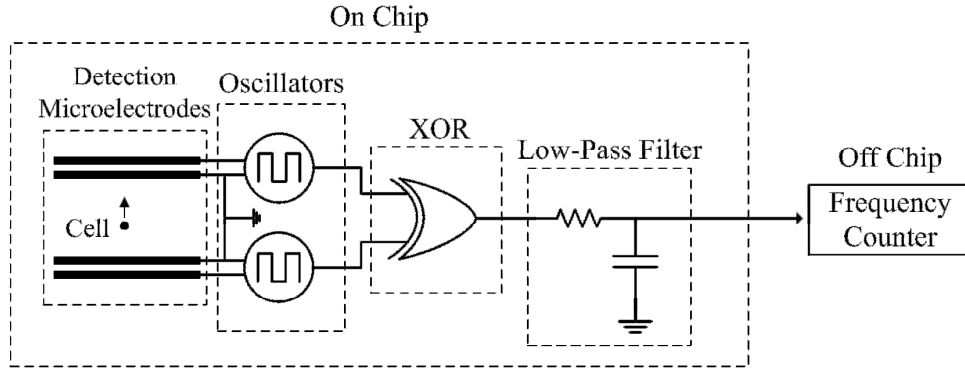


**Figure 4.1:** Ring oscillator based capacitance sensor design architecture.

#### 4.4 Design Optimization for Single Cell Application

For single cell permittivity measurements at GHz frequencies, lower detection voltages are desirable. An unwanted dielectrophoretic force occurs at higher voltages which causes the cells in the microfluidic channels to alter their position [26]. In case of using CMOS sensors, it is also desirable to minimize process costs which scales with process resolution. Schematic simulation (using Cadence software) of a 3-stage ring oscillator using the 0.35  $\mu\text{m}$  TSMC CMOS technology, resulted in a  $\sim 3.1$  GHz oscillation frequency. As in a typical ring oscillators, the inverters oscillate between the voltage rails, a tapered ring oscillator structure was used to optimize the sensor for this particular application. This structure will help in maximizing oscillation frequency, as well as the capacitance sensitivity while maintains a minimal voltage on detection microelectrodes.

To maximize frequency in a tapered ring oscillator, number of stages need to be minimized. So 3-stage and 5-stage oscillators were designed (see figures 4.2(a) and (b)) to have maximum frequency that could drive a 2 pF capacitive load. This load value was obtained from previous capacitance

sensors connected to external microfluidic devices<sup>2</sup> [9]. In a tapered ring oscillator with an “ $\alpha$ ” scaling factor, a minimum propagation delay can be achieved when

$$C_{\text{load}} = \alpha^{N+1}C_g \quad (4.1)$$

and

$$\alpha \ln(\alpha - 1) = \frac{C_d}{C_g} \quad (4.2)$$

where  $N$  is the number of stages,  $C_{\text{load}}$  is the load capacitance at the last stage,  $C_g$  is the input capacitance of the first stage, and  $C_d$  is the output capacitance of the first stage [77]. Extraction of a minimally sized, symmetric inverter, with  $(W/L)_n=2.4 \mu\text{m}/0.35 \mu\text{m}$  and  $(W/L)_p=3.8 \mu\text{m}/0.35 \mu\text{m}$  resulted in  $C_g \approx 2.4 \text{ fF}$  and  $C_d \approx 0.6 \text{ fF}$ . Using these inverter cells results in a scaling factor of  $\alpha \approx 3$  since  $C_d \ll C_g$ . For  $N=3$ ,  $C_g \approx 25 \text{ fF}$ , proportional to 12 unit cells on the first stage and consequently 36 and 108 unit inverters for the next two stages. For  $N=5$ ,  $C_g \approx 2.7 \text{ fF}$  proportional to a single unit cell on the first stage and consequently 3, 9, 27 and 81 unit inverters for the next four stages.

In this design, differential microelectrodes with same spacing dimensions as in [24] but with a length of  $400 \mu\text{m}$  are used. The extraction of the parasitic capacitance of such microelectrodes in  $0.35 \mu\text{m}$  TSMC CMOS technology was found to be  $\sim 200 \text{ fF}$ . This number can increase by a factor of 2 when the channel was placed over the microelectrodes and filled with water instead of air. So in the schematic circuit simulations a capacitance of  $500 \text{ fF}$  was used as the microelectrode

---

<sup>2</sup>  $2 \text{ pF}$  load was selected as an initial estimate for the worst case scenario, to be able to use oscillators in different detection architectures. For example, rather than using an XOR gate to detect frequency difference between oscillators, oscillators output can directly drive input capacitances of on chip counters. Also the oscillators can be used for detection when in contact with external microfluidic chips, rather than on chip microelectrodes in this work. These microelectrodes are estimated to have  $\sim 500 \text{ fF}$  capacitance, and hence are not connected to the last stage of the oscillator, but are moved between different stages such that the sensor can have the highest possible sensitivities. The output stages in this work only drive  $6 \text{ fF}$ , and  $6.7 \text{ fF}$  capacitances which are the capacitance of the input ports of the XOR gate. These capacitances are too small compared with loading ability of the oscillators, and hence does not change oscillators frequency based on measured sensitivities in Table 4.4.

parasitic capacitance which represents the load connected to the output of one of the stages in the tapered structure.

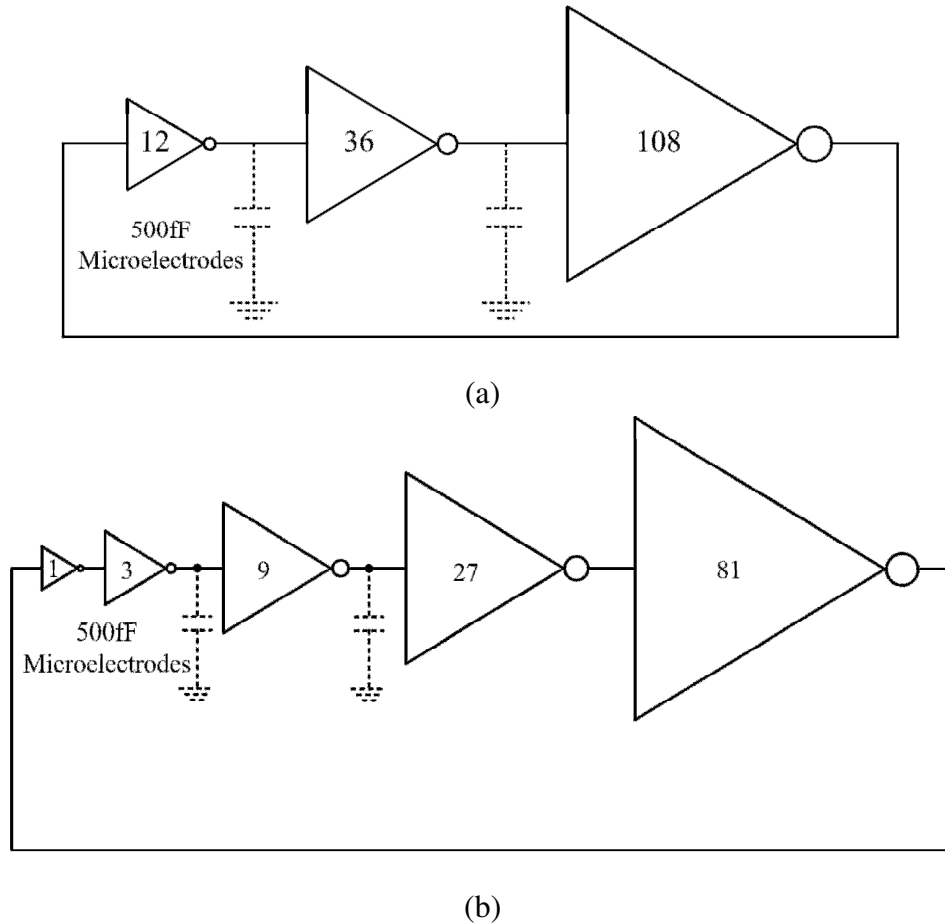


**Figure 4.2:** (a) 3-stage ring oscillator. (b) 5-stage ring oscillator.

In theory, connecting this capacitance to the output of the last stage in each of the 3-stage and 5-stage oscillator results in minimum sensitivity, and connecting them to the first stage should result in significant drop in frequency due to minimum loading capability of those stages. So such capacitance is moved between different stages of the oscillators to find the best stage to connect it to, in terms of operation frequency and sensitivity. The changes in sensitivity and operation frequency are shown in Table. 4.1 with a 500 fF microelectrode load is connected to the first and second stages of the 3-stage oscillator and the second and third stages of the 5-stage oscillator.

Based on these schematic simulation results, the microelectrodes in the 3-stage ring oscillator were connected to the output of the first stage, and in the 5-stage oscillator to the output of the second stage. This achieved the highest possible sensitivity with ~GHz operation frequency.

The chip layout is shown in Fig. 4.3. Pin and component descriptions of the following sensor are discussed in Table 4.2.

**Table 4.1:** Oscillation frequency and sensitivity changes by connecting microelectrodes to different stages.

	Simulated		Measured
<b>3-Stage Oscillator</b>	Stage 1	Stage 2	Stage 1
Oscillation Frequency	1.84 GHz	2.26 GHz	1.37 GHz
Sensitivity	0.65 MHz/fF	0.1 MHz/fF	0.57 MHz/fF

	Simulated		Measured
<b>5-Stage Oscillator</b>	Stage 2	Stage 3	Stage 2
Oscillation Frequency	0.7 GHz	0.9 GHz	0.51 GHz
Sensitivity	0.37 MHz/fF	0.32 MHz/fF	0.134 MHz/fF

As shown, the 3-stage and 5-stage differential ring oscillator based sensors were implemented on the same die. The pair of microelectrodes connected to each of these sensors were aligned at the same horizontal coordinate which facilitated the use of the same microfluidic channel. For this purpose, the chip pins were only placed on the left and right hand sides of the chip. The top and bottom were left open for mounting a microfluidic part on top of the chip. The microfluidic section was made by machining a 350  $\mu\text{m}$  width and 100  $\mu\text{m}$  height microfluidic channel which was clamped on top of the chip. The microelectrodes were implemented using the top metal level (M4) in the process. These microelectrodes are 400  $\mu\text{m}$  in length and are used to sense the changes in capacitance when a cell passes over the differential coplanar microelectrodes of each sensor.

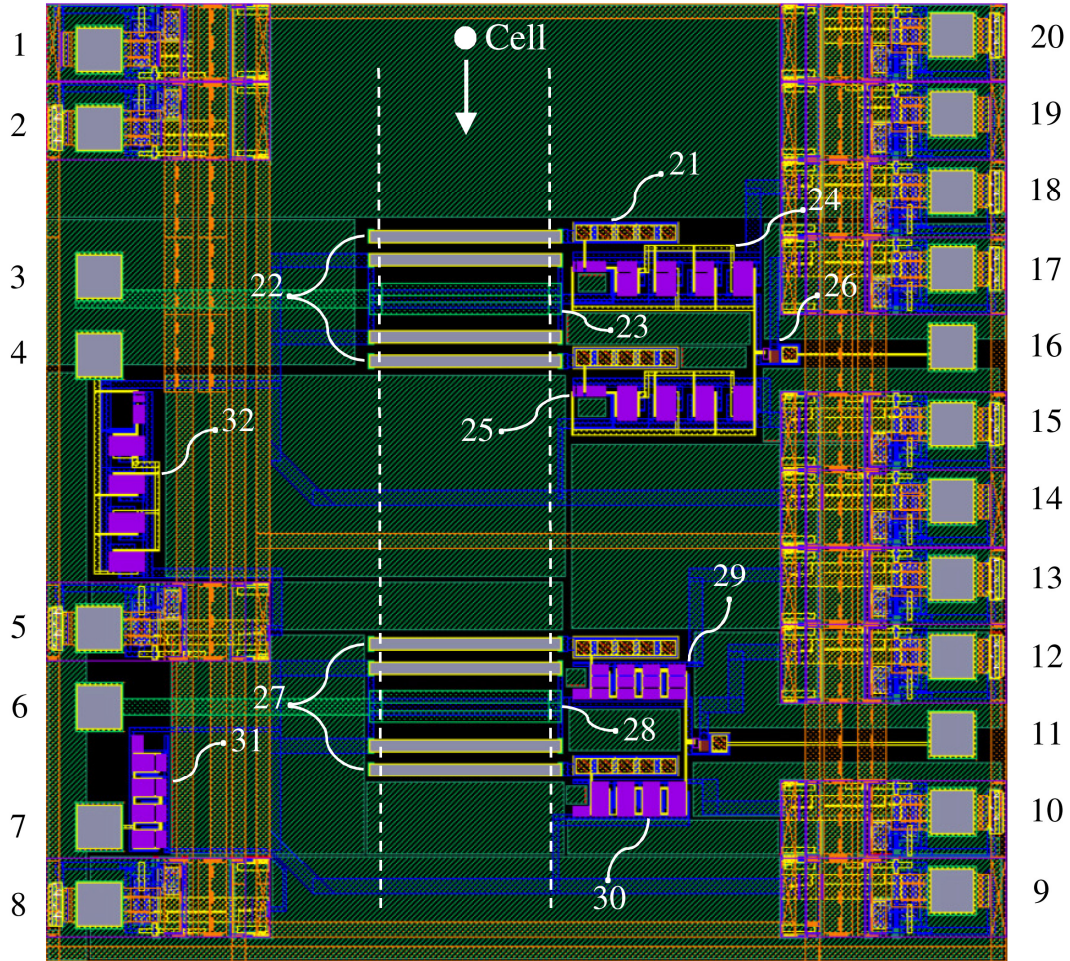


**Figure 4.3:** Chip layout in Cadence. It is designed to be 2 mm×2 mm in dimension. Pin configuration and component descriptions are discussed in Table 4.2.

In theory when the oscillators are powered using the same supply voltage, they should operate at the same frequency. Due to the injection locking of one oscillator in each pair to the other because of microelectrodes coupling capacitance, oscillators operate at almost the same frequency unless they are tuned far enough in frequency to operate unlocked. Based on experimental measurements in this work, a 20 MHz frequency difference is required for the oscillators to operate in an almost linear unlocked frequency range.

**Table 4.2:** Chip Layout Pin and Components Description of Fig. 4.3.

Pin/Component Number	Description
1	VDD ring pad for protection
2	VSS ring pad for protection
3	DEP signal pad for 5-stage sensor
4	5-stage test ring oscillator output
5	5-stage test ring oscillator VDD pad
6	DEP signal pad for 3-stage sensor
7	3-stage test ring oscillator output
8	3-stage test ring oscillator VDD pad
9	GND pad for 3-stage sensor
10	VDD pad for 3-stage ring oscillator1
11	3-stage sensor output pad
12	VDD pad for 3-stage sensor XOR gate
13	VDD pad for 3-stage ring oscillator2
14	GND pad for 5-stage sensor
15	VDD pad for 5-stage ring oscillator1
16	5-stage sensor output pad
17	VDD pad for 5-stage sensor XOR gate
18	VDD pad for 5-stage ring oscillator2
19	VSS ring pad for protection
20	VDD ring pad for protection
21	5pF decoupling capacitor between 5-stage ring oscillator2 and its sensing microelectrode. The same capacitor exists between other oscillators and their associated sensing microelectrodes.
22	Sensing microelectrodes of 5-stage sensor
23	DEP microelectrode of 5-stage sensor
24	5-stage ring oscillator2
25	5-stage ring oscillator1
26	XOR gate and filter of 5-stage sensor. The same block exists in 3-stage sensor.
27	Sensing microelectrodes of 3-stage sensor
28	DEP microelectrode of 3-stage sensor
29	3-stage ring oscillator2
30	3-stage ring oscillator1
31	3-stage test ring oscillator
32	5-stage test ring oscillator

To be able to achieve this, separate supply pins were implemented for each oscillator in a pair to be able to tune them at the desired frequency difference. To measure the oscillation frequency, separate test ring oscillators were implemented vertically on the left side of the chip. The output from these tapered oscillators were directly connected to an output pad and probed with a high impedance probe (GGB, Model35). This resulted in 0.715 GHz and 1.46 GHz oscillation frequencies at a 3 V supply for 5-stage and 3-stage oscillators respectively<sup>3</sup>. As the chip is being used for detection of biomaterials, 5 pF DC decoupling capacitors were used between detection microelectrodes and oscillators to avoid deterioration of Al detection microelectrodes [30].

#### 4.5 Sensitivity Measurement

To measure capacitance sensitivity of the 3-stage and 5-stage differential ring oscillator based sensors, 15 μm and 10 μm diameter polystyrene spheres in DI water were driven over the detection microelectrodes. In this case the sensor supply voltage was 3 V. To supply the sensors a 16 bit DAC was used (LTC2607, Linear Technology) with 15 μV p-p noise from 0.1-10 Hz. This makes the dominant source of noise in the system the thermal and flicker noise from the sensor itself. This was confirmed by measuring the sensor RMS frequency noise when supplied with batteries. The sensor output was buffered (LT1220) and monitored using a frequency counter (53132A, Agilent). Sample signatures of 20 μm, 15 μm and 10 μm PSS detected by the 5-stage sensor are shown in Fig. 4.4. Also sample signatures of 15 μm and 10 μm PSS and a biological CHO cell with the 3-stage sensor is shown in this figure.

Sensor sensitivity can be calculated by its minimum detectable capacitance (MDC) as:

$$\text{MDC} = \frac{\text{Detected Capacitance}}{\text{SNR}} \quad (4.3)$$

---

<sup>3</sup> GGB Model 35, high impedance probe has a frequency response of DC to 26 GHz. The input capacitance of the probe is 50 fF, which based on the measured sensitivities in Table 4.4, it affects oscillation frequencies by less than 2% in worst case.

It has been shown [5] that the capacitance changes for these microelectrode dimensions, when a 6  $\mu\text{m}$  PSS flows  $7\pm 1 \mu\text{m}$  above the microelectrodes, is  $\sim 48\pm 4 \text{ aF}$ . For higher sensitivity, PSS are driven at  $\sim 100\text{-}200 \mu\text{m/s}$  in this work, such that particles stay close to detection microelectrodes. A 10  $\mu\text{m}$  PSS driven at  $200 \mu\text{m/s}$  velocity in a microfluidic channel with a height of  $100 \mu\text{m}$ , achieves an altitude of  $\sim 6.1 \mu\text{m}$  in the channel (particle center to the bottom of the channel) [39]. Capacitance change scales linearly with particle volume when particle is far from coplanar electrodes. Neglecting nonlinearity in this case, the capacitance change induced by a 10  $\mu\text{m}$  PSS passing above the microelectrodes of this design at the mentioned velocities can be estimated  $\sim 220 \text{ aF}$ .

So using the signatures shown in Fig. 4.4, the capacitance sensitivity of 3-stage sensor was calculated to be  $\sim 0.57 \text{ MHz/fF}$  and for the 5-stage sensor is found to be  $0.134 \text{ MHz/fF}$ . Also using the 10  $\mu\text{m}$  signatures obtained from each sensor, the minimum detectable capacitance of the 3-stage and 5-stage sensors can be calculated to be  $14 \text{ aF}$  and  $33 \text{ aF}$  respectively.

#### **4.6 Sensor Bandwidth**

In the measurement results shown in Fig. 4.4, an averaging time period of  $100 \text{ ms}$  was used for the frequency counter. This is proportional to a bandwidth of  $10 \text{ Hz}$ , resulting in a slow cytometer. In practice fast cytometers are desired to analyze  $1000\text{'s}$  cells in a second. As the sensor sensitivity stays constant, by reducing averaging time, increasing bandwidth also increases the noise. For large enough averaging time frames, flicker noise is dominant [71, 73], and the noise floor is limited by the ratio of  $(\kappa/\zeta)^2$  in which  $\kappa$  is the white noise multiplicand and  $\zeta$  is the flicker noise multiplicand.

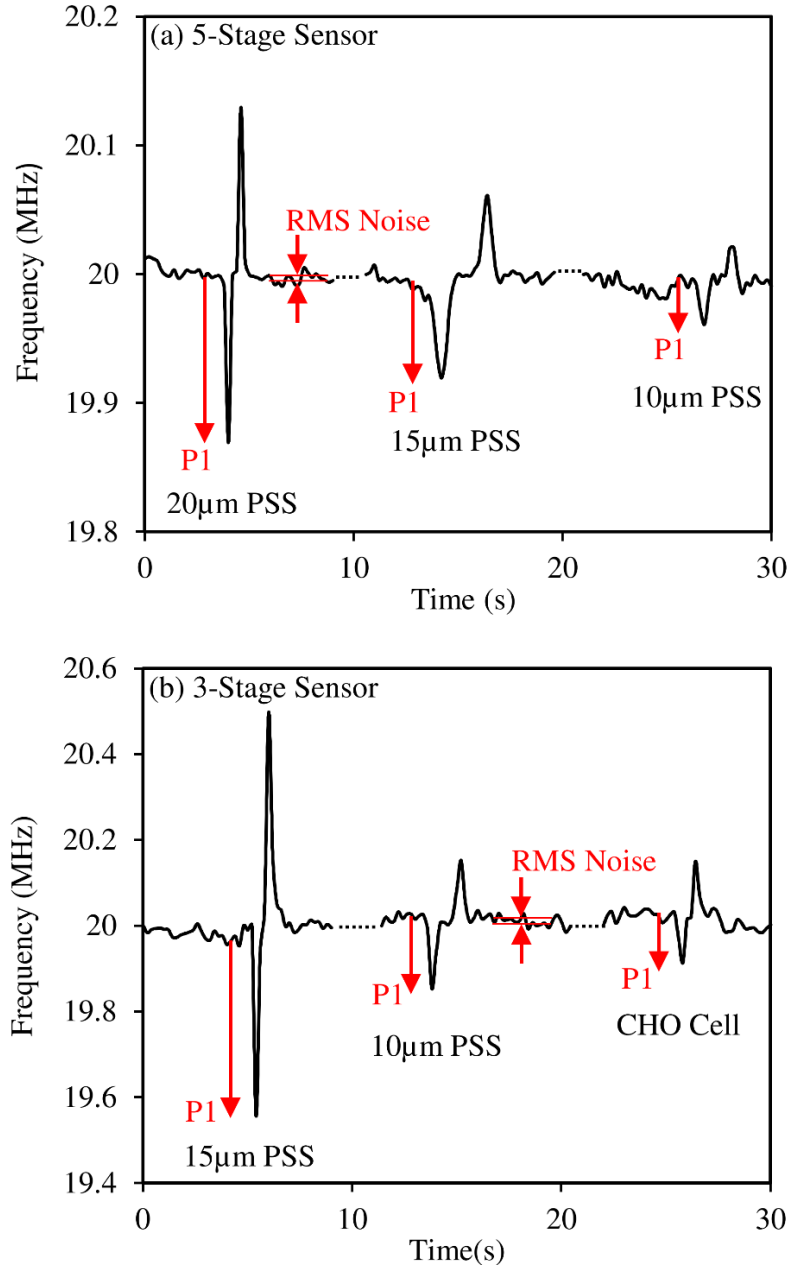


**Figure 4.4:** Sample signatures of PSS and CHO cell detected by the CMOS chip. (a) Signatures from 5-stage sensor. For 20 μm PSS P1=130 kHz, for 15 μm PSS P1=74.7 kHz, and for 10 μm PSS P1=34.6 kHz. RMS noise is ~5 kHz. (b) Signatures from 3-stage sensor. For 15 μm PSS P1=433 kHz, for 10 μm PSS P1=161 kHz, and for CHO cell P1=93.9 kHz. RMS noise is ~10 kHz.

In this design, increasing the bandwidth will not increase noise floor linearly. The reason is because the noise is dominated by flicker noise due to the large averaging time. To demonstrate this effect,

the sensor noise was measured with 100 ms, 10 ms and 1 ms frequency counter averaging time frames. The results are shown in Table 4.3. The noise increases by less than a factor of 2 for a 100 folds' increase in bandwidth. This increase in noise can be either from the flicker noise or thermal noise of both transistors and the supply. This means that if the sensor capacitive sensitivity can be enhanced by a factor of less than 2, the sensor bandwidth can be increased by a factor of 100 keeping the minimum detectable capacitance constant. Other design modifications can also be implemented to make a faster cytometer. The channel height in this design is 100  $\mu\text{m}$ . To drive cells close to the microelectrodes and controlling their altitude, they are driven at very low velocity (100  $\mu\text{m/s}$ -200  $\mu\text{m/s}$ ). At very high velocities, cells get driven almost at the middle of the channel height. So to make a faster cytometer, channel height can be reduced which with an enhancement in sensitivity can result in a faster cytometer.

**Table 4.3:** System noise for different averaging time frames.

Averaging Time	100 ms	10 ms	1 ms
RMS Frequency Noise	10.1 kHz	11.5 kHz	14.4 kHz

#### 4.7 Conclusion

A differential ring oscillator based capacitance sensor was designed and implemented on chip using 0.35  $\mu\text{m}$  CMOS technology. The sensor makes use of on-chip ring oscillators to generate GHz frequency signals to enable cell detection using the coplanar microelectrodes on the top most layer of the chip. The use of tapered 3-stage and 5-stage ring oscillators allowed operation frequency and sensitivity to be maximized with a minimal detection voltage on the microelectrodes. The sensor was tested using polystyrene spheres and achieved a  $\sim 14$  aF in capacitive sensitivity at 1.4 GHz with an off chip frequency counter averaging time frame of 100 ms. Integration of the frequency

counter on chip with the other parts of the sensor makes a complete lab on chip system for detection and analysis of biological cells.

In the next chapter, more details about design requirements, simulations, implementation, and testing will be given. Also, Statistical analysis of PSS and CHO cells signatures collected by the integrated DEP cytometer will be discussed.

## **Chapter 5: GHz Frequency CMOS DEP Cytometer for Characterization of Single Biological Cells**

### **5.1 Abstract**

A detailed review of the requirements for designing a capacitance cytometer for detection of single biological cells on chip has been completed. Based on the required specifications, an integrated DEP cytometer has been designed and implemented using a standard 0.35  $\mu\text{m}$  CMOS technology. This design makes use of differential ring oscillators which the frequency shifts between the two ring oscillators, in presence of a cell, is detected through an XOR gate and a frequency counter. This sensor has  $\sim 14$  aF capacitance sensitivity at  $\sim 1.4$  GHz. It is used for detection of 10-20  $\mu\text{m}$  polystyrene spheres and Chinese hamster ovary cells using coplanar microelectrodes on top of the CMOS chip. The design demonstrates that it is possible to differentiate between particles experiencing an altitude change resulting from either a positive or negative dielectrophoretic force in a microfluidic channel. The total area occupied by the detection electrodes and ring oscillator sensor is  $0.6 \text{ mm}^2$ . The sensor integrates all of the required parts of a DEP cytometer, making a complete lab on chip system for single cell detection and analysis.

### **5.2 Introduction**

Integrated CMOS characterization devices with single biological cell sensitivity have many possible applications [78]. Electrical detection and analysis techniques make these chips markerless compared to conventional chemical-optical methods, such as Trypan blue exclusion, that uses dyes for detection that can modify the cell physiology [4, 5]. Integrating these electronic sensors with flow cytometry allows for the rapid capture of single cell properties [18]. Microscale sensor dimensions reduces the required sample size, and is desirable for single cell analysis applications [79]. Single cell analysis is advantageous in revealing properties of subpopulations of

cells that are hidden in the average or bulk response such as in detecting circulating tumour cells [1]. In addition, these integrated sensors will be low cost, disposable, portable and may be manufactured via mass production techniques [79].

Several research groups have reported success in achieving some aspects of detection and analysis of single biological cells using microelectronic chips. In 2003, Manaresi et al. designed an integrated 8×8 mm sensor-actuator for single cell sorting, and manipulation using 0.35 μm CMOS technology. They used embedded optical photodiodes for detection [80]. The sensor was used for separating K562 tumour cells from a bulk cells without the need for fluid flow [81]. Recently, Lee et al. designed a CMOS integrated impedance cytometer operating between 20 kHz-1 MHz, and achieved 0.07% impedance resolution with a 300 mV excitation voltage. The sensor was used to characterize single red blood cell deformity at a flow rate of 0.33 μL/minute [82]. Niknejad et al. designed coupled quadrature oscillators that energized detection coils sensitive to super-magnetic labelled mouse embryonic fibroblast cells [83]. The sensor was integrated on a 1.1 × 1.3 mm die using a 0.18 μm CMOS technology and had a detection rate of 20 cells/sec [83]. In another design [84], an integrated interferometric capacitance sensor was designed using a 65 nm CMOS technology which included injection locked Colpitts oscillators at 6.5 GHz/17.5 GHz to achieve 1.5 aF capacitance resolution. This sensor was used to detect 5.8 μm polystyrene spheres (PSS) at 40-160 mm/s velocities, and is to be used for detection of biological cells [84].

For the CMOS based capacitive detection of mammalian cells, with diameters of 10-15 μm, several design requirements need to be met to achieve success. The primary design aspects include the dimension and materials of the detection microelectrodes, the sensor signal to noise ratio (SNR), an appropriate detection frequency, a suitable peak-peak voltage signal applied to the detection

microelectrodes, the integration of the microfluidic channels, and the required magnitude of sensor bandwidth.

The dimensions of the electrodes can be optimized to achieve the highest sensitivity. The width of the detection microelectrodes should be close to the cell diameter to achieve maximum impedance sensitivity. This is reported about 25  $\mu\text{m}$  for a cell size of  $\sim 18 \mu\text{m}$  in diameter [85]. The length of these electrodes is largely dictated by the width of the channel, normally 50-150  $\mu\text{m}$  [10, 82, 84]. A narrower channel increases the possibility of clogging but has the benefit of decreasing the detection microelectrodes capacitance versus the change that is induced by the biological cells, which in a capacitive sensor, will lead to higher sensitivity. For two parallel coplanar electrodes of width “W”, length “L” and interelectrode spacing “D” the capacitance can be calculated by [86]:

$$C = \frac{2\epsilon_{eff}\epsilon_0 L}{\pi} \ln \left( \left( 1 + \frac{2W}{D} \right) + \sqrt{\left( 1 + \frac{2W}{D} \right)^2 - 1} \right) \quad (5.1)$$

For 25  $\mu\text{m}$  wide microelectrodes spaced by 25  $\mu\text{m}$ , each 100  $\mu\text{m}$  in length translates to  $\sim 45$  fF on glass if the channel is filled with DI water [9]. On silicon substrates, this value depends on which metal layer is used for detection and the dielectric material between microelectrodes and substrate ground plane.

The materials need to be compatible with the chemistry and biological processes. Most integrated circuits technologies use common metals such as Al or Cu for interconnect fabrication [87]. These are not always biocompatible, unless used with passivation layers [80] or post processed to be coated with less reactive metals such as gold [88]. The use of passivation for capacitance detection degrades the capacitance sensitivity. Post processing also increases the fabrication complexity. Aluminium oxidizes in air and water spontaneously, which forms a  $\sim 2-4$  nm  $\text{Al}_2\text{O}_3$  stable passivation layer [89]. This layer is chemically inert, corrosion resistant [90] in a pH range of 4 to

8.5 [91], and protects the metal from further oxidization. In CMOS technologies Al interconnects are  $\sim 1 \mu\text{m}$  thick, and can often be used for detection directly. The oxidation process of aluminium continues however with an exponential trend over time (rate depends on temperature and moisture), which cause the electrodes completely oxidized in long term.

The magnitude of the AC signals applied to the microelectrodes, used to detect the capacitance perturbations due to the presence of cells, needs to be kept below certain limits. DC voltages above a few hundred millivolts will deteriorate electrodes over time due electrochemical reactions [30]. AC signal frequencies used for biomaterial analysis are mostly above a few 10's kHz to avoid electrothermal, electrochemical and electrode polarization effects [30]. It has been shown [92] that for the specified microelectrodes dimensions, electrode polarization effects can extend above 100 kHz for the conductive mediums which are necessary to keep cells viable during measurements. In the MHz range, cells experience Maxwell-Wagner effects, causing unpredictable dielectrophoretic forces (DEP) [6]. It is very important that the detection signal do not actuate the cells, because this will change their altitude and hence the detected signal level, which may be incorrectly interpreted as a change to the cells biological characteristics. The more ideal detection frequency is above a few 100 MHz to GHz range, where there is a second cross over frequency of the Clausius-Mossotti factor for cells [93]. Above this frequency the dielectric properties of cells change relatively little with frequency and hence this is a good range for detection [59]. Changes in the capacitance in presence of a cell, is due to dielectric contrast between cell and its medium. Biological environments almost always have water as their main subcomponent. Above  $\sim 2$  GHz and extending to  $\sim 50$  GHz the dispersion of the water molecules contributes to measurement uncertainty [94]. In this range, the dielectric response from water is not constant and water dipole response changes with the applied signal frequency, resulting in the

degradation of sensor sensitivity. Sensors designed in this frequency range require extra analysis translating sensor signals to cell biological properties. Therefore, for detection of single cells, with minimal frequency dependence, an ideal frequency range is from ~500 MHz-2 GHz.

Capacitance sensors with resolutions up to ~12 zF has been designed for applications such as integrated gyroscopes [51]. These sensors operate at kHz-MHz range (not appropriate as stated before), within various electronic components bandwidth such as high gain amplifiers [36]. Capacitance detection for microfluidic applications in the GHz range has been reported previously using bulky connectorized components [10], using discrete components on printed circuit boards [25], and recently on chip [84, 95]. In these devices, GHz frequency signals were applied to detection microelectrodes, and a frequency or phase change was obtained by down converting the signal to kHz-MHz range using mixers. Chopping can also be used in this case to minimize the effect of  $1/f$  noise. Using GHz frequency oscillators on chip can be implemented using two main types of oscillators; ring oscillators and LC-tank Colpitts oscillators. The latter proved to have better phase noise performance than the former [72, 73]. The more stable the oscillator frequency is, the higher its sensitivity will be. Colpitts oscillators are popular in RF transceivers, making use of large coils which cost die area. Therefore, they have lower integration capability for bioelectronics sensors. On the other hand, ring oscillators designs only require an appropriate number of transistors and can be much more compact.

For single cell detection aF sensitivity is required. The capacitance changes from a 6  $\mu\text{m}$  PSS  $7\pm 1$   $\mu\text{m}$  above microelectrodes with the specified dimension is  $\sim 48\pm 4$  aF [25]. This capacitance change scales with particle volume and the real part of Clausius-Mossotti factor ( $\text{Re}\{\text{KCM}\}$ ) [25, 39]. So a 10  $\mu\text{m}$  PSS at the same height in channel induces  $\sim 222$  aF capacitance change. A 10-15  $\mu\text{m}$  diameter Chinese Hamster Ovary Cell (CHO) in low conductivity medium, has a  $\text{Re}\{\text{KCM}\}\approx 0.1$

at GHz frequency [93]. So compared with a PSS with  $\text{Re}\{K_{CM}\} \approx -0.5$ , the capacitance they induce on the microelectrodes can be estimated 45-150 aF. So to achieve a SNR ratio of  $\sim 10$  in detection, a minimum sensitivity of 15 aF is required for a mammalian cell of that volume.

The detection voltages signal level is another consideration. It has been shown that in GHz range, voltage signals above 300 mV p-p can actuate cells for the stated microelectrodes dimensions [39]. The requirement for small detection voltage on microelectrodes translates into smaller charge displacement in presence of cells and will degrade the signal to noise ratio.

Integration technologies that meet more of the requirements are more desirable. CMOS technology can meet many of the requirements. Ring oscillators can be sensitive detectors of reactance changes [71]. For example simulations performed in this work predicted that a 3-stage ring oscillator with  $(W/L)_n = (2.4 \mu\text{m}/0.35 \mu\text{m})$  and  $(W/L)_p = (3.8 \mu\text{m}/0.35 \mu\text{m})$  using a  $0.35 \mu\text{m}$  CMOS technology resulted in an oscillation frequency of  $\sim 3.1$  GHz. As long as sufficient capacitance sensitivity can be achieved, this technology meets many of the requirements. The use of shorter gate length technologies is not an advantage necessarily as the size of detection microelectrodes and mounting regions in a constant area will dominate the required area. The sensor must have enough driving capability to drive the microelectrodes capacitance. With shorter gate length technologies, a larger W/L ratio of the inverters will need to be maintained to supply the same current ( $I = C \text{ dV}/\text{dt}$ ).

For electronic detection systems operation bandwidth is important as it defines its speed in detection; A higher bandwidth results in faster detection. For a pair of coplanar electrodes  $25 \mu\text{m}$  wide with  $25 \mu\text{m}$  inter-electrode spacing and cells moving at  $2 \text{ mm}/\text{s}$  the cell passes between the electrodes in  $12.5 \text{ ms}$ . A bandwidth of greater than  $\sim 20 \text{ Hz}$  would be required to resolve the signal arising from a cell passing between the electrodes. At this velocity, fluid flow imposes “lift” forces

on the cell biasing towards the middle of the channel. Short channel heights can be used to pass cells close to detection microelectrodes for higher sensitivity [9,10]. Also coplanar detection microelectrodes cause signal with amplitudes that depend on the cells altitude in the channel as the electric field reduces with distance squared. This is an important consideration when signal amplitude is translated into a cell size. So single cells velocity and height in the channel should be well controlled based on the sensor sensitivity and bandwidth.

This work demonstrates a CMOS based ring oscillator detector that is suitable for dielectrophoretic analysis of single mammalian cells. This design advances on a printed circuit board design [26]. In this detection circuit, the frequency of two ring oscillators, each connected to a pair of microelectrodes, are compared using an XOR gate and detected by a frequency counter. The sensor can operate at ~500 MHz or 1.4 GHz. The detection voltage on the microelectrodes was as low as ~1.4 V with a 3 V supply. The sensor minimum detectable capacitance is ~14 aF with a 100 ms averaging time. The design has been implemented using a 0.35  $\mu\text{m}$  CMOS technology on a 2 $\times$ 2 mm die. The sensor with coplanar electrodes occupies a total of 0.6 mm<sup>2</sup>. In this demonstration, a microfluidic channel was mounted on top of the chip to drive the fluid carrying cells over the detection microelectrodes. The sensor has been successful in detecting 10  $\mu\text{m}$  diameter PSS and CHO cells. The chip has also demonstrated its application as a DEP cytometer for both PSS and CHO cells [9]. It proves to be useful for GHz detection of single cells altitude change due to both applied positive DEP (PDEP) and negative DEP (NDEP) forces.

### **5.3 System Design**

Design architecture is shown in Fig. 5.1 (a). Two nominally identical ring oscillators are each connected to a pair of detection microelectrodes. The DC signal from oscillators is decoupled by series capacitors. The ring oscillator frequency depends on the microelectrode capacitance. In

presence of a  $\Delta C$  capacitance perturbation, due to a cell passing in proximity of the microelectrode, causes the oscillator's frequency to shift by  $\Delta f$ , proportional to  $\Delta C$ . The outputs of oscillators are connected to an XOR gate that is used for phase detection [96]. The XOR gate produces a signal that has a fundamental frequency given by the ring oscillators, that is pulse width modulated at the difference frequency. The signal is then passed through a low pass filter to remove the high frequency components, leaving only the difference frequency. This difference or IF frequency was then monitored using a frequency counter (53132a, Agilent).

### **5.3.1 Detection Microelectrodes**

Microelectrodes were implemented on the chip surface for detection using 0.35  $\mu\text{m}$  CMOS process top most metal layer which were connected to the oscillators through vias. Electrode materials are aluminium that are used without a passivation layer to maximize sensitivity. Each detection microelectrode and its ground is 25  $\mu\text{m}$  wide with an interelectrode spacing of 25  $\mu\text{m}$ . Interelectrode spacing between grounds is 130  $\mu\text{m}$  with DEP microelectrode sitting at the center between the electrodes, with a total width of 65  $\mu\text{m}$ . Ground connections are the inner microelectrodes used to minimize the interference from kHz-MHz range DEP signal to the GHz frequency detection signal. The DEP microelectrode is used with passivation for protection, as kHz-MHz signals are being used with a 1-4 Vp-p. The length of the microelectrodes is 400  $\mu\text{m}$  and the width of the microfluidic channel is 350  $\mu\text{m}$ . Microelectrodes can be seen in the final chip micrograph in Fig. 5.1 (b).

### **5.3.2 Ring Oscillator Design**

A ring oscillator is made by cascading an odd number of inverters in series. Based on the specified design constraints, the oscillation frequency of oscillator should be between 500 MHz-2 GHz, with the maximum possible sensitivity (minimum required was 22 aF), and a minimized voltage swing

on detection microelectrodes. For a symmetric inverter the total propagation time can be given by [77]:

$$\tau_p = \frac{2C_{Load}}{K_n (V_{DD} - V_{T,N})} \left( \frac{2V_{T,N}}{V_{DD} - V_{T,N}} + \ln \left( \frac{4(V_{DD} - V_{T,N})}{V_{DD}} - 1 \right) \right) \quad (5.2)$$

So the frequency sensitivity to capacitance change of the microelectrodes attached to one stage is proportional to:

$$\frac{\partial f_{osc}}{\partial C_{Microelectrode}} \propto \frac{K_n}{(C_{Parasitic} + C_{Microelectrode})^2} \quad (5.3)$$

Where in (5.2),  $K_n$  is the inverter NMOS transconductance,  $V_{DD}$  is the supply voltage,  $V_{T,N}$  is NMOS threshold voltage, and  $C_{Load}$  is the load capacitance in the output of the single inverter stage. In (5.3)  $C_{Microelectrode}$  and  $C_{Parasitic}$  are the capacitance of the microelectrode and inverter equivalent to  $C_{Load}$ . The capacitance,  $C_{Parasitic}$ , includes all of the capacitances connected to the input of the inverter in the oscillator cascade.  $C_{Parasitic}$  is dominated by the input gate capacitance of the transistors of the inverter. Keeping  $L$  constant,  $K_n$  and  $C_{Parasitic}$  are both linearly proportional to transistors width,  $W$ . The maximum sensitivity occurs when  $C_{Parasitic} = C_{Microelectrodes}$ . Using minimum sized inverters maximizes the oscillation frequency but creates a low sensitivity to capacitance change and vice versa. In the present design a tapered ring oscillator architecture was used to obtain a balance between the oscillation frequency, and sensitivity.

Initially a symmetric single inverter unit cell with  $(W/L)_n=(2.4 \mu\text{m}/0.35 \mu\text{m})$  and  $(W/L)_p=(3.8 \mu\text{m}/0.35 \mu\text{m})$  was used. Cascading 3 stages of these inverters in  $0.35 \mu\text{m}$  technology resulted in a 3.1 GHz frequency. The input and output parasitic capacitance of this inverter was found to be 2.45 fF and 0.6 fF, respectively. The tapered ring oscillator was designed for a total load capacitance of  $C_{Load}=2 \text{ pF}$  connected to the last stage. This load was the estimated maximum

observed in off-chip microfluidic systems [9, 10]. For maximum frequency [77], the inverter capacitances are given by:

$$C_{\text{Load}} = \alpha^{N+1}C_g \quad (5.4)$$

$$\alpha(\ln \alpha - 1) = \frac{C_d}{C_g} \quad (5.5)$$

where,  $C_{\text{Load}}=2$  pF in the last stage,  $\alpha$  is stage scaling ratio,  $N$  is the number of stages,  $C_g$  is the input capacitance of the first stage and  $C_d$  is the output capacitance of the first stage. As  $C_d \ll C_g$  in an inverter,  $\alpha \approx 3$ . The maximum frequency can be achieved with either a 3-stage or 5-stage ring oscillator. For  $N=3$ ,  $C_g=24.7$  fF equivalent to 12 unit inverters on the first stage, resulting in 36 and 108 unit cells for the 2nd and 3rd inverters in the cascade. For  $N=5$ ,  $C_g=2.74$  fF, equivalent to a single inverter unit on the first stage and therefore 3, 9, 27 and 81 inverters were used for the 2nd through 5th stages in the cascade.

The differential ring oscillator sensor required some means to individually tune each oscillator. The frequency of oscillation depends, among many other factors, on the magnitude of the power supply voltage. In the present work, separate power supply pins were implemented for each oscillator to in order to individually tune each sensor. Oscillators connected to detection microelectrodes can be seen in Fig. 5.1 (b).

For testing purposes some ring oscillators were included that were directly connected to an output pad in the last stage. A 400 fF load capacitance was used in simulation to model the pad and the test probe capacitance. The test probe was an active probe with a bandwidth of 26 GHz and a load capacitance of 50 fF (Model 35 GGB Industries). The frequencies were measured with frequency counter (53132a, Agilent). In Table 5.1 the simulation results of the oscillation frequency are

shown for the ring oscillators. Both of the 3 and 5-stage oscillators satisfy the required operation frequency in 0.35  $\mu\text{m}$  CMOS technology.

**Table 5.1:** Oscillation frequency of the application specific tapered ring oscillators designed in CMOS 0.35  $\mu\text{m}$  technology,  $C_{\text{Load}}=400$  fF.

$f_{\text{osc}}(\text{GHz})$	Schematic	Post-Layout	Measurement
5-Stage Oscillator	1.00	0.800	0.715
3-Stage Oscillator	2.12	1.72	1.46

In this design, the ring oscillators were coupled to the detection microelectrodes on chip. The microelectrode capacitance with water above the electrodes was estimated using the CAD tool (Cadence, TSMC 0.35  $\mu\text{m}$  CMOS) at  $\sim 340$  fF. Considering the coupling capacitance between one detection microelectrode and other microelectrodes (the DEP and the other GND microelectrode) a total capacitance of 500 fF was used in the simulations of operation frequency, voltage swing and capacitance sensitivity. The results are shown in Table 5.2. Based on the simulation results, the best stage to connect the microelectrodes to is stage 2 for the 5-stage and stage 1 for the 3-stage oscillator. The measurements were done on chip with the microelectrodes connected to these stages. The operation frequency was measured in air and with deionized water (DI) water over the top of the microelectrodes. The capacitance sensitivity was measured by using flowing PSS spheres to induce known capacitance perturbations on microelectrodes [25].

### 5.3.3 Microfluidic Design

To run particles and biological cells over the chip, a 2-layer microfluidic device was machined in PMMA to be mounted on top of the CMOS chip. As shown in Fig. 5.1 (c), the device 1st layer is connected to fluid tubing with inner and out diameters of 1.09 mm and 350  $\mu\text{m}$ , respectively. In this design, the height of the channel is 100  $\mu\text{m}$ . The cells were driven very slowly (100  $\mu\text{m/s}$ -200  $\mu\text{m/s}$ ) so that they would be at the bottom of channel close to detection microelectrodes. For faster

velocities, smaller channel heights can be used [9]. The microfluidic piece was mounted on top of the chip, by aligning the channel walls vertical to the microelectrodes under the microscope. The microfluidic part is then moved slowly downward to be mounted on the CQFP44 PCB template where the chip is soldered. When the part was in contact with the chip, water was purged slowly to the channel, and screws were fixed to prevent leaking.

**Table 5.2:** Capacitance sensitivity, oscillation frequency and voltage swing of microelectrodes located at different stages of the tapered oscillator.

(a) 5-Stage Oscillator

	Post-Layout				Measurement	
	Stage5	Stage4	Stage3	<b>Stage2</b>	Stage1	Stage 2
$\partial f/\partial C(\text{MHz}/\text{fF})$	0.025	0.084	0.206	<b>0.263</b>	0.230	0.134
$f_{\text{osc}}(\text{MHz})$	795	775	684	<b>544</b>	393	512
$V_{\text{swing}}$	3.01	2.92	2.76	<b>2.31</b>	1.60	1.65

(b) 3-Stage Oscillator

	Post-Layout			Measurement
	Stage3	Stage2	<b>Stage1</b>	Stage 1
$\partial f/\partial C(\text{MHz}/\text{fF})$	0.215	0.205	<b>0.58</b>	0.57
$f_{\text{osc}}(\text{GHz})$	1.69	1.70	<b>1.40</b>	1.37
$V_{\text{swing}}(\text{V})$	2.99	1.79	<b>2.17</b>	1.42

## 5.4 Materials and Methods

Chinese Hamster Ovary (CHO) cells expressing a human llama chimeric antibody (EG2) were used for this work. Yves Durocher of the NRC, Canada kindly provided the cell line (CHODG44-EG2-hFc/clone 1A7) [97]. The cells were cultured in 250 mL baffled shaker flasks (VWR International, Radnor, PA) at 120 rpm in an incubator at 37°C with 10% CO<sub>2</sub> overlay.

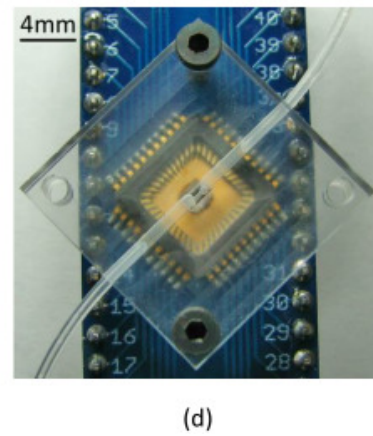
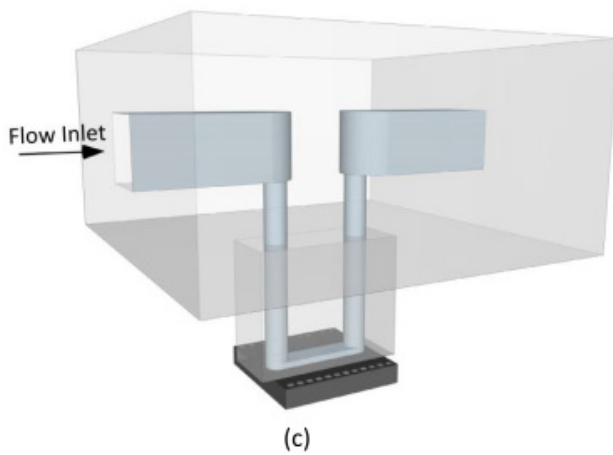
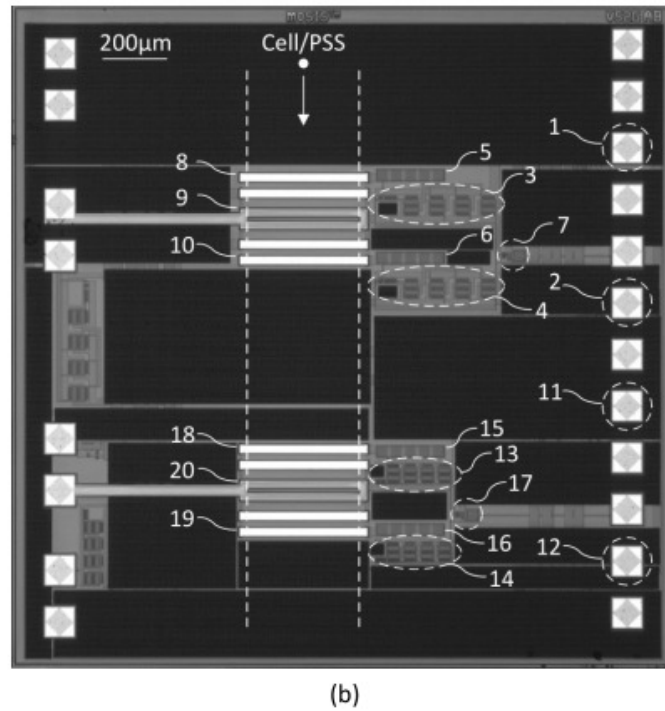
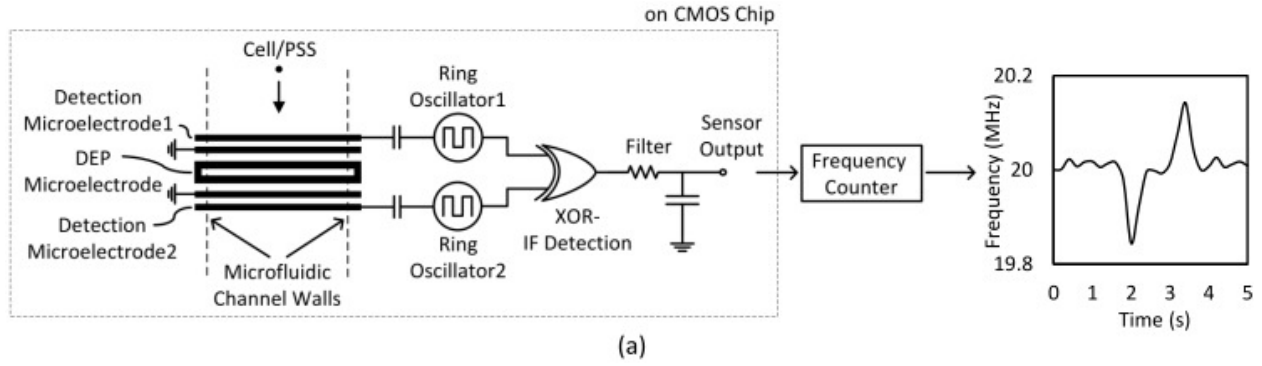


**Figure 5.1:** Design of an integrated DEP cytometer. (a) Design schematic. (b) Chip micrograph. Components description for 3-stage and 5-stage sensor are shown in Table 5.3. (c) 3D block

diagram of microfluidic part on top of chip die. (d) Integrated DEP cytometer sensor including all parts mounted together.

**Table 5.3:** Description of components and pins shown in Fig. 5.1 (b).

Component/Pin Number	Explanation
1	Supply voltage pin of 5-stage ring oscillator1
2	Supply voltage pin of 5-stage ring oscillator2
3	5-stage ring oscillator1
4	5-stage ring oscillator2
5	Decoupling capacitor of 5-stage ring oscillator1
6	Decoupling capacitor of 5-stage ring oscillator2
7	XOR-Filter of 5-stage sensor
8	5-stage sensor detection microelectrode1
9	DEP microelectrode of 5-stage sensor
10	5-stage sensor detection microelectrode2
11	Supply voltage pin of 3-stage ring oscillator1
12	Supply voltage pin of 3-stage ring oscillator2
13	3-stage ring oscillator1
14	3-stage ring oscillator2
15	Decoupling capacitor of 3-stage ring oscillator1
16	Decoupling capacitor of 3-stage ring oscillator2
17	XOR-Filter of 3-stage sensor
18	3-stage sensor detection microelectrode1
19	DEP microelectrode for 3-stage sensor
20	3-stage sensor detection microelectrode2

The cells were grown in BioGro-CHO serum-free medium (BioGro Technologies, Winnipeg, MB) supplemented with 0.5 g/L yeast extract (BD, Sparks, MD), 1 mM glutamine (Sigma, St. Louis, MO), and 4 mM GlutaMax I (Invitrogen, Grand Island, NY).

For the DEP cytometer measurement, a sample was taken from the shaker and centrifuged at 377 g for 1 min. After the supernatant was removed the cell pellet was reconstituted in fresh growth medium (37°C) and low conductivity (~0.067 S/m) medium (37°C) [22.9 mM sucrose (Sigma), 16 mM glucose (Fisher), 1 mM CaCl<sub>2</sub> (Fisher), 16 mM Na<sub>2</sub>HPO<sub>4</sub> (Fisher)] [39] using a ratio of

2:30 (fresh: low conductivity medium) diluting the cell sample to 105 cells/mL and reaching a conductivity of  $\sim 0.17$  S/m as measured by a conductivity meter (Orion 3-Star Plus, Thermo Scientific).

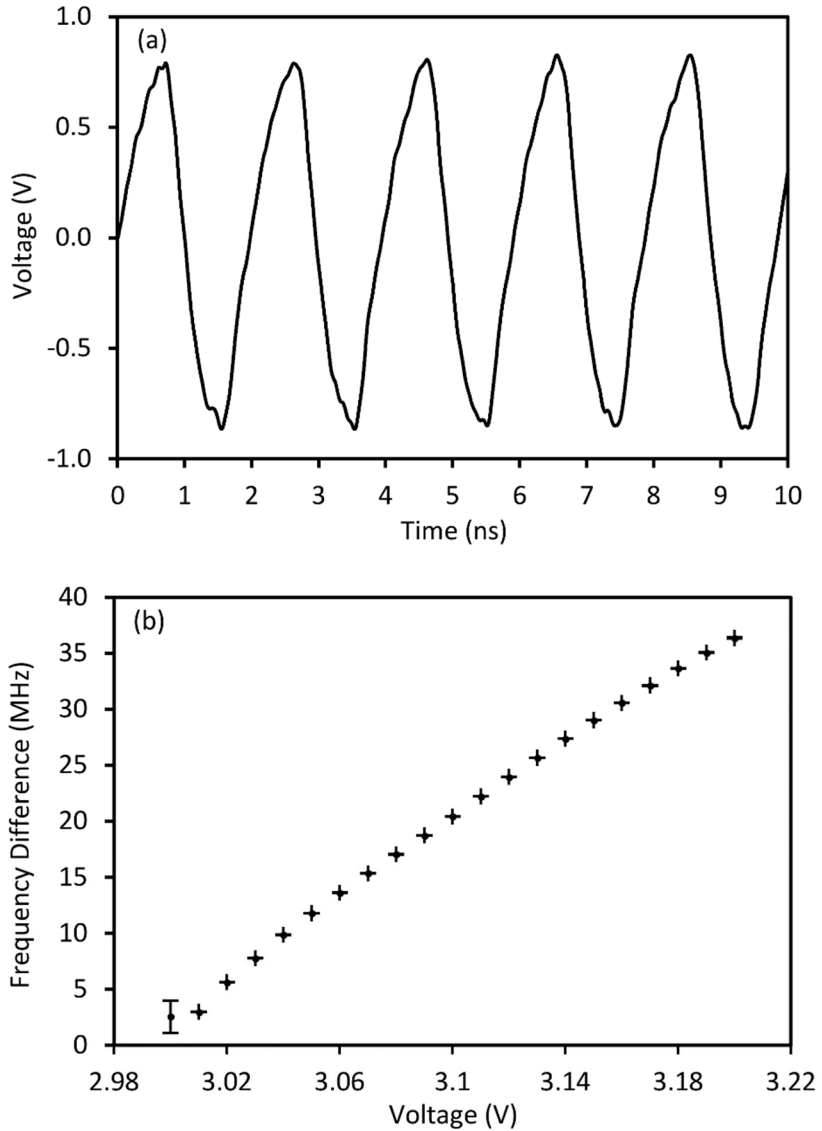
## **5.5 Results and Discussion**

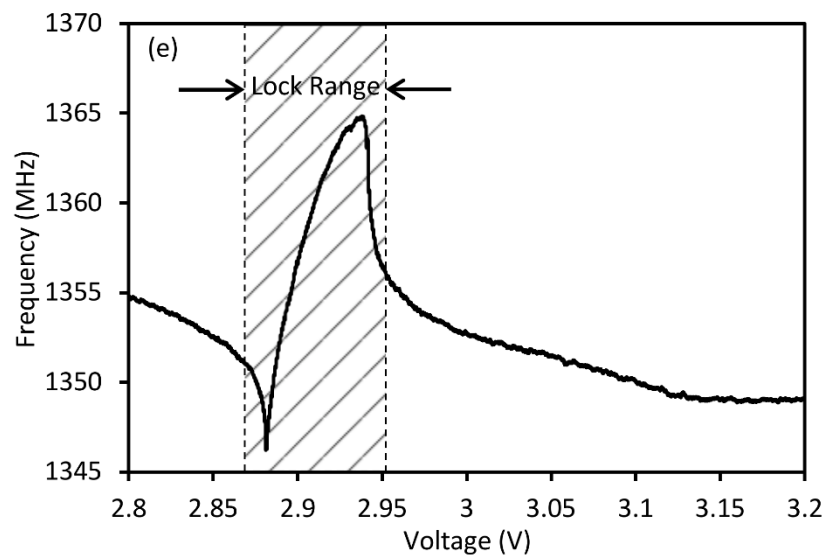
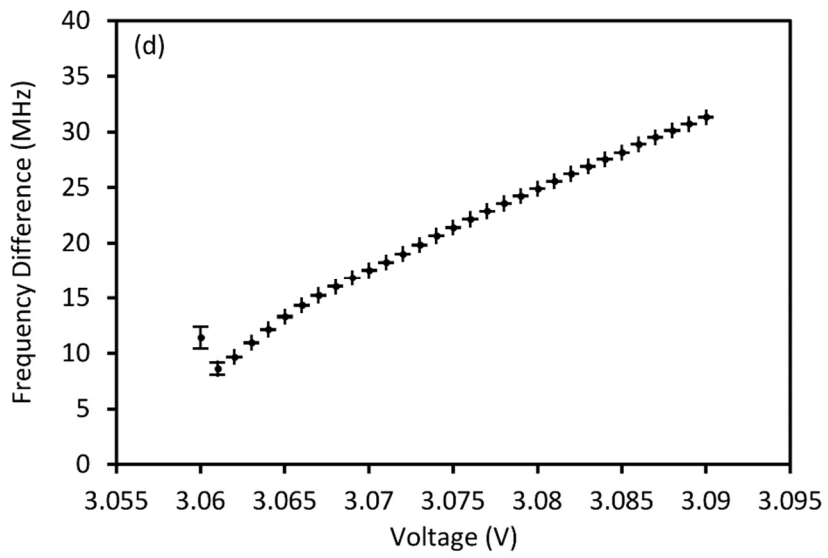
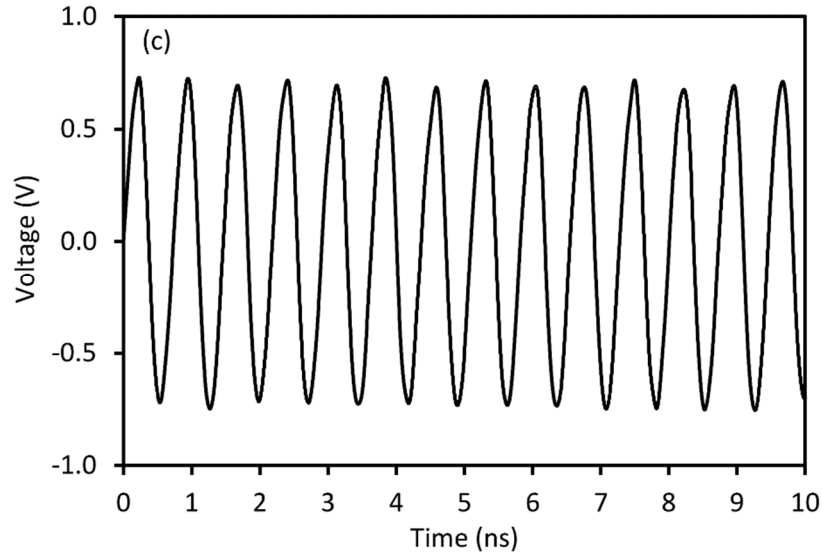
The sensor was characterized by flowing particles over the microelectrodes. To provide a low noise adjustable power supply for each oscillator a dual channel 16 bit DAC (LTC2607, Linear Technology) was used. A frequency counter (53132A, Agilent) was used to detect the output differential frequency with an acquisition period of 100 ms. The output from frequency counter was logged to a PC using Matlab. Voltage signals on chip is recorded on a 2.5 GHz oscilloscope (DSO9254A, Agilent) using a high impedance probe (Model 35, GGB Industries). The chip is then used to detect PSS and CHO cells.

### **5.5.1 CMOS Sensor Characterization**

The frequency, signal levels and power supply tuning sensitivity of the sensor was characterized before single particle testing. First only one of the oscillators of 3-stage and 5-stage ring oscillator based sensors was supplied with 3V, and the voltage on its microelectrode is recorded. The results are shown in Figs 5.2 (a) and (c) for 5-stage and 3-stage sensors respectively. The former has a 1.65 V<sub>p-p</sub> signal at  $\sim 512$  MHz on its microelectrodes, and the latter has 1.42 V at  $\sim 1373$  MHz. In both cases, the oscillators have operational frequencies above that required. However, the detection voltage magnitude is sufficient to actuate cells, as will be discussed later. In this work single cells are detected at very low velocities close to detection microelectrodes to accommodate for the sensor's ability to be used for positive DEP forces as well as negative DEP forces without the cells sticking to DEP microelectrode.

The sensitivity of the sensors to the magnitude of the supply voltage was also been tested. One oscillator supply voltage is fixed at 3V and the supply voltage of the other oscillator is changed from 3 V in steps of 10 mV for 5-stage sensor (to 3.2) and 1 mV for 3-stage sensor (to 3.09). The output difference frequency was monitored on the frequency counter to measure the sensitivity to supply changes. The results are shown in Figs 5.2(b) and (d) for the 5-stage and 3-stage sensors respectively. In this case the frequency sensitivity to supply change was measured as 0.178 MHz/mV and 0.787 MHz/mV near a difference frequency of 20 MHz for the 5-stage and 3-stage sensors respectively.





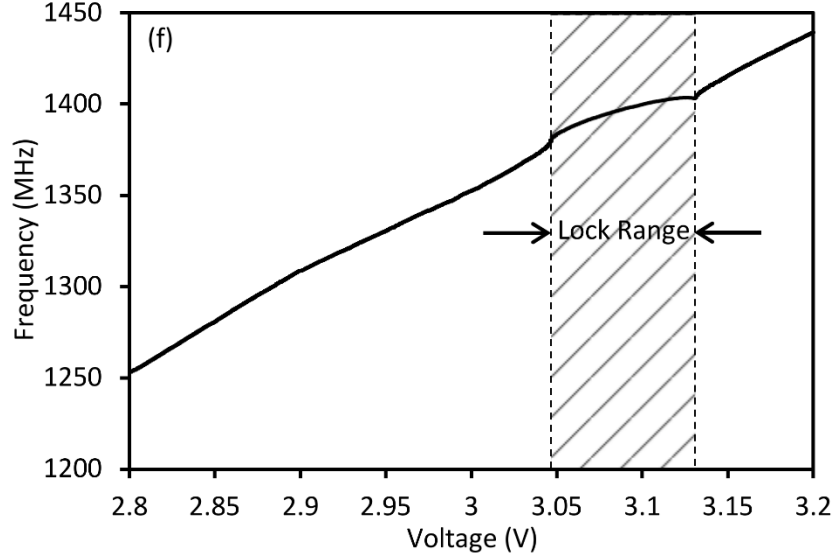


**Figure 5.2:** Characterization tests results for 5-stage and 3-stage sensors. (a) Voltage signal on sensing microelectrode of the 5-stage ring oscillator2 at VDD=3 V. Signal peak to peak and frequency are 1.65 V and 512 MHz respectively. (b) Output IF frequency change of 5-stage sensor when ring oscillator2 supply voltage is reduced from 3.2V to 3V with steps of 10mv and ring oscillator1 supply voltage is fixed at 3V.  $\Delta f/\Delta V$  is 0.175 MHz/mV around 20 MHz. (c) Voltage signal on sensing microelectrode of the 3-stage ring oscillator2 at VDD=3V. Signal peak to peak and frequency are 1.42 V and 1373 MHz respectively. (d) Output IF frequency change of 3-stage sensor when ring oscillator2 supply voltage is reduced from 3.09 V to 3.06V with steps of 1mv and ring oscillator1 supply voltage is fixed at 3V.  $\Delta f/\Delta V$  is 0.787 MHz/mV around 20 MHz. (e) Oscillation frequency of 3-stage ring oscillator1 when its supply voltage is fixed at 3V and the supply voltage of 3-stage ring oscillator2 is reduced from 3.2 V to 2.8 V with steps of 1 mV. (f) Oscillation frequency of 3-stage ring oscillator2 when its supply voltage is reduced from 3.2 V to 2.8 V with steps of 1 mV and the supply voltage of 3-stage ring oscillator1 is fixed at 3 V. The oscillators lock around 3.130 V and unlock around 3.047 V.

The value for frequency to capacitance sensitivity is found from particle detection experiments in the next section.

An important characteristic of this design architecture is the injection locking that occurs between the differential oscillators. This phenomenon was often observed in closely matched oscillators

where cross coupling occurs. In the case of ring oscillators, capacitive coupling can cause the oscillators frequencies to become locked to one another as shown in Figs 5.2(e) and (f) for the 3-stage sensor. In Fig. 5.2 (e), the supply of ring oscillator1 was fixed and was probed on its microelectrode, while the supply of ring oscillator2 was increased from 2.8 V to 3 V. The frequency of ring oscillator1 decreases until  $\sim 2.85$  V, at which point became locked onto ring oscillator2. The two oscillators remained locked until  $\sim 2.95$  V. For the sensor to work the oscillators must be adjusted to operate in the unlocked range. To achieve this in the 3-stage sensor, one oscillator frequency was tuned to  $\sim 20$  MHz above the other. This can be seen in Fig. 5.2 (f) where the oscillator1 supply voltage was fixed, and the oscillator2 supply voltage was increased from 2.8 V to 3.2 V. For supply voltages between 3.05 V to 3.13 V the oscillators are locked. Outside this range the oscillators is roughly linearly dependent with the supply voltage.

### **5.5.2 Detection of PSS**

Polystyrene spheres were used to estimate the capacitance sensitivity of the sensors. When PSS pass over the electrodes they induce capacitance perturbations measured which have been reported in other experiments [39]. Polystyrene spheres with a diameter of  $20\ \mu\text{m}$ - $10\ \mu\text{m}$  (Polysciences inc.) were suspended in DI water. Syringe pumps and pressure driven flow was used to drive the suspension over the electrodes. Signatures for the  $20\ \mu\text{m}$ ,  $15\ \mu\text{m}$  and  $10\ \mu\text{m}$  PSS, as they flow over the microelectrodes of a 5-stage sensor, are shown in Fig. 5.3 (a). Signatures peak amplitude and RMS noise of each sensor is shown in Table. IV. As expected, the signatures scale almost cubically with the sphere diameter- i.e. with the sphere volume. A  $10\ \mu\text{m}$  PSS flowing near the bottom of channel will result in a capacitance perturbation of  $\Delta C \approx 222$  aF as the PSS displaces the water when it flows past the electrode. The capacitance sensitivity of the 5-stage was found to be  $\sim 0.135$  MHz/fF. For 3-stage sensor, sample signatures of  $15\ \mu\text{m}$  and  $10\ \mu\text{m}$  PSS and CHO cells are shown

in Fig. 5.3 (b). The sensitivity of this sensor was measured to be  $\sim 0.57$  MHz/fF. From these signatures the minimum detectable capacitance was estimated to be  $\sim 14$  aF (RMS), which is sufficient for detection of CHO cells as discussed in the introduction.

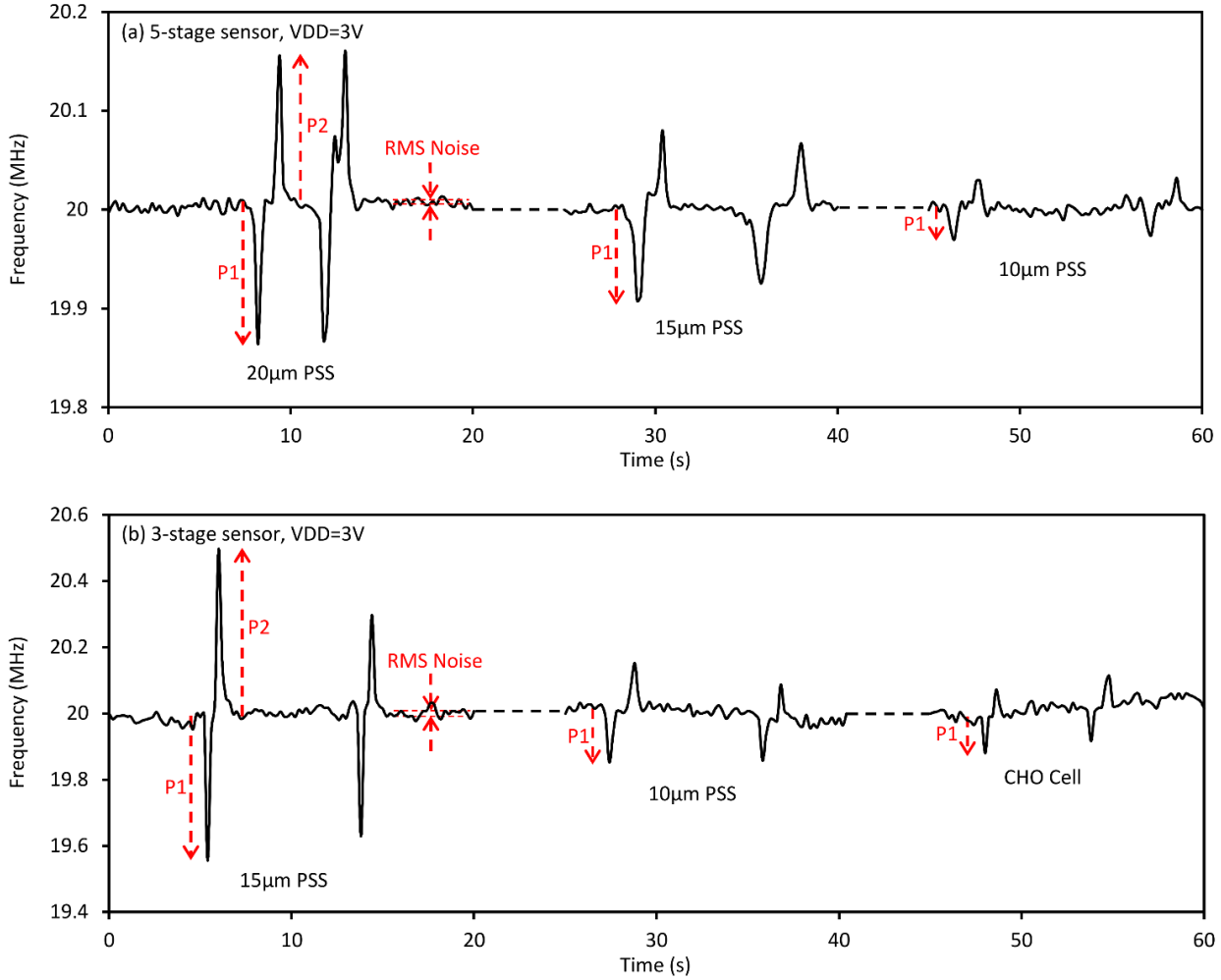


**Figure 5.3:** Sample signatures of polystyrene spheres and CHO cells detected with the chip for VDD=3 V. Signal amplitudes are shown in Table 5.4.

**Table 5.4:** Particle/cell signatures peak amplitude shown in Fig. 5.3.

(a) 5-Stage Sensor

Particle	20µm PSS	15µm PSS	10µm PSS	Noise
Amplitude	P1=145 kHz, P2=151 kHz	P1=76 kHz	P1=31 kHz	5 kHz(RMS)

(b) 3-Stage Sensor

Particle/Cell	15µm PSS	10µm PSS	10-15µm CHO	Noise
Amplitude	P1=443 kHz, P2=436 kHz	P1=195 kHz	P1=102 kHz	12 kHz(RMS)

### 5.5.3 PSS Signatures with DEP

A DEP signal is applied to DEP microelectrode at 1 MHz, 1 Vp-p in the 5-stage and the 3-stage sensors to observe the actuation of the PSS. Since the real part of Clausius-Mossotti factor is negative for PSS above a few 10<sup>3</sup> kHz [99], they experience a negative DEP (NDEP). Some sample signatures of the 15 μm beads detected with the 5-stage sensor with DEP and without DEP are shown in Fig. 5.4 (a). The same experiment was performed with 10 μm PSS using the 3-stage sensor. In both cases, the particle repulsion to higher altitudes in the channel is obvious. As particles are at a higher altitude after repulsion, the second peak is smaller and also narrower which results because the particles are pushed farther from the electrodes into to channel regions with a greater fluid velocity.

To quantitatively express the peak difference, a normalized peak difference [24] was used and is defined by

$$\text{Normalized Peak Difference} = \frac{P_1 - P_2}{P_1 + P_2} \quad (5.6)$$

where  $P_1$  and  $P_2$  are the absolute amplitude of the first and second peaks, respectively.

For the shown 15 μm PSS signature detected with 5-stage sensor in Fig. 5.4 (a),  $P_1 \approx 66$  kHz and  $P_2 \approx 63$  kHz when no DEP voltage is applied. The normalized peak difference in this case is -0.023, a value close to zero, because the peaks are almost at the same level.

For the detected 15 μm PSS signature in Fig. 5.4 (a) After applying DEP signal  $P_1 \approx 50$  kHz,  $P_2 \approx 43$  kHz. This is proportional to -0.075 normalized peak difference, which shows a shift of -0.052 compared with the previous signature. For the 10 μm PSS signatures detected with the 3-stage sensor in Fig. 5.4 (b),  $P_1 \approx 62$  kHz,  $P_2 \approx 50$  kHz when  $V_{DEP} = 0$ . On the other hand,  $P_1 \approx 45$  kHz,  $P_2 \approx 17.3$  kHz for the signature detected after applying DEP at 1 MHz, 1Vp-p. This shows a normalized peak difference shift from -0.107 to -0.455 in the former compared with the latter.

Statistical analysis of normalized peak difference can be used to find out about the amount and direction of actuation of single cells in the channel which is discussed in the next sections.

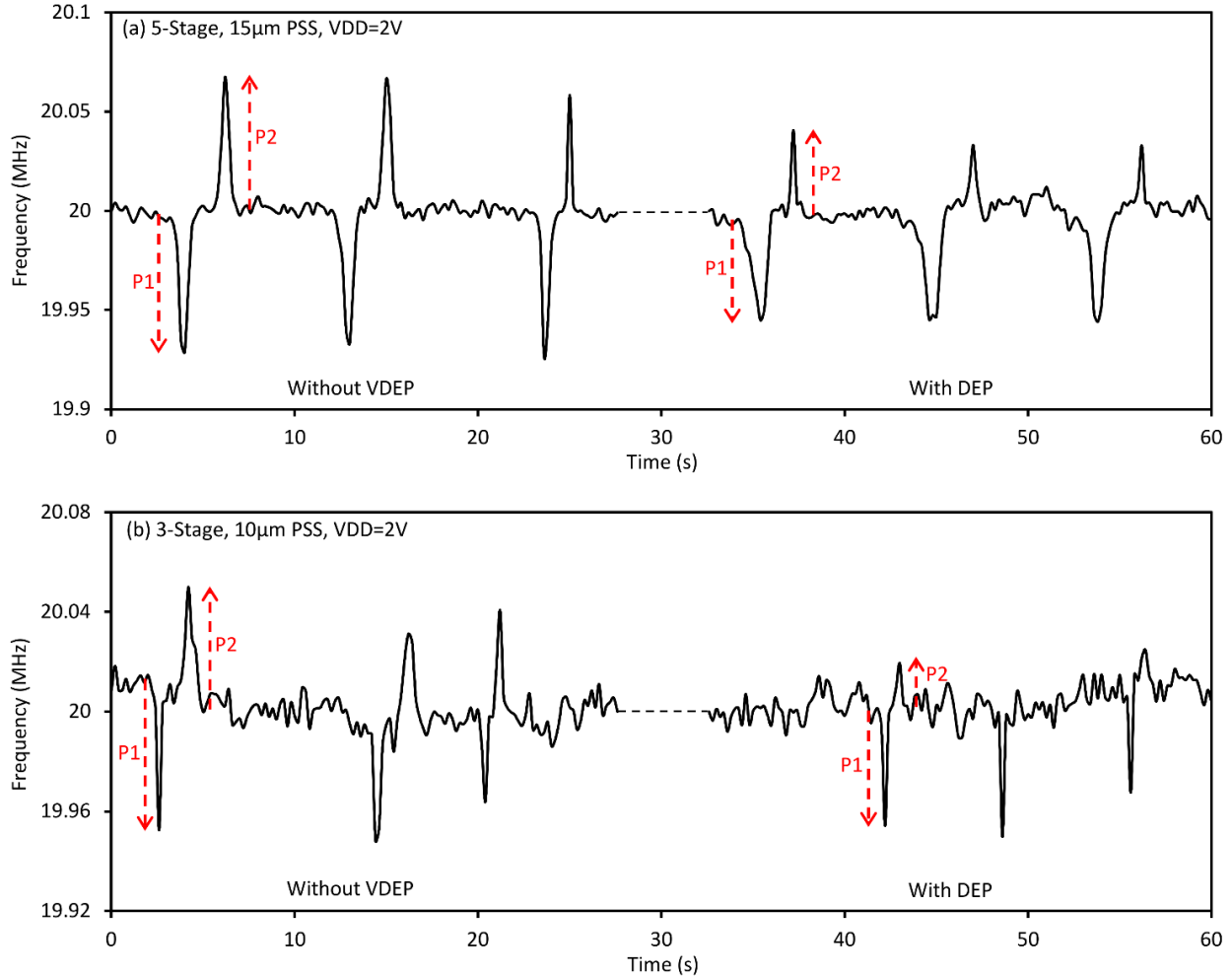


**Figure 5.4:** Sample signatures of PSS detected by the chip for  $V_{DD}=2$  V, without applying DEP signal ( $V_{DEP}=0$ ) and with DEP signal applied at 1 MHz, 1 Vp-p. (a) Signatures of 15  $\mu$ m PSS detected by the 5-stage sensor. (b) Signatures of 10 $\mu$ m PSS detected by 3-stage sensor.

It should be noted that the DEP force is proportional to the particle volume. So if 15  $\mu$ m and 10  $\mu$ m PSS were detected on the same sensor, the actuation of the 15  $\mu$ m sphere would be  $\sim 3.4$  times greater than 10  $\mu$ m ones. In Fig. 5.4, the 10  $\mu$ m beads appear to be actuated more, because they are detected with the 3-stage sensor, with an operation frequency of  $\sim 3$  times of the 5-stage sensor. This means that the detection signal in 3 stage sensor is more

concentrated toward its microelectrodes. So 15  $\mu\text{m}$  particles actuate to higher altitudes in the 5-stage sensor, but the field from this sensor extends to higher altitudes (it is less sensitive), hence it detects a lower frequency difference.

#### 5.5.4 Statistical Analysis of PSS Signatures

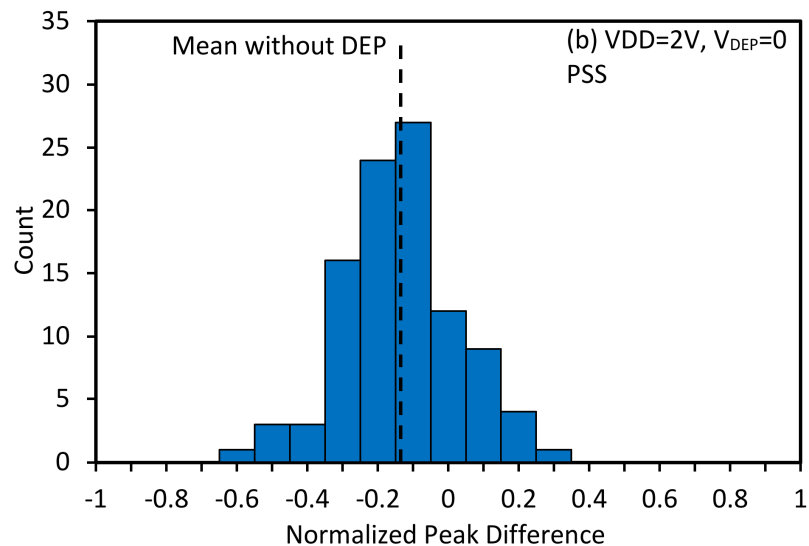
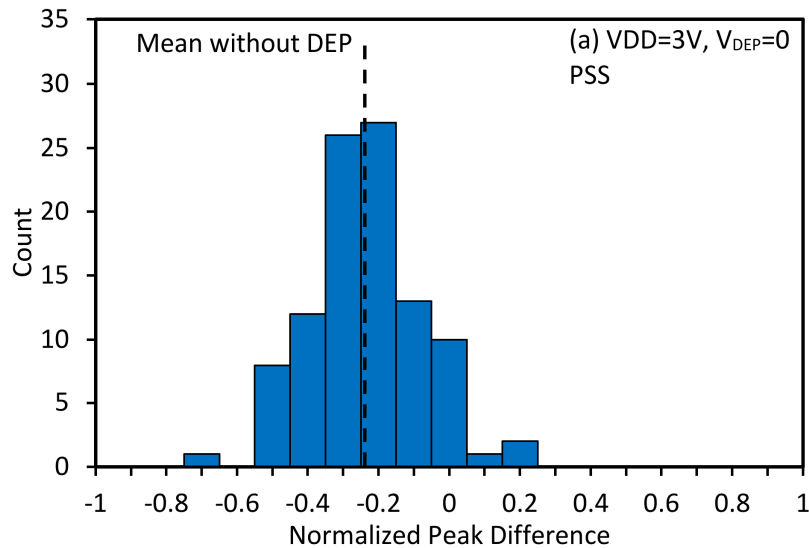
Signatures were collected with the 3-stage sensor for statistical analysis. For each case 100 signatures were collected and histograms distribution of the normalized peak difference were plotted. The results are shown in Fig. 5.5. In all cases the particle flow over the electrodes was 100 -200  $\mu\text{m/s}$ . Therefore the PSS should be found near the bottom of the channel. For the data shown in Fig. 5.5 (a), the sensor supply voltage was 3V with a  $\sim 40$  mV difference in oscillator supply voltages which resulted in a difference frequency of  $\sim 20$  MHz. Average detected signatures  $P_1$  in this case was 141 kHz. In this case no DEP (NODEP) signal was applied. The histograms show that the detection microelectrodes actuate particles, resulting in a mean negative normalized peak difference -0.237.

To reduce voltage on detection microelectrodes, the same experiment was done at 2 V supply. Average detected signatures  $P_1$  in this case was 56 kHz. The normalized peak difference distribution for a supply voltage of 2 V is shown in Fig. 5.5 (b). In this case the average normalized peak difference is -0.136. Taking the frequency reduction into account, decreasing supply voltage brings normalized peak difference closer to zero [9, 25]. Polystyrene Spheres were analysed using VDD=3 V and 2 V, and a DEP signal 1 Vp-p at 1 MHz. For VDD=3 V in presence of DEP voltage, the mean of signatures normalized peak difference was found -0.438, which shows histograms shift by 0.201 to left compared with NODEP case. For VDD=2 V, applying DEP voltage causes the mean value of signatures normalized peak difference to be -0.292. In this case histograms shift to left by 0.156 due

to applying negative DEP force to 10  $\mu\text{m}$  PSS in the channel. Clearly the negative DEP actuation of the PSS particles can be observed.

### 5.5.5 Statistical Analysis of CHO cells Signatures

A DEP signal has been shown to be able to determine a cell's viability [9]. With a medium conductivity solution of 0.17 S/m at a DEP frequency of  $\sim 6$  MHz, a viable CHO cell experiences a positive DEP force while a non-viable CHO cell experiences negative DEP force [24]. Therefore, the peak difference can be used as an indicator of the population's viability for a constant flow velocity.



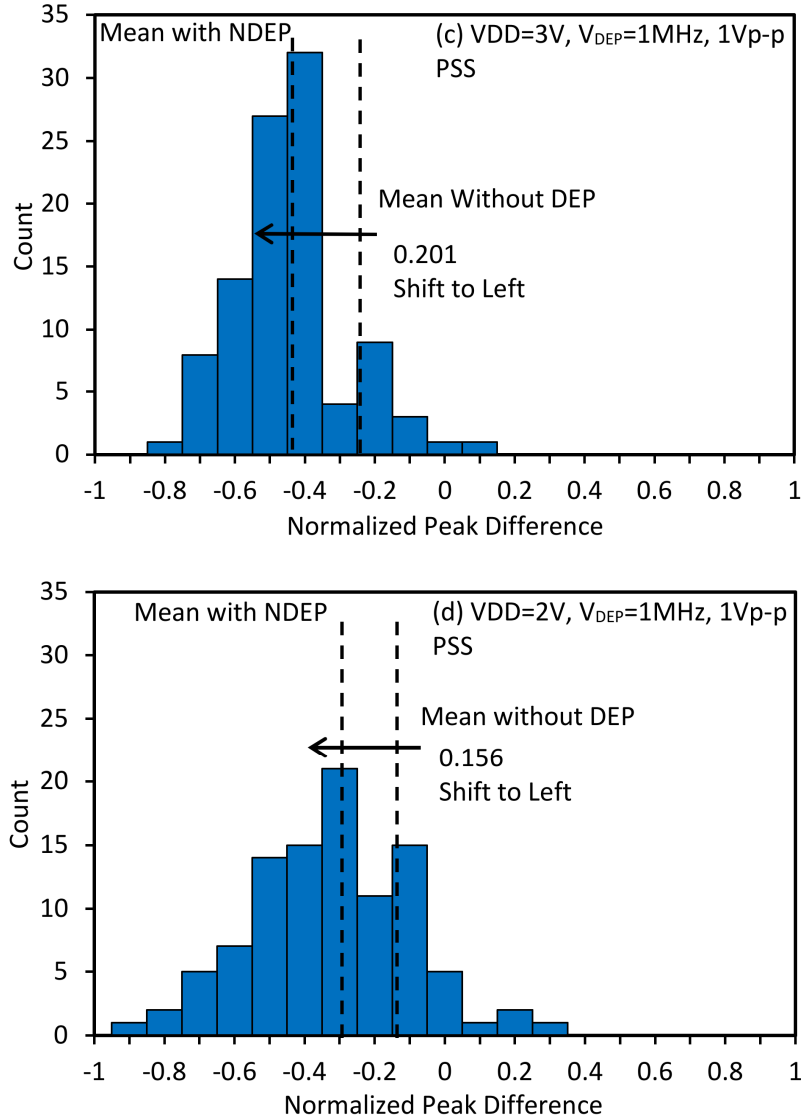
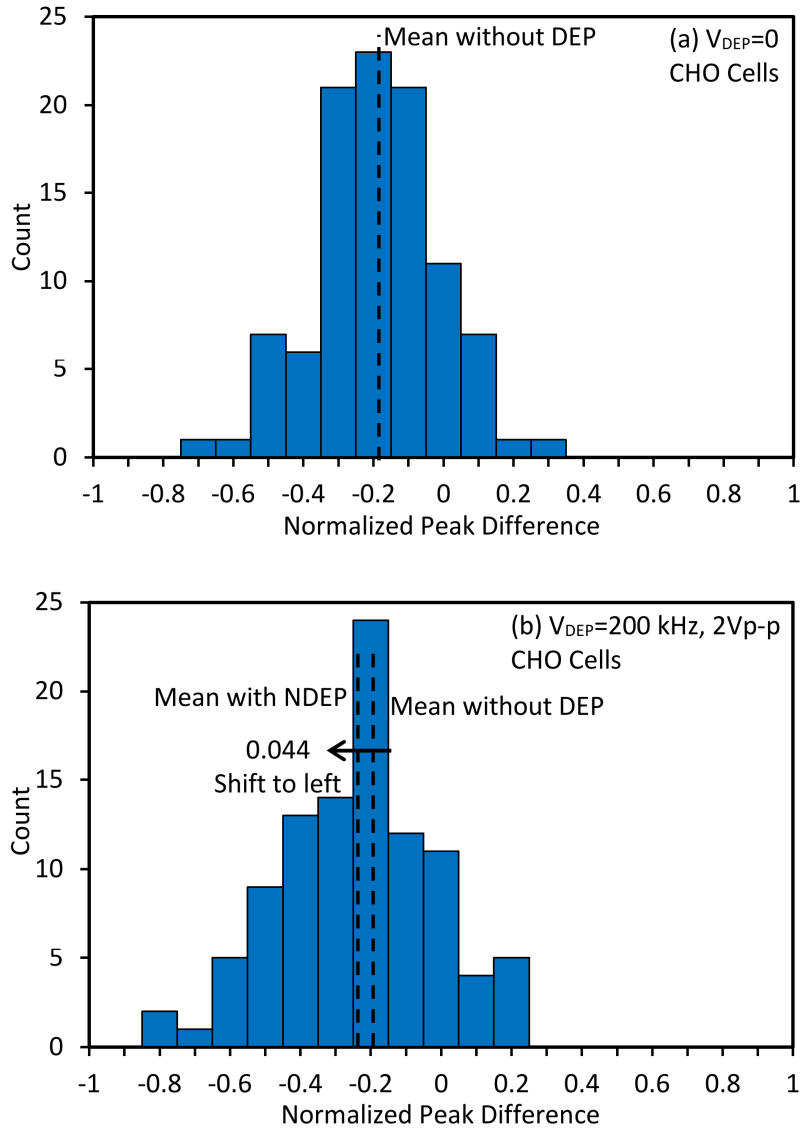


**Figure 5.5:** Normalized peak difference distribution for 100 signatures of 10 μm PSS in DI water detected by 3-stage sensor. (a) VDD=3 V, V<sub>DEP</sub>=0. (b) VDD=2 V, V<sub>DEP</sub>=0. (c) VDD=3 V and DEP signal is applied at 1 MHz, 1 Vp-p. (d) VDD=2 V and DEP signal is applied at 1 MHz, 1 Vp-p.

For CHO cell detection, a 3V supply was used to enhance the sensitivity. Conditions of NODEP, PDEP and NDEP were tested with the sensor. The CHO samples were suspended in low conductivity medium (~0.17 S/m) and were driven over the top of the microelectrodes. With a medium of this conductivity, viable CHO cells have well known frequencies where dielectrophoretic forces are positive and negative [24]. Samples were used within a one-hour time

frame to ensure that the cells remained viable for the duration of the measurements [24]. CHO cells experience PDEP when viable for a DEP signal frequency of 1 MHz, and a strong NDEP for a DEP signal frequency below 500 kHz [24, 93].

In these measurements, four cell samples were used for each case of NODEP, NDEP (2 V<sub>p-p</sub>, 200 kHz), NDEP (4V<sub>p-p</sub>, 200 kHz) and PDEP (2V<sub>p-p</sub>, 1 MHz). The viability of cell samples under the exclusion of Trypan blue by a Cedex Analyzer was measured prior to each test. Viability was reported in all cases above 97%. Statistical analysis of collected signatures is shown in Fig. 5.6.



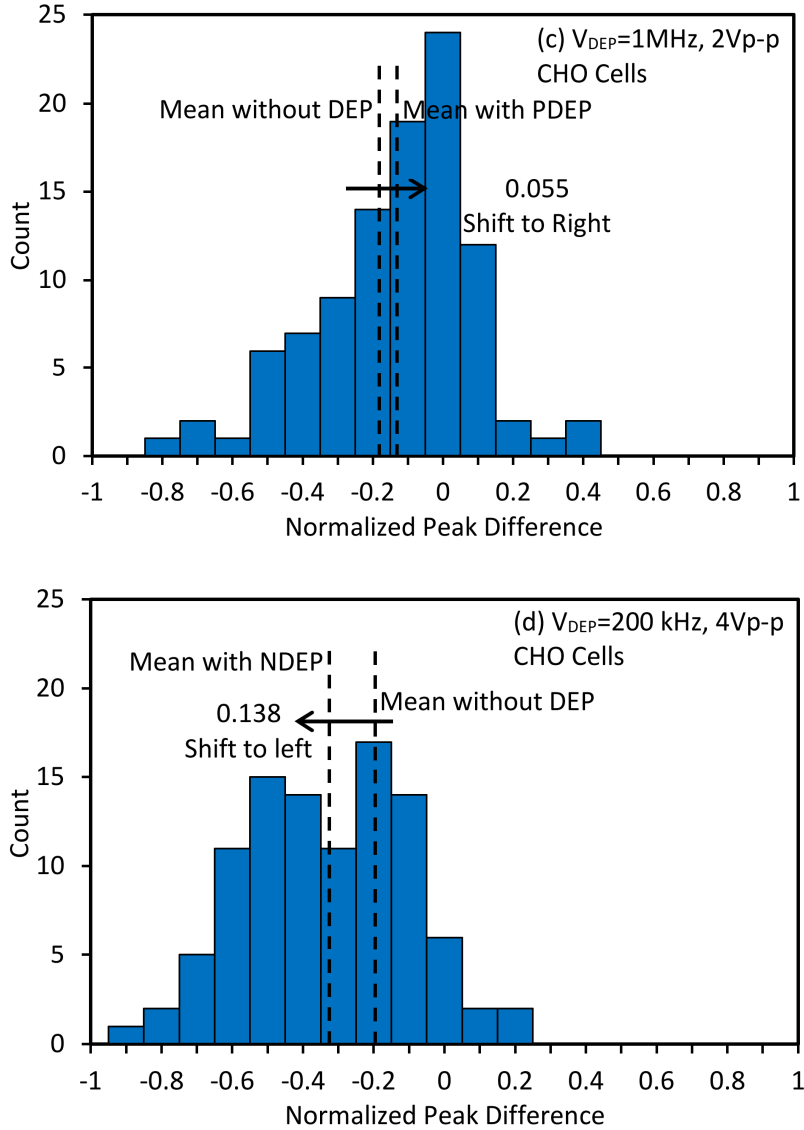


**Figure 5.6:** Normalized peak difference distribution for 100 signatures of CHO cell in low conductivity medium detected by 3-stage sensor. (a)  $V_{DEP}=0$ . (b) DEP signal is applied at 200 kHz, 2 V<sub>p-p</sub>. (c) DEP signal is applied at 1 MHz, 2 V<sub>p-p</sub>. (d) DEP signal is applied at 200 kHz, 4 V<sub>p-p</sub>.

For the data shown in Fig. 5.6 (a), no DEP signal was applied and average signatures  $P_1$  detected was 126 kHz. The mean value of signatures normalized peak difference was found -0.190 with a standard deviation of 0.184. This shows a smaller actuation when compared with the same experiment using 10  $\mu\text{m}$  PSS. This is compatible with theory as real part of Clausius-Mossotti

factor is  $\sim -0.5$  for PSS in DI water, and  $\sim -0.1$  for viable CHO cells in low conductivity medium [77, 93].

For the data shown in Figs 5.6 (b) and 5.6 (d), the VDEP, applied at 200 kHz, was 2 V<sub>p-p</sub> and 4 V<sub>p-p</sub>, respectively. This translates to an NDEP signal which is stronger in latter as DEP force scales with the square of the applied voltage on microelectrodes [30]. In Fig. 5.6(b) the average signatures P<sub>1</sub> was 142 kHz and in 5.6(d) was found 131 kHz. The results show that the mean of the normalized peak difference shifts from -0.190 when there is NODEP to -0.234 (with standard deviation  $\sim 0.220$ ) in Fig. 5.6 (b) and -0.328 (with standard deviation  $\sim 0.230$ ) in 5.6(d). This is compatible with theory. When VDEP is applied at 200 kHz, 2 V<sub>p-p</sub>, the normalized peak difference histograms mean shift to left by only -0.044, while this shift is -0.138 when the applied DEP voltage is doubled ( $F_{DEP} \propto V_{DEP}^2$ ).

For the data shown in Fig. 5.6 (c), a positive DEP was applied at 1 MHz, 1 V<sub>p-p</sub>. As the cells experience PDEP at this frequency [24] when viable, it was expected that the histograms shift to right. Given the NDEP from the detection microelectrodes, the cells do not stick to the DEP microelectrodes. Still purging of the low conductivity medium is required each  $\sim 5$  minutes when applying positive DEP. In this case the average detected signatures P<sub>1</sub> was found 147 kHz. Signatures normalized peak difference mean and standard deviation were found -0.136 and 0.222 respectively. This means that histograms in PDEP case are shifted to the right by +0.061 relative to the NODEP case. These results are consistent with theory and this sensor system demonstrates the ability to differentiate between positive and negative dielectrophoretic forces in case of biological CHO cells. To summarize, NDEP is observed for CHO cells at DEP signal frequencies of 200 kHz and PDEP is observed for DEP signal frequencies of 1 MHz.

The distribution of the histograms can be attributed to the variance in cell sizes and to the noise in the system. The uncertainty in histograms mean value (for a normal distribution) is given by  $\sigma/N$ , where  $\sigma$  is standard deviation and  $N$  number of samples. For all of the histograms shown in Fig. 5.6, is less than the observed shifts in histograms between the DEP applied and NODEP case. Also the shifts in histograms can be enhanced by applying larger DEP peak to peak voltages.

## **5.6 Conclusion**

The constraints in designing a capacitance cytometer useful for single cell applications are shown to be the ~cell size microelectrodes dimensions, microelectrodes biocompatibility, GHz operation frequency, aF capacitive sensitivity, and ~100's mV voltage on microelectrodes. Based on these design constraints, GHz frequency ring oscillators have been designed and used in a tapered oscillator structure for maximal operation frequency and sensitivity at the minimum detection voltage. This sensor was integrated as a DEP cytometer on a 4 mm<sup>2</sup> chip using a 0.35  $\mu\text{m}$  CMOS technology. It works based on detection of frequency shifts of one ring oscillator relative to another in a differential structure using an XOR gate and a frequency counter. Bare aluminium metal layers from the process were used as detection microelectrodes and microfluidic system part was used to drive cells over the top of microelectrodes. Integration of all of the required sensor components around a small die makes the design inexpensive, simple to implement, and easily reproducible. The design was used for detection of 15  $\mu\text{m}$  PSS with a 5-stage ring oscillator based sensor and 10  $\mu\text{m}$  PSS with a 3-stage ring oscillator sensor with a SNR > 10. Capacitance sensitivities of up to ~14 aF were achieved. The sensor demonstrated its use for the detection of single biological cells in a low conductivity medium.

Using the 3-stage sensor operation as a DEP cytometer was demonstrated for detection and identification of 10  $\mu\text{m}$  PSS and CHO cells. These sensors also show the ability to differentiate between three different cases of NODEP, NDEP and PDEP using the CHO cells.

The sensors designed in this work are simple to implement, and can be used for differential capacitance sensors with a high resolution for a wide range of applications. For single cell applications the SNR of the sensor still needs to be enhanced by at least one order of magnitude. So in the next chapter, system noise and sensitivity equations are presented. Then the calculated noise is compared with noise measurements in time and frequency domains. These analytical equations can be used to improve sensor SNR in future.

## Chapter 6: GHz Frequency CMOS DEP Cytometer Noise and Sensitivity Analysis

### 6.1 Abstract

System dominant source of noise is identified. Phase noise measurement results of the 3-stage and 5-stage sensors are presented. A general formula for an N stage tapered ring oscillator phase noise due to 1/f sources of noise is found, and calculations of noise using this formula is shown to be in close match with measurement results. Output jitter is estimated from phase noise spectrum and compared with sensors output noise. A general formula for the minimum detectable capacitance of the sensor architecture in this work is obtained, and design insights are given for future works.

### 6.2 Introduction

In a CMOS oscillator based reactance sensor, the dominant sources of noise are thermal and flicker noise of transistors, and the noise from power supplies [72-74, 100, 101]. These noises add (RMS values) if not correlated to make the total output noise [71]. In the phase noise spectrum, thermal white noise close to multiples of carrier frequency modulates at the carrier frequency resulting in the  $1/f^2$  part of the spectrum [72]. Flicker noise at low frequencies, modulates at carrier frequency to make the  $1/f^3$  part of the spectrum [72]. In time domain total accumulated jitter due to thermal and flicker noise from a single oscillator in a  $T_w$  time frame can be calculated by [73, 74]:

$$\sigma_{\text{Thermal}} = \kappa \sqrt{T_w} \quad (6.1)$$

$$\sigma_{\text{Flicker}} = \zeta T_w \quad (6.2)$$

In (6.1) and (6.2),  $\kappa$  and  $\zeta$  are the oscillator thermal and flicker noise jitter coefficients.

Taking all these into account, for a frequency counter averaging time of  $T_w$ , RMS output frequency noise from two oscillators in time domain can be calculated by [71]:

$$\sigma_{\frac{\Delta f}{f}}^2(T_W) = \frac{1}{T_W^2} (\sigma_{\text{Oscillator1}}^2 + \sigma_{\text{Oscillator2}}^2) = \frac{2}{T_W^2} (\sigma_{\text{Thermal}}^2 + \sigma_{\text{Flicker}}^2) \quad (6.3)$$

In which  $\sigma_{\text{Thermal}}$  and  $\sigma_{\text{Flicker}}$  are the jitter from each oscillator due to thermal and flicker noises respectively. Increasing averaging time decreases output noise ultimately to the sensor noise floor [71] equal to  $2\zeta^2$ . In fact, for averaging times beyond:

$$T_W = \left( \frac{\kappa}{\zeta} \right)^2 \quad (6.4)$$

flicker noise dominates thermal noise, and the accumulated jitter increases linearly with averaging time [102]. As shown later for the oscillators designed in this work, this averaging time is  $\sim 1\mu\text{s}$ .

### 6.3 Dominant source of noise

In the designed reactance sensors, the difference in oscillation frequency of two identical ring oscillators are detected using an XOR gate and a low pass filter. This difference frequency is then measured by a frequency counter. Each sensor components can add noise to the output frequency.

Sensor noise diagram is shown in Fig. 6.1.

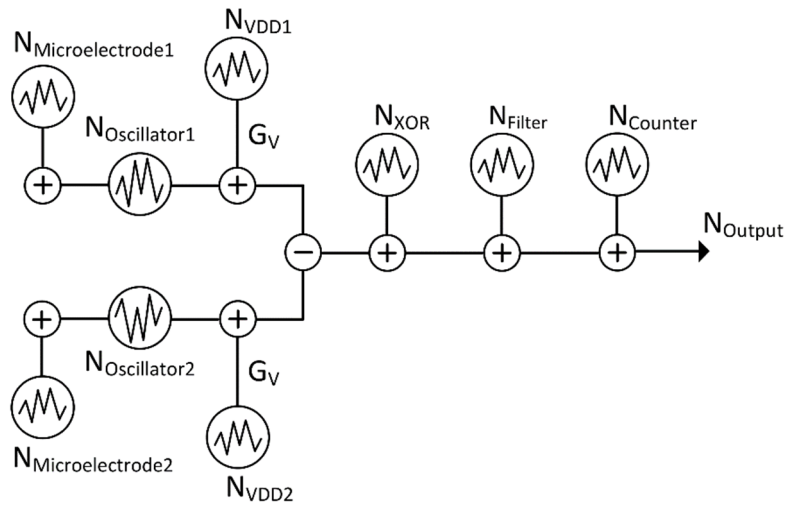


**Figure 6.1:** Sensor noise diagram.

Ring oscillators detection microelectrodes are sensitive to differential changes in capacitance and can add frequency noise in case of differential perturbations. Microelectrodes are 180  $\mu\text{m}$  apart on the same die. Common sources of noise such as mechanical vibrations, thermal drift and noise from optical interferences can be removed after frequency comparison in the XOR gate, as long as these sources induce the same perturbation on microelectrodes in the differential pair. The dominant sources of noise induced by ring oscillators are thermal noise and flicker noise [72-74, 100, 101]. The uncorrelated thermal noise from ring oscillators transistors and noise from non-stationary processes such as 1/f noise of transistors directly add (RMS values) after the XOR gate [71]. In this design simple inverters are used in the oscillators architecture. So the noise from separate power supplies used for tuning, directly couple to the output with a gain of  $G_V$  (equal to  $\partial f_{\text{osc}}/\partial V_{\text{DD}}$ ). This gain was measured to be 0.175 MHz/mV for the 5-stage oscillator and 0.787 MHz/mV for the 3-stage oscillator at difference frequency of 20 MHz. Therefore, DC supply voltage noise can induce a significant frequency noise in the output. Hence in this work a 16 bits DAC (LTC2607, Linear Technology) is used with output voltage noise of  $\sim 15 \mu\text{V}_{\text{p-p}}$ . This is proportional to 2.6 kHz and 11.8 kHz peak to peak noise in the output of 5-stage and 3-stage oscillators respectively. Supply noise is not the dominant source of noise as the measured RMS output noise values are  $\sim 5$  kHz in the output of 5-stage sensor and  $\sim 12$  kHz in the output of 3-stage sensor. To confirm that supply noise is not dominant in this design, a noise measurement is done by replacing the 16 bits DAC with a heavily filtered (200  $\mu\text{F}$  capacitor) 3.3 V battery. The results are shown in Table. 6.1.

**Table 6.1:** 3-stage sensor measured noise with different supplies.

	DAC	Battery
RMS Output Frequency Noise	10.5 kHz	8.0 kHz

In this measurement, 3-stage sensor oscillators and XOR gate are supplied all with one battery. Enough voltage difference is induced using series potentiometers to tune the output frequency difference to be 20 MHz. It is obvious that the supply noise is no the dominant source of output noise. In fact:

$$N_{\text{Output}} = \sqrt{G_V^2(N_{\text{VDD1}}^2 + N_{\text{VDD2}}^2) + N_{\text{other}}^2} \quad (6.5)$$

In this equation  $N_{\text{other}}$  represents the noise from other sources rather than supply. Using this equation and the measured values in Table 6.1, and assuming that batteries are noiseless, total DAC noise contribution to output noise is calculated ~ 6.8 kHz rms.

The noise from digital phase detectors and mixers are usually neglected especially in PLL designs as it does not significantly contribute in the total output noise [103, 104]. Also the frequency counter (53132A, Agilent) has a maximum of 2.5 ppm frequency error at 20 MHz when averaging time is set between 1 ms to 100 ms. Therefore, the noise from the last three blocks in Fig. 6.1 are neglected.

To show that the dominant source of noise in this work is the flicker noise of the oscillators, 3-stage sensor output frequency noise is measured for three different averaging times of 100 ms, 10 ms and 1 ms when 16 bits DAC is used as supply. The results are shown in Table 6.2.

**Table 6.2:** 3-stage sensor frequency noise for different averaging time lengths.

Averaging Time	100 ms	10 ms	1 ms
RMS Frequency Noise	10.1 kHz	11.5 kHz	14.4 kHz

According to these results, increasing noise bandwidth by a factor of 100, will increase the noise only by a factor of less than 2. This matches with theory based on equations (6.2) and (6.3), that for large averaging times sensor is at its noise floor and flicker noise is dominant. This means that cytometer sampling rate can be increased by a factor of 100 when sacrificing sensitivity by a factor of less than 2.

## 6.4 Calculation of phase noise due to 1/f noise

The ring oscillators designed in this work are mainly composed of multiples of a simple unit inverter cell with  $(W/L)_n=(2.4 \mu\text{m}/0.35 \mu\text{m})$  and  $(W/L)_p=(3.8 \mu\text{m}/0.35 \mu\text{m})$ . The 3-stage oscillator has 12, 36, and 108 unit cells in its first, second and third stage and the 5-stage oscillator has 1, 3, 9, 27, and 81 unit cells in its first to fifth stage. A general N stage ring oscillator which has  $N_1, N_2, \dots, N_n$  unit inverters in its 1<sup>st</sup> to n<sup>th</sup> stage is shown in Fig. 6.2.

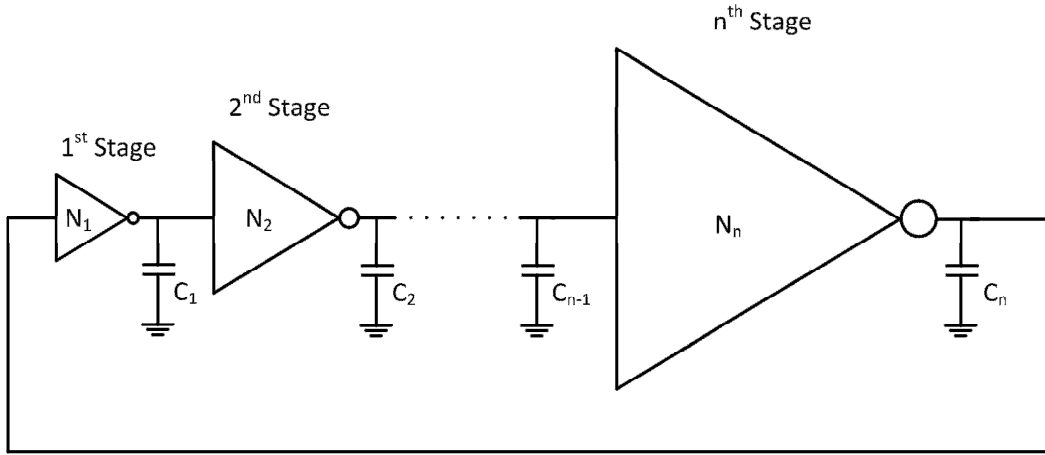


**Figure 6.2:** A general n stage ring oscillator with  $N_i$  unit inverter cells in its  $i^{\text{th}}$  stage.

Phase noise from transistors 1/f noise sources is calculated using ring oscillator time domain noise calculations from McNeill [74] and Abidi [100] for this general oscillator. If  $I_{NK}$  and  $I_{PK}$  are the saturation current of NMOS and PMOS devices in the  $k^{\text{th}}$  stage, oscillation period can be estimated by [4]:

$$T_{\text{osc}} = \frac{V_{\text{DD}}}{2} \sum_{k=1}^n C_k \left( \frac{1}{I_{\text{NK}}} + \frac{1}{I_{\text{PK}}} \right) \quad (6.6)$$

If NMOS and PMOS devices at each stage, make a symmetric inverter, which is the case in this design, oscillation frequency will be:

$$f_{\text{osc}} = \frac{1}{V_{\text{DD}}} \left( \sum_{k=1}^n \frac{C_k}{I_{\text{NK}}} \right)^{-1} \quad (6.7)$$

And:

$$\frac{\partial f_{\text{osc}}}{\partial I_{\text{NK}}} = \frac{1}{V_{\text{DD}}} \left( \sum_{k=1}^n \frac{C_k}{N_k} \right)^{-2} \frac{C_k}{N_k^2} \quad (6.8)$$

In (6.8),  $N_k$  is the number of inverters used in the  $k^{\text{th}}$  stage in tapered oscillator structure. So phase noise due to flicker noise can be calculated by:

$$\begin{aligned} \mathcal{L}(f) &= \frac{1}{4f^2} \sum_{k=1}^n \left( S_{\text{NK}}^{1/f} + S_{\text{PK}}^{1/f} \right) \left( \frac{\partial f_{\text{osc}}}{\partial I_{\text{NK}}} \right)^2 \\ &= \frac{1}{4f^2} \sum_{k=1}^n \left( \frac{\partial f_{\text{osc}}}{\partial I_{\text{NK}}} \right)^2 \left( \frac{K_{\text{FN}}}{N_k W_n \text{LC}_{\text{OX}} f} (g_{\text{d0}}^{\text{NK}})^2 + \frac{K_{\text{FP}}}{N_k W_p \text{LC}_{\text{OX}} f} (g_{\text{d0}}^{\text{PK}})^2 \right) \end{aligned} \quad (6.9)$$

In (6.9)  $S_{\text{NK}}^{1/f}$  and  $S_{\text{PK}}^{1/f}$  are flicker noise spectrum from NMOS and PMOS devices in the  $k^{\text{th}}$  stage.  $g_{\text{d0}}$  is zero bias drain source conductance.  $W_n$  is NMOS width, and  $W_p$  is PMOS width of the unit inverter cell used for making tapered oscillator stages.  $K_{\text{FN}}$  and  $K_{\text{FP}}$  are flicker noise coefficients for an NMOS and a PMOS device respectively.

$$\begin{aligned} \mathcal{L}(f) &= \frac{1}{4f^2} \sum_{k=1}^n \left( \frac{1}{V_{\text{DD}}} \left( \sum_{j=1}^n \frac{C_j}{N_j} \right)^{-2} \frac{C_k}{N_k^2} \right)^2 \times \\ &\left( \frac{K_{\text{FN}}}{N_k W_n \text{LC}_{\text{OX}} f} \left( \mu_n C_{\text{OX}} \frac{N_k W_n}{L} \left( \frac{V_{\text{DD}}}{2} - V_{\text{T,N}} \right) \right)^2 + \frac{K_{\text{FP}}}{N_k W_p \text{LC}_{\text{OX}} f} \left( \mu_p C_{\text{OX}} \frac{N_k W_p}{L} \left( \frac{V_{\text{DD}}}{2} - V_{\text{T,P}} \right) \right)^2 \right) \end{aligned} \quad (6.10)$$

Assuming  $V_{\text{T,N}} = V_{\text{T,P}} = V_{\text{th}}$ ,

$$\mathcal{L}(f) = \frac{1}{4f^3} \left( K_{\text{FN}} \mu_n^2 W_n + K_{\text{FP}} \mu_p^2 W_p \right) \frac{C_{\text{OX}}}{L^3} \left( \frac{V_{\text{DD}} - V_{\text{th}}}{2 V_{\text{DD}}} \right)^2 \frac{\sum_{k=1}^n \frac{C_k^2}{N_k^3}}{\left( \sum_{k=1}^n \frac{C_k}{N_k} \right)^4} \quad (6.11)$$

These equations are used to calculate phase noise spectrum of the 3-stage and 5-stage oscillators. Process parameters are obtained from BSIM3 v3.1 TSMC 0.35 $\mu$ m CMOS technology model file [105], and are shown in Table 6.3. For simplicity,  $V_{T,N}=V_{T,P}=V_{th}=0.7$  V.

**Table 6.3:** Parameters values used in noise equations [105 ,106].

$\mu_n=0.049$ m <sup>2</sup> /V.S	$V_{th} = 0.7$ V	$K_{FN} = 1.32 \times 10^{-25}$ V <sup>2</sup> .F
$\mu_p=0.0158$ cm <sup>2</sup> /V.S	$t_{ox}=7.7 \times 10^{-9}$ F/m <sup>2</sup>	$K_{FP} = 5.88 \times 10^{-25}$ V <sup>2</sup> .F

Calculation of parasitic capacitance at each node is done based on extraction of input and output capacitance of the single unit cell inverter in Cadence (IC 5.1) using TSMC 0.35 $\mu$ m CMOS 2P4M polycide process design kit. In this case, input and output capacitances are found 2.45 fF and 0.6 fF respectively. Based on the number of unit cells used at each stage of oscillators, parasitic capacitances at the nodes of 3-stage and 5-stage oscillators are calculated and shown in Table 6.4. In this case a 500 fF microelectrode load capacitance is assumed to be in the output of the first stage in 3-stage oscillator and in the output of the second stage in 5-stage oscillator.

**Table 6.4:** Parasitic capacitances at different nodes of 3-stage and 5-stage oscillator.

	C <sub>1</sub>	C <sub>2</sub>	C <sub>3</sub>	C <sub>4</sub>	C <sub>5</sub>
3-Stage Oscillator	595.4 fF	286.2 fF	94.2 fF	-	-
5-Stage Oscillator	7.9 fF	523.8 fF	71.5 fF	214.6 fF	51.0 fF

Using (6.11), and the parameters values in Table 6.3 and Table 6.4, phase noise of oscillators are calculated.

$$\mathcal{L}_{3\text{-Stage}}(f) = \frac{1.12 \times 10^7}{f^3} \quad (6.12)$$

$$\mathcal{L}_{5\text{-Stage}}(f) = \frac{4.13 \times 10^6}{f^3} \quad (6.13)$$

## 6.5 Phase noise measurement results

Phase noise of 3-stage and 5-stage ring oscillators are measured by probing their microelectrodes using a high impedance probe (Model 34A, GGB), and a phase noise measurement personality (Agilent E4448A PSA). In this case, one oscillator from a pair of two in the 3-stage sensor and 5-stage sensor are supplied at 3 V using 16 bits DAC. Also the sensors 20 MHz output IF signal phase noise is measured by buffering the output signal (LT1220, Linear Technology and SRS445A, Stanford Research Systems Inc.) before applying it to phase noise measurement tool. For this measurement both oscillators of sensors were supplied with 16 bits DAC at 3 V, with enough voltage difference to tune output frequency at 20 MHz. Fig. 6.3 shows measurement results for the 3-stage sensor and Fig. 6.4 shows measurement results for the 5-stage sensor.

Thermal noise and flicker noise from oscillators modulate at carrier frequency with slopes of -20 dB/dec and -30 dB/dec [72-74]. Comparing output noise with the noise from a single oscillator shows that uncorrelated white noise sources and non-stationary  $1/f$  noise add in the output of phase detector. In fact, differential architecture of this sensor cannot help reducing the effect of the mentioned sources of noise.

## 6.6 Jitter calculation from measured phase noise spectrum

Measured phase noise spectrum of oscillators are curve fitted by two lines with slopes of -20 dB/dec and -30 dB/dec. By doing this phase noise coefficients of 3-stage oscillator are found 30.5 Hz and  $1.29 \times 10^7 \text{ Hz}^2$  for thermal and flicker noise respectively. As shown in Fig. 6.3 flicker noise trend line is closed to the calculated phase noise using equation (6.11). For 5-stage oscillator thermal and flicker phase noise coefficients are found 4.6 Hz and  $2.5 \times 10^6 \text{ Hz}^2$ .

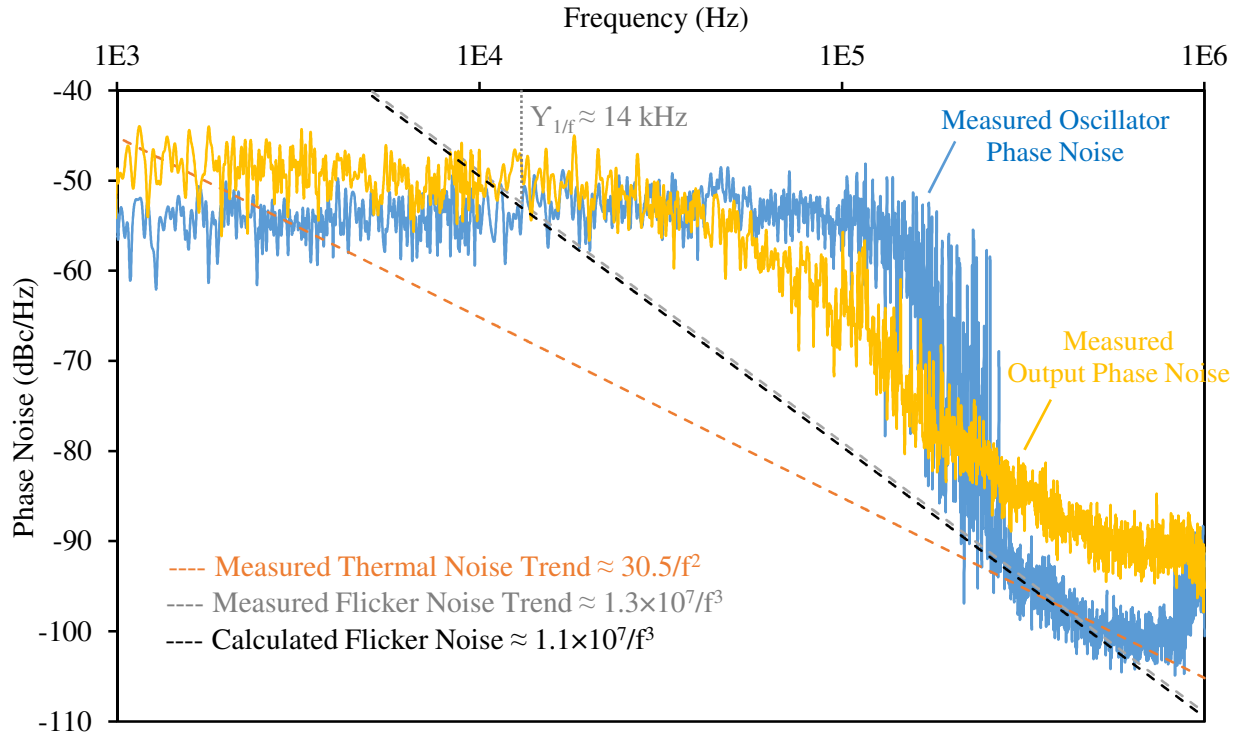


**Figure 6.3:** 3-stage sensor output and 3-stage ring oscillator measured phase noise spectrums.

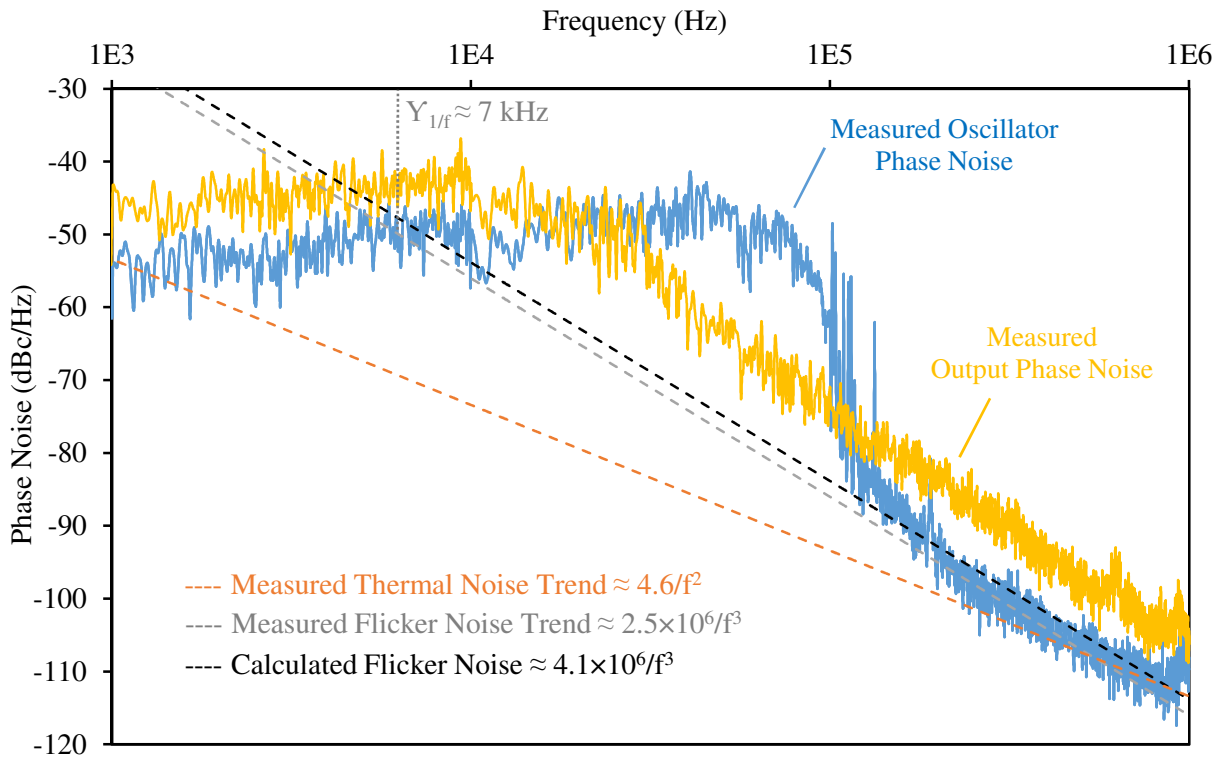


**Figure 6.4:** 5-stage sensor output and 5-stage ring oscillator measured phase noise spectrums.

The difference between calculated and measured phase noise of 5-stage oscillator can be related to the parasitic capacitances due to interconnects in the 5-stage oscillator as it has more and larger interconnects than 3-stage oscillator. It can also be due to process parameters variation.

Calculations from McNeill [102] is used to theoretically relate measured phase noise data to jitter in time domain. Thermal and flicker noise jitter coefficients can be calculated by:

$$\kappa = \frac{\sqrt{C_{\text{Thermal}}}}{f_{\text{osc}}} \quad (6.14)$$

$$\zeta = \alpha \frac{\sqrt{C_{\text{Flicker}}}}{f_{\text{osc}}} \quad (6.15)$$

In these equations  $C_{\text{Thermal}}$  and  $C_{\text{Flicker}}$  are phase noise coefficients of thermal and flicker noises respectively.  $\alpha$  is a constant which obtains its value based on flicker noise cut off frequency  $Y_{1/f}$ , and is about 2 when  $2\pi Y_{1/f} \Delta T_w \gg 1$ . The averaging time used in this work was 100 ms. Assuming that this large averaging time reduce jitter to down to noise floor, output jitter of 3-stage sensor can be calculated as follows [102]:

$$\kappa_{3\text{-Stage}} = \frac{\sqrt{30.5}}{1.4 \text{ GHz}} = 3.94 \times 10^{-9} \sqrt{\text{Sec}} \quad (6.16)$$

$$\zeta_{3\text{-Stage}} = 2 \times \frac{\sqrt{1.26 \times 10^7}}{1.4 \text{ GHz}} = 5.07 \times 10^{-6} \quad (6.17)$$

$$\sigma_{\frac{\Delta f}{f}} = \sqrt{2} \zeta_{3\text{-Stage}} = 7.17 \text{ ppm} \quad (6.18)$$

$$N_{\text{Output}} = \sigma_{\frac{\Delta f}{f}} \times f_{\text{osc}} = (7.17 \times 10^{-6}) \times 1.4 \text{ GHz} = 10.04 \text{ kHz RMS} \quad (6.19)$$

For 5-stage sensor:

$$\kappa_{5\text{-Stage}} = \frac{\sqrt{4.6}}{0.5 \text{ GHz}} = 4.28 \times 10^{-9} \sqrt{\text{Sec}} \quad (6.20)$$

$$\zeta_{5\text{-Stage}} = 2 \times \frac{\sqrt{2.50 \times 10^6}}{0.5 \text{ GHz}} = 6.32 \times 10^{-6} \quad (6.21)$$

$$\sigma_{\frac{\Delta f}{f}} = \sqrt{2}\zeta_{5\text{-Stage}} = 8.94\text{ppm} \quad (6.22)$$

$$N_{\text{Output}} = \sigma_{\frac{\Delta f}{f}} \times f_{\text{osc}} = (8.94 \times 10^{-6}) \times 0.5 \text{ GHz} = 4.47 \text{ kHz RMS} \quad (6.23)$$

The summary of these calculations compared with measured noise values are shown in Table 6.5 A and B for 3-stage and 5-stage sensors.

**Table 6.5:** Calculated vs. measured noise parameters.

A. 3-Stage Sensor

	Phase Noise		Jitter		
	C <sub>Flicker</sub> (Hz <sup>2</sup> )	C <sub>Thermal</sub> (Hz)	K (Sec <sup>1/2</sup> )	ζ	N <sub>Output</sub> (kHz)
Calculated	1.1×10 <sup>7</sup>	-	-	4.66×10 <sup>-6</sup>	10 kHz
Measured	1.3×10 <sup>7</sup>	30.5	3.94×10 <sup>-9</sup>	5.07×10 <sup>-6</sup>	12 kHz

B. 5-Stage Sensor

	Phase Noise		Jitter		
	C <sub>Flicker</sub> (Hz <sup>2</sup> )	C <sub>Thermal</sub> (Hz)	K (Sec <sup>1/2</sup> )	ζ	N <sub>Output</sub> (kHz)
Calculated	4.1×10 <sup>6</sup>	-	-	8.09×10 <sup>-6</sup>	4.5 kHz
Measured	2.5×10 <sup>6</sup>	4.6	4.28×10 <sup>-9</sup>	6.32×10 <sup>-6</sup>	5 kHz

### 6.7 Suggestions on how to improve the design SNR

The minimum sensitivity achieved in the designed cytometer was ~14 aF. Increasing capacitance sensitivity or reducing noise can help enhancing minimum detectable capacitance. For “n” stage tapered ring oscillator, assuming microelectrodes are located at stage “i”, and C<sub>i</sub>/N<sub>i</sub> >> C<sub>k</sub>/N<sub>k</sub> for 1≤k≤n (k≠i), and C<sub>i</sub>=C<sub>Microelectrode</sub>+C<sub>parasitic,i</sub>, phase noise can be estimated by:

$$\mathcal{L}(f) \approx \frac{1}{16f^3} \left( K_{\text{FN}} \mu_n^2 W_n + K_{\text{FP}} \mu_p^2 W_p \right) \frac{C_{\text{OX}}}{L^3} \frac{N_i}{\left( C_{\text{Microelectrode}} + C_{\text{parasitic,i}} \right)^2} \quad (6.24)$$

So:

$$N_{\text{Output}} = \sigma_{\frac{\Delta f}{f}} \times f_{\text{osc}} = \sqrt{2}\zeta \times f_{\text{osc}} = 2\sqrt{2C_{\text{Flicker}}}$$

$$= \frac{\sqrt{2}}{2} \left( \left( K_{FN} \mu_n^2 W_n + K_{FP} \mu_p^2 W_p \right) \frac{C_{OX}}{L^3} \right)^{1/2} \frac{N_i^{1/2}}{\left( C_{Microelectrode} + C_{parasitic,i} \right)} \quad (6.25)$$

Sensitivity to capacitance changes can be calculated using (6.7):

$$S_{Capacitance} = \frac{\partial f_{osc}}{\partial C_i} = f_{osc} \frac{1}{N_k} \left( \sum_{k=1}^n \frac{C_k}{N_k} \right)^{-1} \approx \frac{f_{osc}}{C_i} = \frac{f_{osc}}{C_{Microelectrode} + C_{Parasitic,i}} \quad (6.26)$$

So minimum detectable capacitance (MDC) can be estimated by:

$$MDC = \frac{N_{Out}}{S_{Capacitance}} = \frac{\frac{\sqrt{2}}{2} \left( \left( K_{FN} \mu_n^2 W_n + K_{FP} \mu_p^2 W_p \right) \frac{C_{OX}}{L^3} \right)^{1/2} N_i^{1/2}}{f_{osc}} \quad (6.27)$$

If  $f_{osc}$  is kept constant to meet design requirements, there is not much room for design parameters to enhance MDC by 1-2 orders of magnitude using a CMOS process and the designed architecture.

Doubling “L” can help reducing MDC by a factor of 2, but to keep  $f_{osc}$  constant,  $W_n$  and  $W_p$  should be increasing with the same ratio, resulting in chip area to increase by a factor of 4.

To reduce flicker noise signal chopping can be used. Also differential ring oscillators are less susceptible to supply noise variations but they suffer from worst flicker noise performance [73, 100]. The use of other transistors types such as JFETs can also help reducing minimum detectable capacitance [107].

## 6.8 Conclusion

The dominant source of sensor noise is identified to be the flicker noise from oscillators transistors. It is shown that for ~ms averaging time of the frequency counter, noise is constant and close to its noise floor. Calculated RMS noise prove to be close to measured results. The general formula obtained for the minimum detectable capacitance shows that for a constant die area, this parameter is mainly dependent on process parameters. Reducing noise by one order of magnitude will make

the noise from the power supply dominant, unless other architectures for inverters are used that make the oscillator power supply rejection ratio higher.

In the next chapter, the works done in this thesis is reviewed, and based on the results obtained in this chapter, more suggestions on improving the design will be given.

## **Chapter 7: Conclusions and Future Work**

### **7.1 Overview of the Accomplished Works**

This research was organized toward developing a completely electronic integrated sensor for analyzing single biological cells. While fully electrical sensors in this application are typically markerless compared with chemical-optical techniques, they have the capability of being integrated. Integration makes these sensors low cost, small in size, portable and easily reproducible.

In chapter 1, a complete literature review of different electrical techniques for characterization of single cells are given. DEP and impedance spectroscopy are shown to be faster compared with Electrorotation. These techniques in conjunction with cytometry, makes the sensor analysis rate faster. A brief review of a previously designed resonator based DEP-Cytometer is done including the disadvantages of that sensor [10]. The main motivation of the works done during this research was specified to be shrinking down the size of the sensor. This lead to totally different designs than the initial sensor, which was introduced in the next chapters.

In chapter 2, a review on requirements for designing a sensor for single cell applications is given. The most important constraint being operation frequency, leads to detection of permittivity of the subject under test, or the capacitance. A detailed review of different high resolution capacitance detection techniques shows that most of them have been developed to operate at kHz-MHz range which is not proper for detection of single biological cells. A review of the previously designed GHz frequency DEP-Cytometer is done first. This apparatus has proved to be useful in monitoring single cells apoptosis process. This sensor is shown to meet all the required constraints for a single cell analysis sensor. But the sensor is bulky, expensive and hardly portable as it uses an RF signal generator and a lock-in amplifier. Also tuning the sensor is hard and follows two steps of setting

the RF frequency at resonance frequency of the sensor and nulling the output by a phase tuning phase shifter. So the design of a GHz frequency reflectometer is introduced [25]. It is shown that the sensor meets all the constraints for detection of single cells. The sensor operates at 1.86 GHz and achieves 1.25 aF capacitance sensitivity with only -16dbm power level on its microelectrodes. The sensor is integrated on PCB but still makes use of a lock-in amplifier, and RF generator and a separate microfluidic chip to be complete DEP-Cytometer system.

In chapter 3, ring oscillator based capacitance sensor is introduced as an approach which all its components can be integrated on chip [26]. This sensor is implemented on PCB for operation proof of concept. This sensor is used in detection of water IPA contents from 100%-1%, and 15  $\mu\text{m}$  PSS. The sensor does not achieve enough sensitivity for single biological cells detection, because the inverters used in that sensor are designed with output buffers to be able to drive  $\sim 5$  pF capacitance load. But the sensor has the capability of being integrated completely on chip. The sensor also uses supply voltage levels at detection frequency, which for single cell applications result in actuation. In chapter 4 and chapter 5, a comprehensive review of constraints for designing an integrated sensor for DEP-Cytometry is give. These include sensor GHz operation frequency, low voltage on detection microelectrodes,  $\sim$ aF capacitance sensitivity, bandwidth, and selection of proper integration technology.

Based on these constraints the previously designed differential ring oscillator based sensor is integrated on chip using 0.35  $\mu\text{m}$  CMOS technology [28]. Application specific ring oscillators are designed to meet the requirements for an integrated capacitance sensor for single cell applications. The design is shown to have a sensitivity of 14 aF with 1.6 V detection voltage on microelectrodes in 10 Hz bandwidth. The main source of noise is shown to be flicker, which only increases by a factor of less than two with a 100 times decrease in averaging time length. So the sensor bandwidth

can easily be increased for faster detection by sacrificing SNR with a factor of less than two. The integrated sensor is used as a DEP-Cytometer for detection of single CHO cells in presence of positive and negative DEP force. Analysis of signatures from 100 CHO cells show that the histograms shift to right by 0.055 by applying a 1 MHz, 1 V<sub>p-p</sub> PDEP signal, while shifting to left by 0.138 while applying NDEP at 200 kHz, 4 V<sub>p-p</sub>.

In chapter 6, a detail explanation of different sources of noise in the designed sensor are presented. This completes with analytical equations that estimates the dominant noise in the system. The equation for the minimum sensitivity of the system obtained in this chapter gives insight to those who want to pursue working on this design in future.

## **7.2 Comparison with Capacitance Sensors in Other Works**

Three different capacitance sensors were designed and introduced in chapters 2-4. These capacitance sensors were optimized for single cell detection and analysis in a DEP cytometer. As mentioned in chapter 5, GHz detection frequency, ~aF capacitance sensitivity, minimum voltage on microelectrodes, bandwidth, cost and size has been the main design constraints. The design in chapter 3 was mainly implemented to prove the concept of ring oscillator based capacitance detection technique, before implementing the design on chip. The main advantage of the designs in chapter 3-5 is that all of the components in the designs are integratable on chip. The main advantage of the design in chapter 5, compared with other capacitance sensors implemented on chip, is that the design has high density integration capability.

The summary of the designs specifications in this work compared with the capacitance sensors from other research groups -mentioned in introduction of chapters 2 and 5- can be found in Table I.

**Table 7.1:** Comparison of the sensors developed by different groups for high sensitivity capacitance detection.

Developed in	Technique used	Resolution	Bandwidth	Operational Frequency	Parasitic Capacitances	Applied Voltage	Implementation of Electronics
[108]	CBCM	10 aF	-	0.6 MHz-5 MHz	-	2 V	1 $\mu\text{m}$ CMOS, Area= 2.25 $\mu\text{m}^2$
[31]	CBCM	16 aF	-	50 kHz-200 kHz	-	5 V	0.8 $\mu\text{m}$ CMOS Technology
[109]	CBCM	15 aF	-	1 kHz	~100 fF	3 V	0.5 $\mu\text{m}$ CMOS Technology
[110]	CBCM	1 aF	100Hz	100 kHz	-	20 V	PCB
[51]	CBCM	12 zF	-	15 kHz	-	1.5 V	BiCMOS, Area= 0.64 $\text{mm}^2$
[111]	CBCM	10 aF	-	10 kHz- 1 MHz	~175 fF	1.8 V	0.18 $\mu\text{m}$ CMOS
[112]	Balanced bridges	0.5 aF	-	1 kHz	-	250 mV	Commercial Capacitance Bridge
[113]	Balanced bridges	24 aF	10KHz	1 MHz	~440 fF	3 V	1.5 $\mu\text{m}$ CMOS Technology
[35]	Oscillator based	50 aF	-	10 kHz	~50 pF	5 V	0.7 $\mu\text{m}$ CMOS Technology
[36]	Current front end	5 zF	1.6Hz	DC-1 MHz	~1 pF	6 V	0.35 $\mu\text{m}$ CMOS, Area= 0.6 $\text{mm}^2$
[37]	Resonance based	100 aF	-	2 MHz	~8 pF	1 V	PCB
[10]	Resonance based	0.65 aF	50Hz	1.8 GHz	~250 fF	300 mV	Connectorized Components
[95]	Resonance based	0.32 aF	160 kHz	6.5 GHz	~29 fF	1 V	65 nm CMOS, Area= 0.18 $\text{mm}^2$
Chapter 2 [25]	Reflectometer	1.25 aF	50 Hz	1.86 GHz	~ 1 pF	70 mV	PCB
Chapter 3 [26]	Ring oscillator based	180 aF	10 Hz	240 MHz	~ 1 pF	2.5 V	PCB
Chapter 4-5 [28]	Ring oscillator based	14 aF	10 Hz	1.4 GHz	500 fF	1.42 V	0.35 $\mu\text{m}$ CMOS, area= 0.6 $\text{mm}^2$

### 7.3 Suggestions and Future Works

Based on what was discussed in the past chapters, the designed integrated DEP cytometer sensor can be improved mainly in the following ways:

1- The sensitivity of the sensor achieves 14 aF. The capacitance of a single cell is about 50-200 aF. In case of CHO cell samples under the onset of PDEP, the normalized peak difference histograms only move ~25%. Hence for SNR~10, cells altitude change detection can be affected by system noise. Compared with resonator based sensor with a sensitivity of 0.65 aF, the sensor SNR still need to be increased by at least a factor 10-20 to be comparable with the original design. Increasing the sensor sensitivity is necessary to be able to drive cells at higher altitudes in the channel and higher velocities.

2- Sensor noise can be decreased by making all stages of the ring oscillators identical. The sensor is designed to use tapered ring oscillators, to be able to probe it off-chip and to be able to drive external microfluidic electrodes. It is shown that identical stages result in lower phase noise and hence less frequency noise in time domain [73].

3- The sensor is cheap so it can be used as a disposable sensor. If it is going to be used as a permanent system, it is better not to passivate the microelectrodes to be able to use the sensor for long term measurements. This will decrease sensor sensitivity and hence an increase in SNR is required beforehand. Also the temporary Plexiglas microfluidic part can be replaced with a permanent PDMS mold made microfluidic. The Plexiglas microfluidic part used in this work is attached to the chip by the screwing it to the board which chip is soldered on. This causes the microfluidic Plexiglas piece to deform slightly where it is attached to silicon surface and hence be useful for one time mounting.

4- The buffer amplifier and frequency counter used in this work are off-chip. It can simply be integrated on chip. In case of using on-chip counters, the noise from period variations of that counter should be taken into account as a part of system noise. This noise is negligible in this work because the related noise from the used frequency counter is less than 2.5 ppm [71].

5- The main source of noise is shown to be flicker noise of the MOSFETs. This noise arises mainly from trapping charge carriers in the dangling bonds of Si-SiO<sub>2</sub> gate interface [114]. To reduce the noise, a different process can be used with devices with less flicker noise such as a JFETs. In JFETS, charge transfer is accomplished in bulk silicon so flicker noise is smaller. The other solution is to use a single ring oscillator rather than the differential structure that cause the noise to reduce by a factor of  $\sqrt{2}$ .

6- An important aspect of the capacitance sensor that can be improved is the detection voltages on microelectrodes, which in the current 3-stage sensor is 1.4 V p-p. This voltage should be decreased below 300 mV for the used microelectrodes dimensions to prevent cells and particles from being actuated by the detection microelectrodes. Otherwise the effect of this actuation should be de-embedded from the actuation by DEP microelectrode.

These improvements will make the designed DEP cytometer an ideal tool for analysis of single cells. This MEMS device will meet all the specifications required by a capacitance cytometer, and can replace the conventional bulky and expensive impedance based cytometers available on the market. Some of the current and potential applications of this sensor can be as follows:

1- This MEMS device can be used as a cytometer in monitoring apoptosis, and cells viability. If the sensor is designed with the mentioned SNR, it can be used with CHO cell samples. As a DEP cytometer, dyes [115] rather than Trypan blue can be used to monitor apoptosis with the sensor. The chip can also be used for analysis of larger cells and the dimensions of the microfluidic channel

can be adjusted accordingly. Some examples are monitoring apoptosis of pollen cells and the confluency of microcarriers [116].

2- The signatures amplitude obtained by the sensor will mainly depend on cells volume and permittivity. So it can be used for cell counting and sizing. It can also be used for analysis of cells internal composition based on the relationship between cell contents and its cytoplasmic dielectric constant.

3- The current microelectrodes can be replaced by an array of arbitrary microelectrodes configuration that suit other applications such as trapping/analyzing single cells. Oscillators detection frequency can be made variable for example by a capacitor bank on chip in the current design or by implementing variable frequency oscillators. Hence multi frequency electrical analysis of cells can be done on chip. This can make analysis of cells in  $\alpha$  and  $\beta$  dispersion possible for applications such as detection of DNA contents of cells [112].

4- The total size of the detection system on CMOS chip is  $\sim 0.6 \text{ mm}^2$ . So in about  $1 \text{ cm}^2$  more than 150 of these sensors can be integrated together to capture single cell permittivity spectrum in a wide frequency range. Parallelizing these sensors increases analysis throughput in this case.

## References

- [1] Cell and Molecular Biology Concepts and Experiments, G. Karp, John Wiley and Sons Inc., 2010.
- [2] Guava easyCyte Systems, EMD Millipore, 2015.
- [3] Attune NxT Acoustic Focusing Cytometer, Invitrogen, 2015.
- [4] Trypan blue dye enters viable cells incubated with the pore-forming toxin HlyII of *Bacillus cereus*, S. L. Tran, A. Puhar, M. Ngo-Camus, N. Ramarao, Plos One, vol.6, no.9, 2011.
- [5] Guava ViaCount Assay Datasheet, EMD Millipore, 2008.
- [6] Characterization of Biological Cells by Dielectric Spectroscopy, K. Asami, Non-Crystalline Solids, vol.305, no.1, 2002.
- [7] AmphaZ30, Amphasys AG, 2012.
- [8] Amphasys, retrieved from <http://www.amphasys.com/impedance-flow-cytometry#Chips>.
- [9] Microwave Frequency Sensor for Detection of Biological Cells in Microfluidic Channels, M. Nikolic-Jaric, S. F. Romanuik, G. A. Ferrier, G. E. Bridges, M. Butler, K. Sunley, D. J. Thomson, M. R. Freeman, BioMicrofluidics, vol.3, no.3, 2009.
- [10] A Microwave Interferometric System for Simultaneous Actuation and Detection of Single Biological Cells, G. A. Ferrier, S. F. Romanuik, D. J. Thomson, G. E. Bridges, M. R. Freeman, Lab on A Chip, vol.9, no.23, 2009.
- [11] Single-Cell Bioelectrical Impedance Platform for Monitoring Cellular Response to Drug Treatment, F. Asphahani, K. Wang, M. Thein, O. Veiseh, S. Yung, J. Xu and M. Zhang, Physical Biology, vol.8, no.1, 2011.
- [12] Assessment of Multidrug Resistance Reversal using Dielectrophoresis and Flow Cytometry, F. H. Labeed, M. H. Coley, H. Thomas, M. P. Hughes, Biophysical journal, vol.85, no.3, 2028-2034, 2003.
- [13] Isolation of Rare Cells from Cell Mixtures by Dielectrophoresis, P. Gascoyne, J. Noshari, T. Anderson, F. Becker, Electrophoresis, vol.30, no.8, 2009.
- [14] Dielectrophoretic Separation of Mouse Melanoma Clones, A. C. Sabuncu, J. A. Liu, S. J. Beebe, A. Beskok, Biomicrofluidics, vol.4, no.2, 2010.
- [15] Rapid Determination of Antibiotic Resistance in *E. coli* using Dielectrophoresis, K. Hoettges, J. Dale, M. Hughes, Physics in Medicine and Biology, vol.52, no.19, 2007.

- [16] Separation of Human Breast Cancer Cells from Blood by Differential Dielectric Affinity (Electrorotation), F. Becker, X. Wang, Y. Huang, R. Pethig, J. Vykoukal, Proceedings of the National Academy of Sciences of the United States of America, vol.92, no.3, 1995.
- [17] Leukocyte Analysis and Differentiation using High Speed Microfluidic Single Cell Impedance Cytometry, D. Holmes, D. Pettigrew, C. H. Reccius, J. D.Gwyer, C. Berkel, J. Holloway, D. E. Davies and H. Morgan, Lab on a Chip, vol.9, no.20, 2009.
- [18] Single Cell Dielectric Spectroscopy, H. Morgan, T. Sun, D. Holmes, Sh. Gawad and N. Green, Physics D-Applied Physics, vol.40, no.1, 2007.
- [19] ECIS Cultureware Disposable Electrodes Array, Applied Biophysics Inc., 2016.
- [20] Single Cell Impedance Cytometry for Identification and Counting of CD4 T-Cells in Human Blood Using Impedance Labels, D. Holmes, H. Morgan, Analytical Chemistry, vol.82, no.4, 2010.
- [21] Cell Based Biosensors Principles and Applications, P. Wang, Q. Liu, ARTECH HOUSE, MA, 2010.
- [22] MEA60-200-30-3D, Qwane Biosciences, Germany, 2014.
- [23] A Unified Approach to Dielectric Single Cell Analysis: Impedance and Dielectrophoretic Force Spectroscopy, A. Valero, T. Braschler, P. Renaud, Lab on a Chip, vol.10, no.17, 2010.
- [24] Differential Electronic Detector to Monitor Apoptosis Using Dielectrophoresis-Induced Translation of Flowing Cells (Dielectrophoresis Cytometry), M. Nikolic-Jaric, T. Cabel, E. Salimi, A. Bhide, K. Braasch, M. Butler, G. E. Bridges, and D. J. Thomson, Biomicrofluidics, vol.7, no.2, 2013.
- [25] A Compact Microwave Frequency Reflectometer with attoFarad Sensitivity: A Path Towards an Integrated Dielectrophoresis Cytometer, K. Mohammad, K. Braasch, E. Salimi, A. Bhide, B. S. Rizi, M. Butler, G. Bridges, D. Thomson, Sensors and Actuators A: Physical, vol.232, pp.132-140, 2015.
- [26] Differential Ring Oscillator Based Capacitance Sensor for Microfluidic Applications, K. Mohammad, D. J. Thomson, in Press, IEEE Transactions on Biomedical Circuits and Systems, 2016.
- [27] Integrated 0.35  $\mu\text{m}$  CMOS Capacitance Sensor with atto-Farad Sensitivity for Single Cell Analysis, K. Mohammad, D. A. Buchanan, K. Braasch, M. Butler, D. J. Thomson, IEEE Biomedical Circuits and Systems Conference, 2016.

- [28] GHz Frequency CMOS DEP Cytometer for Characterization of Single Biological Cells, K. Mohammad, D. A. Buchanan, K. Braasch, M. Butler, D. J. Thomson, Submitted to Lab on Chip Journal, 2016.
- [29] The Microflow Cytometer, J. S. Kim, F. S. Ligler, Pan Stanford Publishing, Chicago, 2010.
- [30] Electrical Forces for Microscale Cell Manipulation, J. Voldman, Annual Review of Biomedical Engineering, vol.8, pp.425-54, 2006.
- [31] Microelectronic Capacitance Transducer for Particle Detection, I. Evans, T. York, IEEE Sensors, vol.4, no.3, 2004.
- [32] Design, Fabrication and Characterization of a Femto-Farad Capacitive Sensor for Pico-Liter Liquid Monitoring, J. Wei, C. Yuea, M. Veldena, Z. L. Chenb, Z. W. Liub, K. A. Makinwaa, P. M. Sarroa, Sensors and Actuators A-Physical, vol.162, no.2, 2010.
- [33] Measurement of Small Capacitance Variations, D. Marioli, E. Sardini, A. Taroni, IEEE Transactions On Instrumentation and Measurement, vol.40, no.2, 1991.
- [34] A CMOS Capacitance Sensor That Monitors Cell Viability, S. B. Prakash, P. Abshire, IEEE Sensors, pp.1177-1180, 2005.
- [35] A Novel Low-Cost Capacitive-Sensor Interface, F. Goes, G. Meijer, IEEE Transactions On Instrumentation and Measurement, vol.45, no.2, 1996.
- [36] ZeptoFarad Capacitance Detection with a Miniaturized CMOS Current Front-End for Nanoscale Sensors, M. Carminati, G. Ferrari, F. Guagliardo, M. Sampietro, Sensors and Actuators A-physical, vol.172, no.1, 2011.
- [37] A 15 ppm Resolution Measurement System for Capacitance Transducers, C. Ghidini, D. Marioli, E. Sardini, A. Taroni, Measurement Science & Technology, vol.7, no.12, 1996.
- [38] Near-field Scanning Microwave Microscope for Interline Capacitance Characterization of Nanoelectronics Interconnect, V. Talanov, A. R. Schwartz, IEEE Transactions On Microwave Theory and Techniques, vol.57, no.5, 2009.
- [39] Electrical Detection and Actuation of Single Biological Cells with Application to Deformability Cytometry for Markerless Diagnostics, G. A. Ferrier, Ph.D Thesis, Electrical and Computer Engineering, University of Manitoba, 2011.
- [40] 40 GHz RF Biosensor Based on Microwave Coplanar Waveguide Transmission Line for Cancer Cells (HepG2) Dielectric Characterization, Y. F. Chen, H. W. Wu, Y. H. Hong, H. Y. Lee, Biosensors and Bioelectronics, vol.61, pp.417-421, 2014.

- [41] Discrimination of Colorectal Cancer Cell Lines Using Microwave Biosensors, L. Y. Zhanga, C. B. Puchb, C. Dalmaya, A. Lacroixc, A. Landoulsia, J. Leroya, C. Melinc, F. Lallouec, S. Battuc, C. Lautretteb, S. Giraudb, A. Bessaudoua, P. Blondya, M. O. Jauberteauc, A. Pothiera, *Sensors and Actuators A*, vol.216, pp.405-416, 2014.
- [42] Microwave-Based Biosensor for on-Chip Biological Cell Analysis, D. Dubuc, O. Mazouffre, C. Llorens, T. Taris, M. Poupot, J. J. Fournie, J. B. Begueret, K. Grenier, *Analog Integr. Circ. Sig. Process*, vol.77, pp.135-142, 2013.
- [43] Surface Mount Bandpass Filter, SYBP-2250 Datasheet, Mini-Circuits.
- [44] Surface Mount Directional Coupler, D18P Datasheet, Mini-Circuits.
- [45] A Microflow Cytometer with Simultaneous Dielectrophoretic Actuation for the Optical Assay and Capacitive Cytometry of Individual Fluid Suspended Bioparticles, S. F. Romanuik, M.Sc. Thesis, Electrical and Computer Engineering, University of Manitoba, 2011.
- [46] Dielectric Response of Particles in Flowing Media: The Effect of Shear-Induced Rotation on the Variation in Particle Polarizability, M. Nikolic-Jaric, G. A. Ferrier, D. J. Thomson, G. E. Bridges, M. R. Freeman, *Phys. Rev E*, vol.84, 011922, 2011.
- [47] Semi-Automated Detection of Single Cell Signatures from a Dielectrophoretic Cytometer, B. Saboktakin Rizzi, A. Bhide, T. Cabel, M. Nikolic-Jaric, E. Salimi, K. Braasch, M. Butler, G. E. Bridges, D. J. Thomson, *IEEE International Instrumentation and Measurement Technology Conference*, pp.1083-1087, 2013.
- [48] Freescale Semiconductor, Surface Mount Micromachined Silicon Accelerometer, MMA1211KEG datasheet, 2011.
- [49] An Implantable Capacitive Pressure Sensor for Biomedical Applications, C. C. Chiang, C. C. K. Lin, and M. S. Ju, *Sensors and Actuators A: Physical*, vol.134, no.2, pp.382-388, 2007.
- [50] Resistive, Capacitive, Inductive, and Magnetic Sensor Technologies, W. Y. Du, CRC Press, ch. 3, pp.99, 2014.
- [51] Single-Chip Surface Micromachined Integrated Gyroscope with 50/h Allan Deviation, J. A. Geen, S. J. Sherman, J. F. Chang, S. R. Lewis, *IEEE Journal of Solid-State Circuits*, vol.37, no.12, pp.1860-1866, 2002.
- [52] A 0.18  $\mu\text{m}$  CMOS Capacitive Sensor Lab-on-Chip, E. Ghafar-zadeh, M. Sawan, D. Therriault, *Sensors and Actuators A: Physical*, vol.141, no.2, pp.454-462, 2008.

- [53] Micro-organism-on-chip: Emerging Direct-Write CMOS-Based Platform for Biological Applications, E. Ghafar-Zadeh, M. Sawan, V. P. Chodavarapu, *IEEE Trans. Biomed. Circuits Syst.*, vol.3, no.4, pp.212-219, 2009.
- [54] Bacteria growth monitoring through a differential CMOS capacitive sensor, E. Ghafar-Zadeh, M. Sawan, V. P. Chodavarapu, T. Hosseini-Nia, *IEEE Trans. Biomed. Circuits Syst.*, vol.4, no.4, pp.232-238, 2010.
- [55] Dielectrophoresis-based integrated lab-on-chip for nano and micro-particles manipulation and capacitive detection, M. A. Miled, M. Sawan, *IEEE Trans. Biomed. Circuits Syst.*, vol.6, no.2, pp.120-132, 2012.
- [56] Reconfigurable Prototyping Microfluidic Platform for DEP Manipulation and Capacitive Sensing, A. Miled, B. Auclair, A. Srasra, M. Sawan, *IEEE Trans. Biomed. Circuits Syst.*, vol.9, no.2, pp.155-165, 2015.
- [57] A Microfluidic Capacitance Sensor for Fluid Discrimination and Characterization, M. Demori, V. Ferrari, P. Poesio, D. Strazza, *Sensors and Actuators A: Physical*, vol.172, no.1, pp.212-219, 2011.
- [58] Detection of Microdroplet Size and Speed Using Capacitive Sensors, C. Elbuken, T. Glawdel, D. Chan, C. L. Ren, *Sensors and Actuators A: Physical*, vol.171, no.2, pp.55-62, 2011.
- [59] *Impedance Spectroscopy: Applications to Electrochemical and Dielectric Phenomena*, V. F. Lvovich, John Wiley & Sons, ch.7, pp.137, 2012.
- [60] A Hybrid Microfluidic/CMOS Capacitive Sensor Dedicated to Lab-on-Chip Applications, E. Ghafar-Zadeh, M. Sawan, *IEEE Trans. Biomed. Circuits Syst.*, vol.1, no.4, pp.270-277, 2007.
- [61] A Semi-Digital Interface for Capacitive Sensors, M. A. Bakhshian, G. W. Roberts, *IEEE Int. Symp. Circuits. Syst.*, 2009.
- [62] Parylene Micro Membrane Capacitive Sensor Array for Chemical and Biological Sensing, S. Satyanarayana, D. T. McCormick, A. Majumdar, *Sensors and Actuators B: Chemical*, vol.115, no.1, pp.494-502, 2006.
- [63] Single Chip Interdigitated Electrode Capacitive Chemical Sensor Arrays, M. Kitsara, D. Goustouridis, S. Chatzandroulis, M. Chatzichristidi, I. Raptis, Th. Ganetsos, R. Igreja, C. J. Dias, *Sensors and Actuators B: Chemical*, vol.127, no.1, pp.186-192, 2007.
- [64] A Broadband Complex Permittivity Probe Using Stepped Coaxial Line, S. Seewattanapon, P. Akkaraekthalin, *Electromagn. Anal. Appl.*, 2011.

- [65] Detection of Microdroplet Size and Speed Using Capacitive Sensors, C. Elbuken, T. Glawdel, D. Chan, C. Ren, *Sensors and Actuators A: Physical*, vol.171, no.2, pp.55-62, 2011.
- [66] Surface Micromachined and Integrated Capacitive Sensors for Microfluidic Applications, J. Shih, J. Xie, Y. C. Tai, *IEEE Int. Conf. Transducers Solid State Sens. Act. Microsyst.*, vol.1, pp.388-391, 2003.
- [67] NXP Semiconductors, Low-Power Buffer and Inverter, 74AUP2G3404 datasheet, 2012.
- [68] Multiturn PTFE Dielectric Trimmer Capacitors, Sprague-Goodman, ER-530-006 datasheet, 2003.
- [69] 2 Input Exclusive-OR Gate, Fairchild Semiconductor, NC7SV86 datasheet, 2004.
- [70] A Study of Injection Locking and Pulling in Oscillators, B. Razavi, *IEEE Journal of Solid-State Circuits*, vol.39, no.9, pp.1415-1424, 2004.
- [71] Phase Noise and Fundamental Sensitivity of Oscillator-Based Reactance Sensors, H. Wang, W. Ching-Chih, A. Hajimiri, *IEEE Transactions on Microwave Theory and Techniques*, vol.61, no.5, pp.2215-2229, 2013.
- [72] A General Theory of Phase Noise in Electrical Oscillators, A. Hajimiri, T. H. Lee, *IEEE Journal of Solid-State Circuits*, vol.33, no.2, pp.179-194, 1998.
- [73] Jitter and Phase Noise in Ring Oscillators, A. Hajimiri, S. Limotyrakis, T. H. Lee, *IEEE Journal of Solid-State Circuits*, vol.34, no.6, pp.790-804, 1999.
- [74] Jitter in Ring Oscillators, A. J. McNeill, *IEEE Journal of Solid-State Circuits*, vol.32, no.6, pp.870-879, 1997.
- [75] Dielectric Constant of Water from 0 to 100 C, C. G. Malmberg, A. A. Maryott, *J. Res. Nat. Bureau Stand.*, vol.56, pp.1-8, 1956.
- [76] Dielectric Constants of Some Organic Solvent-Water Mixtures at Various Temperatures, G. Akerlof, *Journal of the American Chemical Society*, vol.54, no.11, pp.4125-4139, 1932.
- [77] CMOS Digital Integrated Circuits, S. M. Kang, Y. Leblebici, Tata McGraw-Hill Education, ch.6, pp.251-253, 2003.
- [78] Cells on Chips, J. El-Ali, P. K. Sorger, K. F. Jensen, *Nature*, vol. 442, no. 7101, pp.403-411, 2006.
- [79] Nanotechnology in Biology and Medicine: Methods, Devices, and Applications, T. Vo-Dinh, CRC Press, ch.38, 2007.

- [80] A CMOS Chip for Individual Cell Manipulation and Detection, N. Manaresi, A. Romani, G. Medoro, L. Altomare, A. Leonardi, M. Tartagni, R. Guerrier, *IEEE Journal of Solid-State Circuits*, vol.38, no.12, pp.2297-2305, 2003.
- [81] Electronic Sorting and Recovery of Single Live Cells from Microlitre Sized Samples, A. B. Fuchs, A. Romani, F. Delphine, G. Medoro, M. Abonnenc, L. Altomare, I. Chartier, D. Guergour, C. Villiers, P. N. Marche, M. Tartagni, *Lab on a Chip*, vol.6, no.1, pp.121-126, 2006.
- [82] A CMOS Impedance Cytometer for 3D Flowing Single-Cell Real-Time Analysis with  $\Delta\Sigma$  Error Correction, K. Lee, J. Nam, S. Choi, H. Lim, S. Shin, G. H. Cho, *IEEE International Solid-State Circuits Conference- Digest of Technical Papers (ISSCC)*, pp.304-306, 2012.
- [83] A CMOS Micro-Flow Cytometer for Magnetic Label Detection and Classification, P. Murali, I. Izyumin, D. Cohen, J. C. Chien, A. M. Niknejad, B. Boser, *IEEE International Solid-State Circuits Conference-Digest of Technical Papers (ISSCC)*, pp.422-423, 2014.
- [84] A 6.5/17.5-GHz Dual-Channel Interferometer-Based Capacitive Sensor in 65-nm CMOS for High-Speed Flow Cytometry, J. C. Chien, M. Anwar, E. C. Yeh, L. P. Lee, A. M. Niknejad, *IEEE MTT-S International Microwave Symposium (IMS)*, pp.1-4, 2014.
- [85] Breast Tumor Cell Detection at Single Cell Resolution Using an Electrochemical Impedance Technique, K. S. Arya, K. C. Lee, A. R. Abdur-Rahman, *Lab on a Chip*, vol.12, no.13, pp.2362-2368, 2012.
- [86] Capacitive Sensing of Droplets for Microfluidic Devices Based on Thermocapillary Actuation, J. Z. Chen, A. A. Darhuber, S. M. Troian, S. Wagner, *Lab on a Chip*, vol.4, no.5, pp.473-480, 2004.
- [87] *Introduction to microfabrication*, S. Franssila, John Wiley & Sons, 2010.
- [88] CMOS High Density Electrical Impedance Biosensor Array for Tumor Cell Detection, Y. Chen, C. C. Wong, T. S. Pui, R. Nadipalli, R. Weerasekera, J. Chandran, H. Yu, A. R. Rahman, *Sensors and Actuators B: Chemical*, vol.173, pp.903-907, 2012.
- [89] Dynamics of Oxidation of Aluminium Nanoclusters Using Variable Charge Molecular-Dynamics Simulations on Parallel Computers, T. Campbell, R. K. Kalia, A. Nakano, P. Vashishta, S. Ogata, S. S. Rodgers, *Physical Review Letters*, vol.82, no.24, p.4866, 1999.
- [90] *Biomaterials: A Basic Introduction*, Q. Chen, G. Thouas, CRC Press, 2014.
- [91] *Corrosion Prevention and Protection: Practical Solutions*, E. Ghali, V. S. Sastri, M. Elboudjaini, John Wiley & Sons, 2007, ch.7, p.468.

- [92] AC Frequency Characteristics of Coplanar Impedance Sensors as Design Parameters, J. Hong, D. S. Yoon, S. K. Kim, T. S. Kim, S. Kim, E. Y. Pak, K. No, *Lab on a Chip*, vol.5, no.3, pp.270-279, 2005.
- [93] Multi-Frequency DEP Cytometer Employing a Microwave Sensor for Dielectric Analysis of Single Cells, S. Afshar, E. Salimi, K. Braasch, M. Butler, D. J. Thomson, G. E. Bridges, *IEEE Transaction on Microwave Theory and Techniques*, vol.64, no.3, 2016.
- [94] The Dielectric Relaxation of Water Between 0 C and 35 C, R. Buchner, J. Barthel, J. Stauber, *Chemical Physics Letters*, vol.306, no.1, pp.57-63, 1999.
- [95] Oscillator-Based Reactance Sensors with Injection Locking for High-Throughput Flow Cytometry Using Microwave Dielectric Spectroscopy, J. C. Chien, A. M. Niknejad, *IEEE Journal of Solid State Circuits*, vol.51, no.2, pp.457-472, 2016.
- [96] *RF Microelectronics*, B. Razavi, New Jersey: Prentice Hall, ch.9, 1998.
- [97] Differential Tumor-Targeting Abilities of Three Single-Domain Antibody Formats, A. Bell, Z. J. Wang, M. Arbabi-Ghahroudi, T. A. Chang, Y. Durocher, U. Trojahn, J. Baardsnes, *Cancer letters*, vol.289, no.1, pp.81-90, 2010.
- [98] Time Domain Dielectric Spectroscopy Study of Human Cells: II. Normal and Malignant White Blood Cells, Y. Plevaya, I. Ermolina, M. Schlesinger, B. Z. Ginzburg, Y. Feldman, *Biochimica et Biophysica Acta (BBA)-Biomembranes*, vol.1419, no.2, pp.257-271, 1999.
- [99] *Optofluidic Devices for Cell, Microparticle, and Nanoparticle Manipulation*, A. T. Ohta, ProQuest, ch.2, pp.4, 2008.
- [100] Phase Noise and Jitter in CMOS Ring Oscillators, A. Abidi, *IEEE Journal of Solid-State Circuits*, vol.41, no.8, pp.1803-1816, 2006.
- [101] A Study of Oscillator Jitter Due to Supply and Substrate Noise, F. Herzel, B. Razavi, *IEEE Transactions on Circuits and Systems II, Analog and Digital Signal Processing*, vol.46, no.1, pp.56-62, 1999.
- [102] Jitter in Oscillators with 1/f noise Sources, C. Liu, J. A. McNeill, *Proceeding of the IEEE International Symposium on Circuits and Systems*, vol.1, pp.773-776, 2004.
- [103] Noise in phase-locked loops, A. Hajimiri, *Proceedings of the SSMSD*, vol.1, pp.1-6, 2001.
- [104] Noise Properties of PLL Systems, V. Kroupa, *IEEE Transactions on communications*, vol.30, no.10, pp.2244-2252, 1982.

- [105] TSMC Spice Model, 0.35  $\mu\text{m}$  mixed mode (2P4M, 3.3V/5V) Polycide process, BSIM3 (V3.1) model, Doc. No. T-035-MM-SP-002, Version 2.4, January 02, 2002.
- [106] TSMC 0.35  $\mu\text{m}$  Logic/Mixed-Mode Polycide (3.3V) MOS Transistor Noise Data, Doc. No. TA-1095-6302, Version 1.2, August 05, 1998.
- [107] Comparison of 1/f noise in JFETs and MOSFETs with several figures of merit, F. A. Levinzon, L. K. J. Vandamme, *Fluctuation and Noise Letters*, vol.10, no.04, pp.447-465, 2011.
- [108] An On-Chip, Interconnect Capacitance Characterization Method with Sub-Femto-Farad Resolution, J. Chen, D. Sylvester, H. Chenming, *IEEE Transactions on Semiconductor Manufacturing*, vol.11, no.2, 1998.
- [109] A Fully Differential Rail-to-Rail CMOS Capacitance Sensor with Floating-Gate Trimming for Mismatch Compensation, S. B. Prakash, P. Abshire, *IEEE Transactions On Circuits And Systems*, vol.56, no.5, 2009.
- [110] A Silicon MEMS Structure for Characterization of Femto-Farad-Level Capacitive Sensors with Lock-in Architecture, J. Wei, C. Yue, Z. L. Chen, Z. W. Liu, P. M. Sarro, *Micromechanics and Microengineering*, vol.20, no.6, 2010.
- [111] Novel Direct-Write CMOS-Based Laboratory-on-Chip: Design, Assembly and Experimental Results, E. Ghafar-Zadeh, M. Sawan, D. Therriault, *Sensors and Actuators A: Physical*, vol.134, no.1, pp.27-36, 2007.
- [112] Capacitance Cytometry: Measuring Biological Cells One by One, L. L. Sohn, O. A. Saleh, G. R. Facer, A. J. Beavis, R. S. Allan, D. A. Notterman, *Proceedings of the National Academy of Sciences of the United States of America*, vol.97, no.20, 2000.
- [113] A High-Performance MEMS Capacitive Strain Sensing System, M. Suster, J. Guo, N. Chaimanonart, W. H. Ko, D. J. Young, *Microelectromechanical Systems*, vol.15, no.5, 2006.
- [114] *Design of Analog CMOS Integrated Circuits*, B. Razavi, McGraw-Hill, Boston, 2001.
- [115] Monitoring Dielectric Properties of Single MRC5 Cells and Oligomycin Treated Chinese Hamster Ovary Cells Using a Dielectrophoretic Cytometer, B. S. Rizi, M.Sc. diss., University of Manitoba, 2014.
- [116] Cell Confluency Analysis on Microcarriers by Micro-Flow Imaging, C. J. Farrell, S. M. Cicalese, H. B. Davis, B. Dogdas, T. Shah, T. Culp, V. M. Hoang, *Cytotechnology*, pp.1-10, 2016.